COMPUTATIONAL INVERSE SOLUTION STRATEGIES FOR CHARACTERIZATION OF LOCALIZED VARIATIONS OF MATERIAL PROPERTIES IN SOLIDS AND STRUCTURES

by

Mengyu Wang

B.S. in Geological Engineering, Tongji University, China, 2006

M.S. in Geological Engineering, Tongji University, China, 2010

Submitted to the Graduate Faculty of

the Swanson School of Engineering in partial fulfillment

of the requirements for the degree of

Doctor of Philosophy

University of Pittsburgh

2014

UNIVERSITY OF PITTSBURGH

SWANSON SCHOOL OF ENGINEERING

This dissertation was presented

by

Mengyu Wang

It was defended on

July 22nd, 2014

and approved by

John C. Brigham, Ph.D., Assistant Professor, Department of Civil and Environmental Engineering and Bioengineering

Jeen-Shang Lin, Sc.D., Associate Professor, Department of Civil and Environmental Engineering

Julie M. Vandenbossche, Ph.D., Associate Professor, Department of Civil and Environmental Engineering

Hae Young Noh, Ph.D., Assistant Professor, Department of Civil and Environmental Engineering, Carnegie Mellon University

Dissertation Director: John C. Brigham, Ph.D., Assistant Professor, Department of Civil and Environmental Engineering and Bioengineering

COMPUTATIONAL INVERSE SOLUTION STRATEGIES FOR CHARACTERIZATION OF LOCALIZED VARIATIONS OF MATERIAL PROPERTIES IN SOLIDS AND STRUCTURES

Mengyu Wang, PhD

University of Pittsburgh, 2014

Computational inverse characterization approaches that combine computational physical modeling and nonlinear optimization minimizing the difference between measurements from experimental testing and the responses from the computational model are uniquely well-suited for quantitative characterization of structures and systems for a variety of engineering applications. Potential applications that are suited for computational inverse characterization range from damage identification of civil structures to elastography of biological tissue. However, certain challenges, primarily relating to accuracy, efficiency, and stability, come along with any computational inverse characterization approach. As such, proper application-specific formulation of the inverse problem, including parameterization of the field to be inversely determined and selection/implementation of the optimization approach are critical to ensuring an accurate solution can be estimated with minimal (i.e. practically applicable) computational expense.

The present work investigates strategies to optimally utilize the available measurement data in combination with a *priori* information about the nature of the unknown properties to maximize the efficiency and accuracy of the solution procedure for applications in inverse characterization of localized material property variations. First, a strategy using multi-objective optimization for inverse characterization of material loss (i.e., cracks or erosion) in structural components is presented. For this first component, the assumption is made that sufficient a *priori* information is available to restrict the parameterization of the unknown

field to a known number and shape of material loss regions (i.e., the inverse problem is only required to identify size and location of these regions). Since this type of parameterization would typically be relatively compact (i.e., low number of parameters), the inverse problem is well suited for non-gradient-based optimization approaches, which can provide accuracy through global search capabilities. The multi-objective inverse solution approach shown divides the available measurement data into multiple competing objectives for the optimization process (rather than the typical single objective for all measurement data) and uses a stochastic multi-objective optimization technique to identify a Pareto front of potential solutions, and then select one "best" inverse solution estimate. Through simulated test problems of damage characterization, the multi-objective optimization approach is shown to provide increased solution estimate diversity during the search process, which results in a substantial improvement in the capabilities to traverse the optimization search space to minimize the measurement error and produce accurate damage size and location estimates in comparison with analogous single objective optimization approaches. An extension of this multi-objective approach is then presented that addresses problems for which the quantity of localized changes in properties is unknown. Thus, a self-evolving parameterization algorithm is presented that utilizes the substantial diversity in the Pareto front of potential solutions provided by the multi-objective optimization approach to build up the parameterization iteratively with an *ad hoc* clustering algorithm, and thereby determine the quantity, size, and location of localized changes in properties with minimal computational expense. Similarly as before, through simulated test problems based on characterization of damage within plates, the solution strategy with self-evolving parameterization is shown to provide an accurate and efficient process for the solution of inverse characterization of localized property changes.

For the second half of the present work, a substantial change in the inverse problem assumptions is made, in that the nature (i.e., shape) of the property variation is no longer assumed to be known as precisely a *priori*. Thus, a more general (e.g., mesh-based) parameterization of the unknown field is needed, which would typically come at a cost of significantly increased computational expense and/or loss of solution uniqueness. To balance the generalization of the approach and still utilize some amount of the knowledge that the solution is localized in nature, while maintaining efficiency, a hybrid compact-generalized

parameterization approach is presented. The initial incarnation of this hybrid approach combines a machine learning data reconstruction strategy known as gappy proper orthogonal decomposition (POD) with a least-squares direct inversion approach to estimate material stiffness distribution in solids (i.e., to solve elastography problems). The direct inversion approach uses a generalized mesh-based parameterization of the unknown field, but full-field response measurements (i.e., measurements everywhere in the solid) are required, which are not available for most practical inverse characterization problems. Therefore, the gappy POD technique first identifies the pattern of potential response fields of the solid through a collection of a *priori* forward numerical analyses of the solid response with a specified compact parameterization and a corresponding collection of arbitrarily generated parameter sets. Once the pattern is identified, the gappy POD technique is able to use the available partial-field measurement data to estimate the full-field response of the solid to be used by the direct inversion. Thus, the computational cost of the inverse characterization is negligible once the gappy POD process has been completed. Through simulated test problems relating to characterization of inclusions in solids, the direct inversion approach with gappy POD is shown to provide highly efficient and relatively accurate inverse characterization results for the prediction of Young's modulus distributions from partial-field measurement data. This direct inversion approach is further validated through an example problem regarding characterization of the layered stiffness properties of an engineered vessel from ultrasound measurements. Lastly, an extension of this hybrid approach is presented that uses the characterization results provided by the previous direct inversion approach as the initial estimate for a gradient-based optimization process to further refine/improve the inverse solution estimate. In addition, the adjoint method is used to calculate the gradient for the optimization process with minimal computational expense to maintain the overall computational efficiency of the inverse solution process. Again, through simulated test problems based on the characterization of localized, but arbitrarily shaped, inclusions within solids, the three-step (gappy POD - direct inversion - gradient-based optimization) inverse characterization approach is shown to efficiently provide accurate and relatively unique inverse characterization estimates for various types of inclusions regardless of inclusion geometry and quantity.

TABLE OF CONTENTS

LIST OF TABLES

LIST OF FIGURES

PREFACE

I would like to first express my deepest gratitude to my advisor and chair of my graduate committee Professor John C. Brigham who taught me learn to be an independent and self-motivated researcher and thinker with his unending inspiration and help.

My appreciation to Professor Jeen-Shang Lin who not only gave me the precious opportunity to start my Ph.D. education at the University of Pittsburgh, but also served on my graduate committee with his support.

My thanks to Professor Julie M. Vandenbossche and Professor Hae Young Noh for serving on my graduate committee with their help.

Special thanks go to thank my colleagues in Professor John C. Brighm's group for their help and encouragement during my PhD study.

Last, but certainly not least, my deepest gratitude goes to my family includes father named Shoulun Wang, mother named Guozhen Xing, younger brother named Jingyu Wang and my future wife (I assume) named Pingping Zhao, for their unconditional love and support. It is my inexhaustible fortune to have every one of you in my life.

1.0 ASSESSMENT OF MULTI-OBJECTIVE OPTIMIZATION FOR NONDESTRUCTIVE EVALUATION OF DAMAGE IN STRUCTURAL COMPONENTS

1.1 ABSTRACT

A multi-objective optimization-based computational approach to nondestructive evaluation of damage in structural components, and more generally in solid continua, is discussed and numerically evaluated. The multi-objective approach provides a substantial improvement in the capabilities to traverse the optimization search space to minimize the measurement error and produce accurate damage estimates. Through simulated test problems based on the characterization of damage in structural steel components, including internal pipe surface geometry as well as material loss within a plate structure utilizing steady-state dynamic measurements of outer surface displacement, a multi-objective genetic algorithm optimization approach is shown to provide substantial computational improvement over single-objective strategies. The multi-objective approach consistently and efficiently produces more accurate characterization results in contrast to equivalent single-objective strategies. More importantly, the multi-objective approach is shown to exhibit consistently better tolerance to test measurement noise and measurement sparsity. Moreover, the multi-objective strategy was found to provide improved diversity in the solution estimates for ill-posed problems, which is an important step leading to insight into the necessary changes to the testing or parameterization to subsequently produce more accurate and unique solutions to such inverse characterization problems.

1.2 INTRODUCTION

Approaches that combine computational mechanics with nonlinear optimization strategies to solve inverse problems in nondestructive evaluation provide generalized frameworks for treating and distinguishing between various contributions to a system response, while providing physically meaningful solutions that can be applied to predict future behaviors [8, 10, 62, 9]. However, there are several key challenges in implementing these approaches, one of which in particular is the need for consistent and efficient nonlinear optimization to identify the unknown system parameters that optimally reproduce the experimental measurements. Complicating things further is that the optimization search spaces for nondestructive evaluation (NDE) problems are often large (e.g., broad ranges of values for damage location and magnitude) as well as highly nonconvex, resulting in a propensity for many optimization approaches to become stuck in local minima (i.e., identify incorrect solutions).

Nongradient-based algorithms such as genetic algorithms have seen substantial use to date to overcome the nonconvexity issues [36, 30, 28]. Yet, while stochastic search algorithms are well equipped for global search capabilities they often require a relatively large number of function evaluations (e.g., finite element analyses to determine a potential solution's accuracy), which can become computationally prohibitive with any degree of complexity of the system under consideration. Alternatively, for structural engineering applications (e.g., damage detection in beam or truss structures) a simple modification of utilizing multi-objective (rather than the typical single-objective) optimization has shown promise to significantly improve the consistency and efficiency of computational NDE strategies [32, 55, 54, 53, 56, 52, 58, 12, 27, 29].

[27, 12] presented some of the earliest work on incorporating multi-objective optimization for structural damage detection in which algorithms were discussed to determine a measure of stiffness for each element of a discretized frame by minimizing the deviation from measured natural frequencies and mode shapes independently in a multi-objective sense. Subsequently, Perera and coworkers have done a considerable amount of work relating to the application of multi-objective optimization strategies to improve NDE solution techniques for structural applications. Specifically, in [55, 52, 54, 53] two objectives based on the mode shapes and

natural frequencies of the structures are minimized independently through non-gradient-based strategies (e.g., genetic algorithm or particle swarm optimization) to estimate damage locations and magnitudes within beam or truss elements. In addition, [32] explored the potential improvements to noise tolerance and sparse measurement data that can be obtained with multi-objective optimization for determining the location and magnitude of damaged elements in truss structures from two sets of vertical displacement measurements. In general, thus far analyses have shown that in structural mechanics applications by dividing the physical targets for the inverse problem into multiple objective functions and minimizing these functions simultaneously but separately, the search process is able to proceed more effectively toward an accurate estimate of the damage properties than if the objectives had been combined to form a single (weighted) objective.

The present work extends this concept of multi-objective optimization for NDE-type inverse problems from structural analysis (i.e., beam and truss modeling) to more generalized problems through the example of solid continua. Moreover, this work uses simulated examples to provide a unique examination of the benefits of a multi-objective optimization strategy with respect to both accuracy and efficiency for NDE applications, the relative effects to accuracy caused by measurement noise and sparse measurement data, as well as the ability to improve solution set diversity specifically for non-unique problems. In the following section the general inverse problem solution framework is outlined, including a detailed explanation of the multi-objective genetic algorithm optimization procedure employed. Then, simulated NDE examples of characterizing erosion in the wall of a pipe structure and identifying holes in a plate structure are presented, including analysis of the inverse characterization results, which is followed by the concluding remarks.

1.3 COMPUTATIONAL INVERSE MECHANICS

Generally, computational inverse mechanics approaches for NDE (depending on implementation and application also referred to as model updating or by other monikers) consist of first constructing a numerical representation (e.g., finite element model) (Fig. 1.1(b)) of the

behavior of the target structure that is parameterized with respect to the unknown structural/system properties ($\vec{\alpha}$) and subject to whatever particular nondestructive test has been chosen to be applied (Fig. 1.1(a)). Then, an objective function ($\gamma(\vec{\alpha})$) is constructed quantifying the difference between the experimentally measured response of the structure from the nondestructive test ($\vec{R}^{exp}$) and the response that is predicted by the numerical representation given an estimate to the structural properties ($\vec{R}^{sim}(\vec{\alpha})$). A nonlinear optimization strategy is applied to minimize the objective function (Fig. 1.1(c)), and if the objective can be minimized sufficiently the resulting structural/system parameters are deemed to be the approximation to the "true" state of the structure/system.

The success of these computational inverse mechanics approaches is dependent upon the accuracy of the numerical representation of the structure, the quality of the response measurements (i.e., noise), the sensitivity of the particular response measured to variations in the structural properties to be determined, and the capabilities of the chosen optimization algorithm to traverse the search space. Moreover, the majority of applications will see some degree of weakness in these requirements, leading to a certain amount of ill-posedness in the inverse problem that challenges the ability to successfully find a unique and accurate solution. The focus of the present work is to quantitatively examine the ability of multi-objective optimization to overcome some of the ill-posedness in NDE problems and improve solution capabilities in a general sense through examples of damage detection in solid continua.

1.4 MULTI-OBJECTIVE OPTIMIZATION

Although there are several suitable multi-objective optimization techniques, for context, the present work will solely consider the example of a multi-objective genetic algorithm (GA). For NDE applications, the key benefit of the multi-objective approach is that it maintains a high level of diversity in the solution population, which helps to prevent stalling or convergence to local minima. Diversity is maintained during the search process in contrast to the single-objective strategies by evolving a set of optimal points in the solution space with respect to the multiple objective functions known as the Pareto set. The Pareto set can be defined

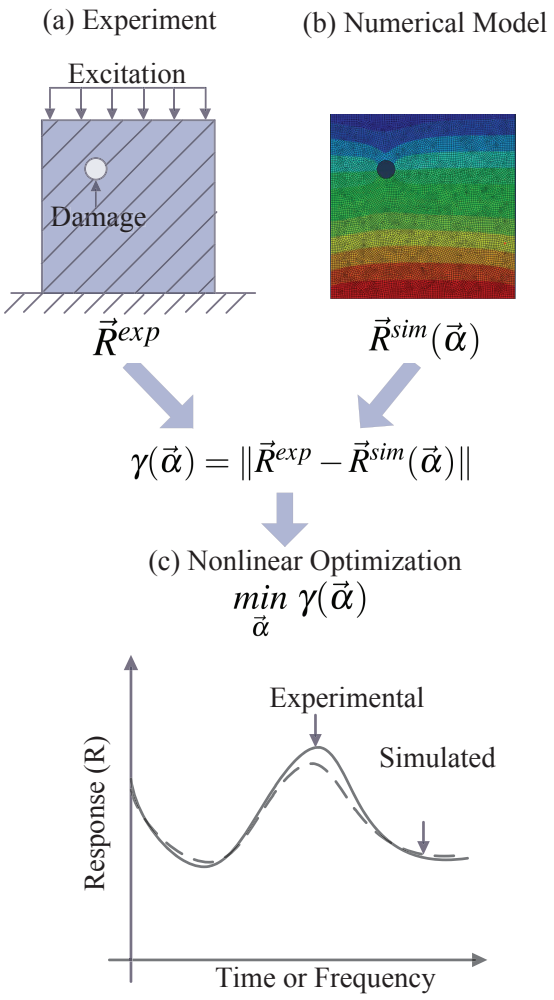

Figure 1.1: Example schematic of the computational inverse mechanics approach for NDE.

as the set of solutions that are not dominated by any other solution in the search space. For example, as shown in Fig. 1.2 for a two-objective optimization, potential solutions A and B both dominate C in that they have lower values of both objective functions, but are not dominated themselves by any other potential solution shown (they may have a higher value of one objective, but never both), and therefore A and B belong to the Pareto set and C does not. Another term for the Pareto set is the "First front", and the remaining solution estimates that are not in the Pareto set can be divided into several subsequent fronts (Second, Third, and so on) based on the criteria that each member of a front is not dominated by any member of the same or higher-number fronts, as shown in Fig. 1.2.

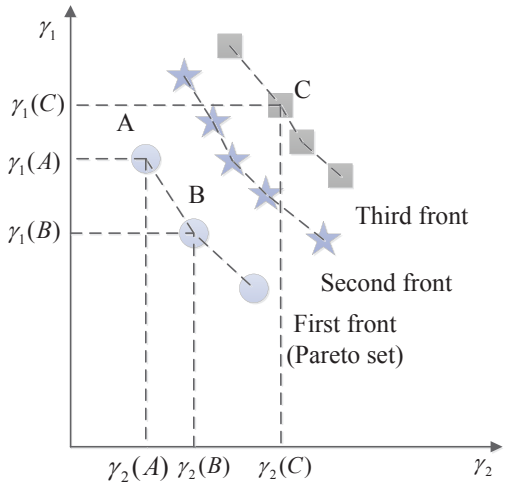

Figure 1.2: Potential solution set distribution for a two-objective (γ_1 and γ_2) optimization problem and their divisions into three non-dominating fronts.

Within a GA the multi-objective criteria primarily affects the ranking of the individuals in the population, which then governs how the evolution operators of mutation, crossover, and natural selection are applied. Specifically, a controlled elitist multi-objective GA (CEMGA) was used for the examples considered herein. While there are alternate multi-objective algorithms available that would likely provide similar results, the CEMGA was used for the present work due to its documented robustness with respect to global search capability and availability within the commercial software MATLAB ([41]). The overall procedure of

CEMGA to evolve a set (i.e., population) of solution estimates towards obtaining the Pareto set is as follows:

1. Randomly generate an initial population of trial solution sets (i.e., individuals) for the unknown parameters and evaluate each parameter set to obtain the corresponding value for each objective function.
2. Assign a priority score to each individual in the population based on their corresponding front (see Fig. 1.2) and measure of "crowdedness" (i.e., how near the individual is to others on the same front in the objective function space).
3. Select a subset of "parent" individuals from the population based on the priority score.
4. Generate new individuals by applying crossover and mutation to the parent individuals and evaluate their respective priority scores.
5. Create the next generation of individuals by selecting from the current population and offspring based on the priority scores and Pareto fraction (i.e., limitation on the number selected from the current Pareto set).
6. IF the stopping criteria is met - OUTPUT the Pareto set of parameter solutions and STOP;

   ELSE RETURN to 3.

A higher priority score, and therefore higher chance to survive throughout generations is assigned to individuals with lower front number and larger distance measure in the objective function space with respect others in the same front. Typical stopping criteria include a maximum number of generations and/or analysis time and limits placed on the change in spread of the individuals in the Pareto set. Note that while the multi-objective approach evolves a set of optimal solutions rather than just one, the physical reality of an NDE problem is that there can be only one "true" solution. Therefore, a postprocessing method is typically applied at the completion of the optimization process to produce one optimal solution estimate from the Pareto set. See [15, 41, 32, 52] for additional details about the CEMGA, including specifics of the operators, stopping criteria, and postprocessing methods that can be used therein.

1.5 EXAMPLES AND DISCUSSION

Several simulated examples of damage characterization (i.e., numerically simulated experiments with chosen damage parameters) were considered to examine the potential benefits of using the multi-objective optimization approach for NDE problems in solid continua. In all cases the simulated nondestructive tests consisted of applying a harmonic pressure to a small portion of the structure at an excitation frequency of 20 Hz, and then measuring the resulting steady-state harmonic displacement amplitudes at several discrete locations along the outer surface of the structure. Vibration testing using direct frequency response measurements was chosen based on its documented ability to provide substantial diagnostic information for a global evaluation of a structure [11, 39]. However, the overall approach and benefits would be expected to yield similar results for alternate testing approaches.

For both generating the experimental data and simulating the forward problem during the inverse solution process the structures were assumed to behave linearly and be defined by steady-state dynamic solid mechanics and analyzed using the finite element method. For the simulated experiments the damage was modeled by directly modifying the geometry (e.g., creating holes), and therefore modifying the finite element mesh. By contrast, for the simulations of the structures throughout the inverse solution process (i.e., for evaluation of the individual fitness during optimization) the meshes remained constant describing the geometry of a healthy structure (i.e., structure without damage), and the damage was modeled by reducing both the Young's modulus and density to negligibly small values at all integration points within the specified damage region. This modeling procedure for the inverse simulations allowed the model to be efficiently parameterized for the optimization process, while also helping to alleviate the inverse crime inherent to simulated experiments by utilizing a moderately different model to generate the experiment as that used for the inverse solution process.

The inverse problems to determine the structural parameters defining the damage in the example structures were briefly cast in the form of the following multi-objective optimization problem. The multi-objective functions that define the difference between the experimental measurements and the responses of the numerical model of the example structures are in

terms two arbitrary groupings of the displacements measured on the surface of the structures due to the harmonic excitation:

$$\underset{\vec{\alpha}}{min} \begin{cases} \gamma_1(\vec{\alpha}) = \left(\frac{\sum_{j=1}^{n} \left(U_{aj}^{exp} - U_{aj}^{sim}(\vec{\alpha}) \right)^2}{\sum_{j=1}^{n} \left(U_{aj}^{exp} \right)^2} \right)^{1/2} \\ \gamma_2(\vec{\alpha}) = \left(\frac{\sum_{j=1}^{m} \left(U_{bj}^{exp} - U_{bj}^{sim}(\vec{\alpha}) \right)^2}{\sum_{j=1}^{m} \left(U_{bj}^{exp} \right)^2} \right)^{1/2} \end{cases}, \tag{1.1}$$

where $\vec{\alpha}$ is the vector containing the parameters of the unknown damage to be determined in the inverse problem, U_{aj}^{exp} and U_{aj}^{sim} are the experimentally measured and numerically simulated displacement at the j^{th} measurement location in the first grouping, respectively, and U_{bj}^{exp} and U_{bj}^{sim} are the experimentally measured and numerically simulated displacement at the j^{th} measurement location in the second grouping, respectively.

While the displacement groupings were chosen arbitrarily for the two separate objectives for the examples in the present study, it would certainly be possible to investigate additional or alternate competing objectives, such as measurements of different directional components and/or from multiple regions of the domain, which may provide different benefits and shortcomings depending on the nature of a particular application.

The CEMGA multi-objective optimization algorithm discussed was applied to solve the constrained optimization problem in terms of the two objective functions, γ_1 and γ_2, as outlined above. In addition, to obtain a single solution estimate from the Pareto set of solutions provided by the CEMGA, at completion the Pareto set was postprocessed to select the one individual with the minimum l_2-norm of the two objective functions as follows:

$$\underset{\vec{\alpha} \in P}{min} \left(\gamma_1^2(\vec{\alpha}) + \gamma_2^2(\vec{\alpha}) \right), \tag{1.2}$$

where P represents the Pareto set obtained by the CEMGA. As discussed previously, there have been alternate methods used to select the final estimate from such results. However, since the measurement groupings used for the examples herein are physically similar quantities to each other, the above choice is somehow intuitively ideal, providing the optimal solution estimate in an average sense.

For comparison purposes, two additional optimization approaches were applied to solve the inverse damage characterization problems in each example, in both cases utilizing a standard single-objective GA technique (see ([28])) for an overview of a typical single-objective genetic algorithm procedure).

In the first set of alternate tests, referred to as the "Lumped-Objectives" trials, the standard GA was applied to minimize the l_2-norm of the two objective functions (similar to the postprocessing equation for the Multi-Objective trials). For the second set of alternate tests, referred to as the "Single-Objective" trials, only one of the objective functions was minimized by the GA, either γ_1 or γ_2. As such, twice the number of analyses were performed for the Single-Objective trials as for the Lumped-Objective or Multi-Objective cases, since one set of tests were performed only using γ_1 and another set only using γ_2.

An initial population of 40 individuals was utilized for all GA cases (Lumped-, Single-, and Multi-Objective), as well as scattered crossover and adaptive feasible mutation. The CEMGA used tournament selection, while the single-objective GA used stochastic uniform sampling. In all cases to ensure a fair comparison the stopping criteria for the optimization was set as a maximum number of generations (which is equivalent to setting a maximum number of finite element analyses). In addition, due to the stochastic nature of the optimization solution strategies, the inverse problem solution procedure was repeated five times for all test cases for all optimization methods and the mean and standard deviation of the results were analyzed to quantify both the accuracy and the consistency of the various techniques for each example.

1.5.1 Example 1: Simulated Pipe With Erosion

The first example consisted of evaluation of a simulated steel pipe to determine the unknown amount of erosion from the inner wall of the pipe. As shown with the pipe cross-section in Fig. 1.3, the pipe was taken to be 1 m long, with an outer radius of 42 cm, a wall thickness of 7.2 cm, and both ends were connected to fixed supports. The material behavior was defined as linear elastic with a Young's modulus of 200 GPa, Poisson's ratio of 0.3, and density of 8000 kg/m^3, and all properties were assumed to remain as defined following damage (i.e.,

the erosion damage being characterized in this simulated problem was assumed to occur without any observable change to the properties of the remaining material in the structure, and therefore only changed the structure's geometry).

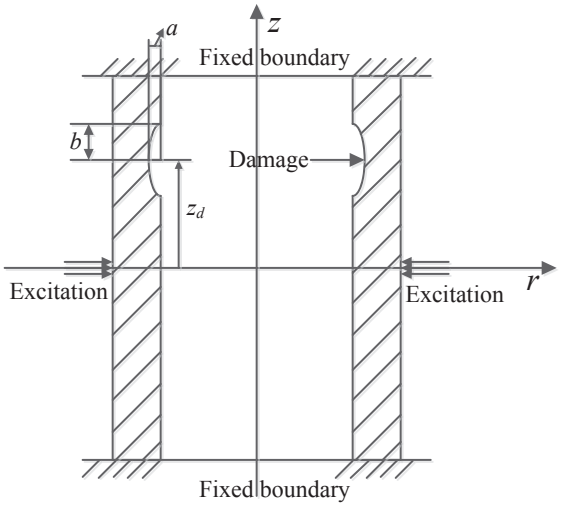

Figure 1.3: Cross-sectional schematic of the damaged pipe structure for Example 1.

To generate experimental data an ellipsoidal region representing the erosion was removed from the inner surface of the pipe in a constant manner throughout the entire circumference of the inner wall. The eroded region was therefore defined by the axial coordinate to the ellipse center, z_d, the axial radius of the ellipse, b, and the radial radius of the ellipse, a. An ellipsoidal geometry was chosen for the erosion because of its simplicity as well as the fact that similar simplifications have been applied in several works to simulate pipe structural behavior following corrosion damage ([31, 79, 6, 42]). The simulated nondestructive test consisted of applying a 1 kPa harmonic load to a 2 cm region on the surface of the pipe centered in the axial direction of the pipe and constant over the circumference of the outer wall, and both the resulting axial and radial displacements were measured at 99 locations along an axial line on the outer surface of the pipe that were equally-spaced in 1 cm increments. Note, the erosion, boundary conditions, and nondestructive testing definitions were all chosen to satisfy the axisymmetric condition, and therefore reduce the computational cost to examine the problem. Table. 1.1 shows the target values for the unknown erosion parameters (i.e., values used to generate the experimental data) and the minimum and maximum values

Table 1.1: Target (experimental) values for the unknown erosion centroid axial coordinate (z_d), radial radius (a), and axial radius (b), and the minimum and maximum values considered for the optimization search process for the example damaged pipe structure.

Erosion Parameter	Target Value	Optimization Minimum	Optimization Maximum
z_d	0.25	-0.5	0.5
a	0.03	0.0	0.072
b	0.05	0.0	0.5

considered plausible for each parameter for the inverse solution process (i.e., optimization constraints). For this first example, the axial displacement measurements were used to form the first objective (γ_1) and the radial displacement measurements were used to form the second objective (γ_2).

1.5.1.1 Optimization Efficiency To demonstrate the computational efficiency of the various GA optimization approaches the first set of tests restricted the maximum number of finite element analyses to three separate values: 400, 800, and 1200. Then, the ability of each approach to successfully minimize the objective functions within the function evaluation constraints was analyzed and compared. Note that for the Single-Objective tests, in which only one of the objective functions was provided for the optimization calculations, the results are only shown for the corresponding objective function (i.e., when axial displacement was provided as the GA objective only the error in the axial displacement measurements was plotted for that optimization solution, and similarly for the radial displacement).

Fig. 1.4 shows the mean and standard deviation of the measurement error for the axial displacement (γ_1) and radial displacement (γ_2) produced by the solutions obtained from the five trials of each optimization approach for each limit on total analyses. Overall, the Multi-Objective approach showed an improved computational efficiency in comparison to both

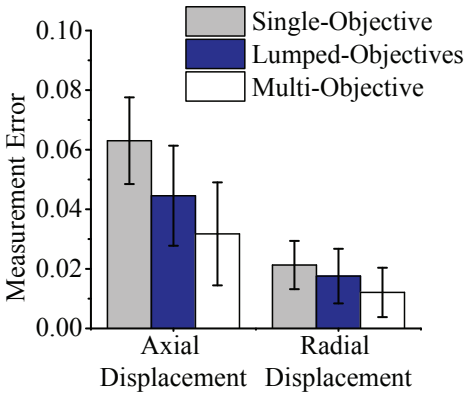

(a) 400 FEA

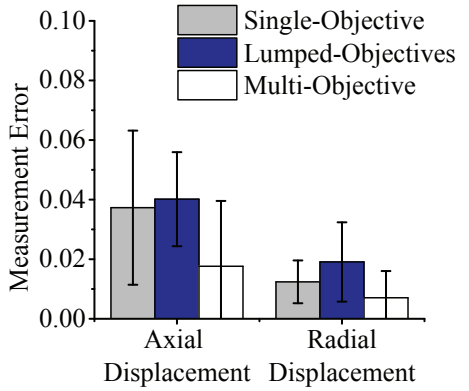

(b) 800 FEA

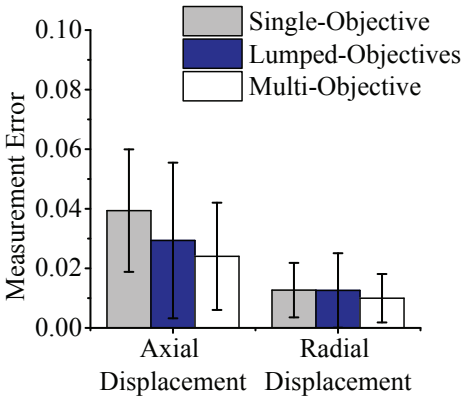

(c) 1200 FEA

Figure 1.4: Mean and standard deviation (error bars) of the measurement error for each optimization approach after the specified maximum number of finite element analyses (FEA) for Example 1.

single-objective strategies (separate or lumped), on average obtaining solution estimates with both lower axial and radial displacement measurement error regardless of the limit on the total number of finite element analyses. Moreover, after the lowest number of function evaluations (400) the Lumped-Objective approach clearly minimized the measurement error farther than the separate Single-Objective trials, but as the number of function evaluations increased the difference between the Lumped-Objective and Single-Objective approaches became almost negligible. These results particularly serve to further emphasize the challenge in traversing the optimization search space for even such a simple inverse characterization problem, and shows that adding more information in a lumped single-objective manner may not actually improve the capability to solve the inverse problem as would be expected. Yet, the Multi-Objective approach may be able to improve the capability to overcome this inverse problem challenge by better utilizing additional measurement information to more efficiently seek out a global minimum to the optimization problem.

1.5.1.2 Solution Accuracy The second set of tests was intended to examine the consistency and accuracy of the solution methods by increasing the stopping criteria to 6000 total finite element analyses, an amount sufficient to ensure all optimization trials reached convergence (whether to a local or global minimum). Fig. 1.5 again shows the mean and standard deviation of the measurement error for the axial displacement and the radial displacement produced by the solutions obtained from the five trials of each optimization approach with 6000 finite element analyses. What is most interesting is that the results for the two single-objective strategies (separate and lumped) are minimally different from those obtained in the prior tests with 1200 finite element analyses, with both the mean and standard deviation of the measurement errors remaining relatively high. By contrast the Multi-Objective results noticeably improved when the number of analyses was increased to 6000, with both a lower mean error and substantially lower standard deviation of the error results. These results imply that in most cases the single-objective strategies experienced premature convergence to local minima, while the Multi-Objective strategy was able to consistently overcome the nonconvexity of the search space given a sufficient number of analyses in nearly all trials to accurately match the measurement data.

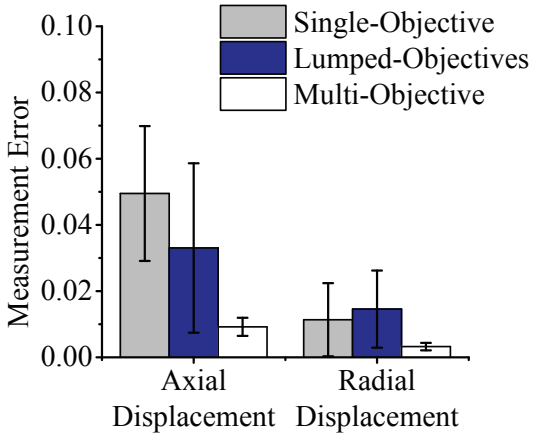

Figure 1.5: Mean and standard deviation (error bars) of the measurement error for each optimization approach after 6000 finite element analyses for Example 1.

To display the effect of the difference in measurement error on the accuracy of the inverse problem solution (i.e., erosion parameters) Fig. 1.6 shows the mean and standard deviation of the erosion parameter values obtained from the five trials of each optimization approach with 6000 finite element analyses in comparison to the target (experimental) values. Even though the modeling approach to generate the experimental data and that for the inverse solution simulations was slightly different (discussed above), the accuracy of the inverse solution estimate to the erosion parameters correlated well with the minimization of the measurement error. As such, the improved ability of the Multi-Objective approach to minimize the measurement error led to improved accuracy in the estimates to the erosion parameters in comparison to both the Single-Objective and Lumped-Objective approaches.

1.5.1.3 Measurement Noise The third set of tests was intended to examine the effect of measurement noise on the solution capabilities for damage inverse characterization of the structures. As it is guaranteed in practice to have some degree of measurement noise, which is likely correlated to the cost of the sensing systems used, it is critically important that the inverse procedure for damage characterization is not strongly affected by this measurement noise. Weak noise tolerance of the inverse procedure could lead to more ill-posed solutions.

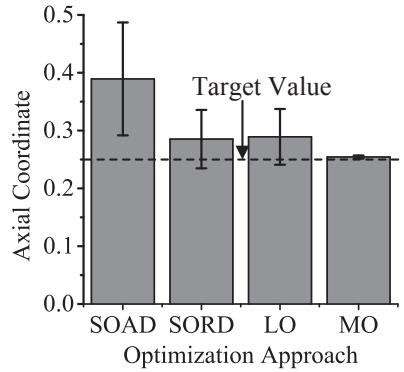

(a) Axial Coordinate

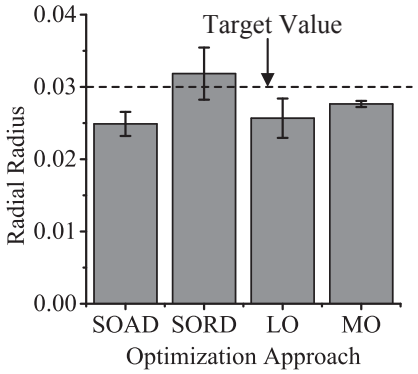

(b) Radial Radius

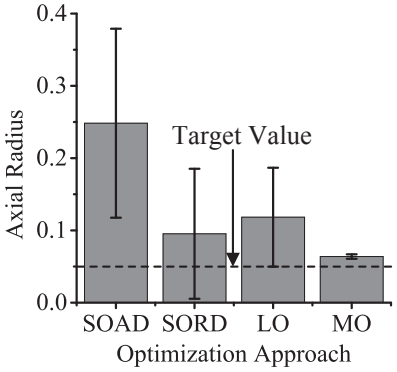

(c) Axial Radius

Figure 1.6: Mean and standard deviation (error bars) of the optimal erosion parameter solutions from each optimization approach: Single-Objective (SO) using either axial displacement (AD) or radial displacement (RD), Lumped-Objectives (LO), and Multi-Objective (MO) after 6000 finite element analyses compared to the target (experimental) values for Example 1.

Therefore, varying levels of Gaussian white noise was added to the simulated experimental measurements of the structures as follows:

$$U^{expn} = U^{exp}\left(1 + k\upsilon\right), \tag{1.3}$$

where U^{expn} is the experimental displacement measurement (either axial or radial displacement) with noise that replaced the previously used measurement without noise, U^{exp}, k is the noise amplitude multiplier, and υ is a normally distributed random variable with unit variance and zero mean. k was chosen to produce and test three different signal to noise ratios (SNR) (ordered from least noise to most): 40 dB, 30 dB, and 20 dB, based on the following definition:

$$SNR(dB) = 10log_{10}\left(\frac{1}{k}\right)^2, \tag{1.4}$$

After the addition of noise the three optimization approaches were again applied for five independent trials each with the stopping criteria set to 6000 finite element analyses and the results were analyzed.

Fig. 1.7 shows the mean and standard deviation of the measurement error for the axial displacement and radial displacement and Fig. 1.8 shows the mean and standard deviation of the erosion parameter values produced through the five trials of each optimization approach with each of the three noise levels. Analogously to the previous noise-free results, the Multi-Objective optimization approach clearly outperformed both the Single-Objective and the Lumped-Objective trials to minimize the measurement error and produce accurate estimates to the erosion parameters. Furthermore, while the final measurement error increases in all cases with increasing noise, the erosion parameter results of the Multi-Objective trials stay highly accurate, particularly in comparison to the other optimization techniques. These results thoroughly emphasize the importance of having the optimization algorithm minimize the measurement error as much as possible within the noise limitations to yield an accurate estimate of the damage parameters, something which the Multi-Objective approach was superior in accomplishing.

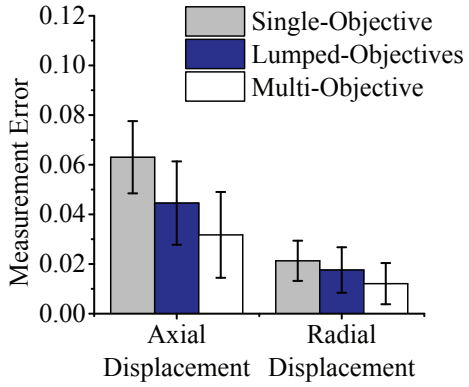

(a) 40 dB

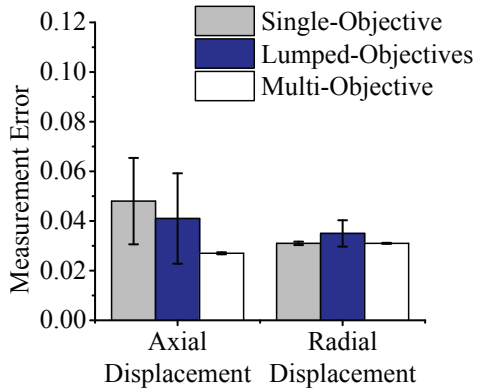

(b) 30 dB

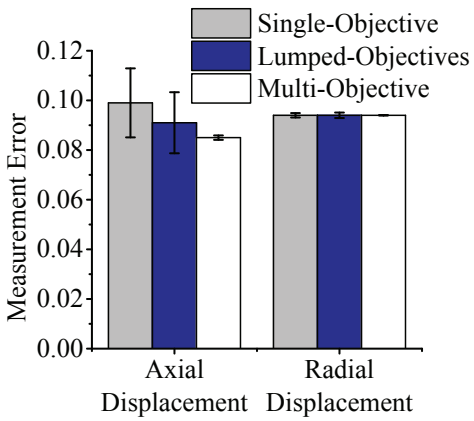

(c) 20 dB

Figure 1.7: Mean and standard deviation (error bars) of the measurement error for each optimization approach subject to the specified level of measurement noise after 6000 finite element analyses for Example 1.

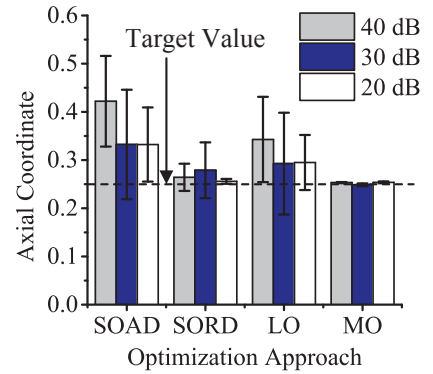

(a) Axial Coordinate

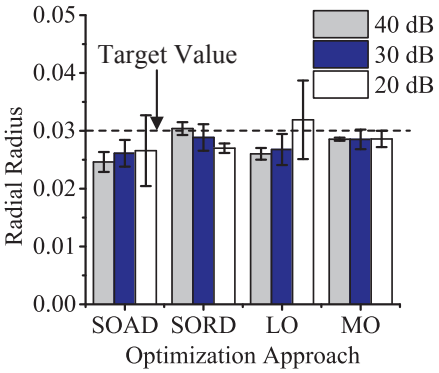

(b) Radial Radius

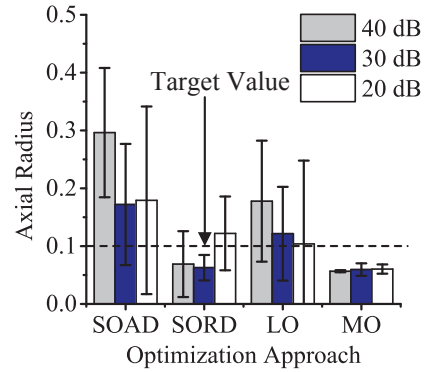

(c) Axial Radius

Figure 1.8: Mean and standard deviation (error bars) of the optimal erosion parameter solutions from each optimization approach: Single-Objective (SO) using either axial displacement (AD) or radial displacement (RD), Lumped-Objectives (LO), and Multi-Objective (MO) subject to the specified level of measurement noise after 6000 finite element analyses compared to the target (experimental) values for Example 1.

1.5.1.4 Measurement Sparsity There are commonly practical limitations on the number of measurements that can be obtained for any given nondestructive test (e.g., there are limits to the number of sensors that can be installed), and the amount of measurements is typically strongly correlated with the ill-posedness of the inverse characterization problem (i.e., less measurement data often leads to a higher likelihood of a nonunique solution and at least a more nonconvex error surface). Therefore, for the last set of tests for Example 1, varying numbers of discrete (noise-free) measurements of the axial and radial displacement along the pipe surface were utilized within the optimization approaches and the evaluation results were again analyzed and compared. In addition to the original 99 measurement points equally spaced at 1 *cm* intervals, two additional cases were examined: 24 locations at 4 *cm* intervals and 9 locations at 10 *cm* intervals. The three optimization approaches were again applied with each quantity of experimental data, in turn, for five independent trials each with the stopping criteria set to 6000 finite element analyses.

Fig. 1.9 shows the mean and standard deviation of the measurement error for the axial displacement and radial displacement produced through five trials of each optimization approach with each case of measurement point intervals. There is negligible difference in the results for measurement intervals of 1 *cm* and 4 *cm*, implying that both data quantities have sufficient information to determine a unique and accurate solution, particularly when provided with the optimization capabilities of the multi-objective approach. Alternatively, there is a substantial difference in the resulting error minimization for measurement intervals of 10 *cm* when compared to the larger experimental datasets. There is clearly convergence to local minima and there was substantial variation in the resulting erosion parameter estimates (not shown for brevity), indicating that the nondestructive test performed with surface measurements at 10 *cm* intervals is insufficient to produce unique and accurate damage estimates and produces a substantially more nonconvex error surface than the cases with more measurement information. However, the multi-objective approach was able to minimize the measurement error consistently to a far lower value than the single-objective approaches, and although there was higher deviation in the solutions than previously, the multi-objective approach produced more accurate damage estimates than the single-objective strategies even when using more dense measurements.

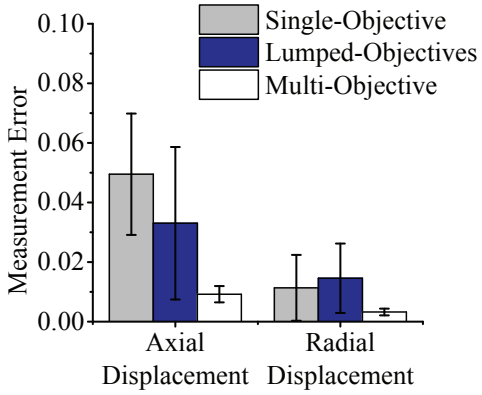

(a) 1 cm

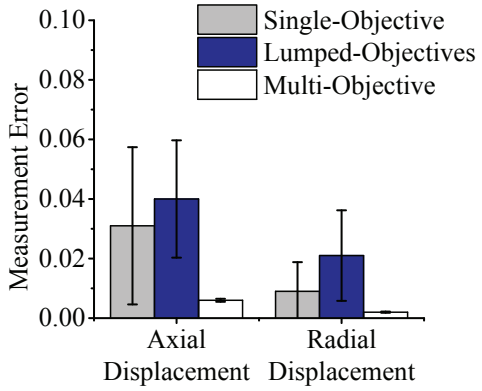

(b) 4 cm

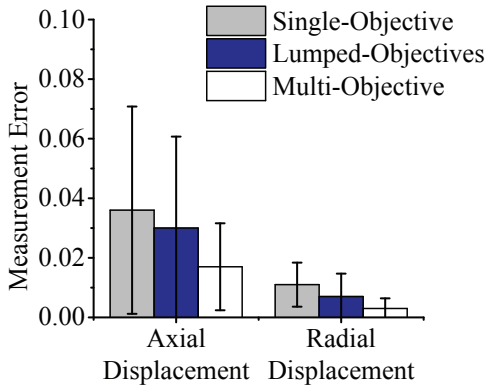

(c) 10 cm

Figure 1.9: Mean and standard deviation (error bars) of the measurement error for each optimization approach subject to the specified measurement point intervals after 6000 finite element analyses for Example 1.

1.5.2 Example 2: Simulated Plate With Holes

A second set of simulated test cases for a different inverse characterization example was considered in order to examine the capabilities of the multi-objective approach to generalize to other similar NDE problems in solid continua. This second example consisted of evaluation of a simulated steel plate to determine the unknown size and location of small circular holes occurring throughout the domain. As shown in Fig. 1.10, the plate was taken to be an arbitrarily thin 1 $m \times 1$ m square section with the bottom fixed to a rigid support. The

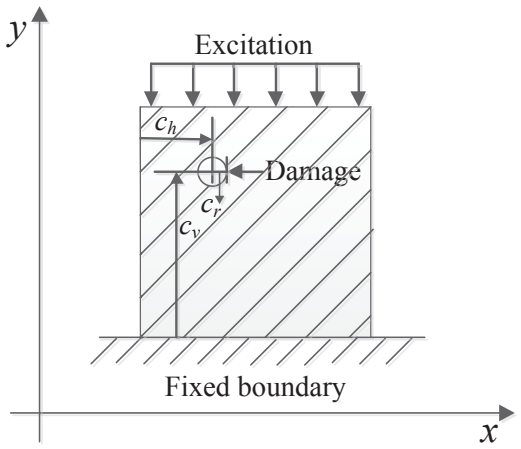

Figure 1.10: Schematic of the damaged plate structure for Example 2.

elastic material properties were defined identically to the previous pipe example, and again the material properties were assumed to be unaffected by damage (i.e., damage only changed geometry).

To generate the experimental data circular regions representing the damage defined by the horizontal and vertical coordinates of their centers (c_h and c_v) and corresponding radii (c_r) were removed from the plate. As in the previous example, the circular assumption was used for simplicity and its similarity to previous related NDE efforts [36, 43, 20, 7, 40, 21]. The simulated nondestructive test consisted of applying a 1 kN/m (factoring out the arbitrary thickness) harmonic excitation to the top surface of the plate and measuring the vertical and/or horizontal displacements at several locations (detailed in the following) on

Table 1.2: Target (experimental) values for the unknown damage centroid horizontal and vertical coordinates (c_h and c_v) and radius (c_r), and the minimum and maximum values considered for the optimization search process for the example plate structure with a single damage location.

Damage Parameter	Target Value	Optimization Minimum	Optimization Maximum
c_h	0.3	0.0	1.0
c_v	0.7	0.0	1.0
c_r	0.05	0.0	1.0

the surface of the plate, and all simulations utilized the plane stress assumption. In addition, Gaussian white noise was added to the experimental data with a SNR of 40 dB.

1.5.2.1 Single Damage Location For the first set of tests a single damage location was used to generate the simulated experiment, and then the inverse characterization problem sought to determine the location and size of this single damage. Table. 1.2 shows the target values for the unknown damage parameters and the minimum and maximum values considered reasonable for each parameter for the inverse solution process. For the measurement data both the horizontal and vertical displacements resulting from the applied harmonic excitation were measured at 19 locations along the right surface of the plate that were equally-spaced vertically in 5 cm increments. Again, the data was divided into two objectives with the vertical displacement measurements used to form the first objective (γ_1) and the horizontal displacement measurements used to form the second objective (γ_2).

The same three optimization strategies as were used in the previous example (Lumped-, Single-, and Multi-Objective) were each applied to estimate the location and size of the unknown damage in the plate, again with five trials for each optimization approach and with a stopping criteria of 2000 total finite element analyses for each trial. The stopping criteria

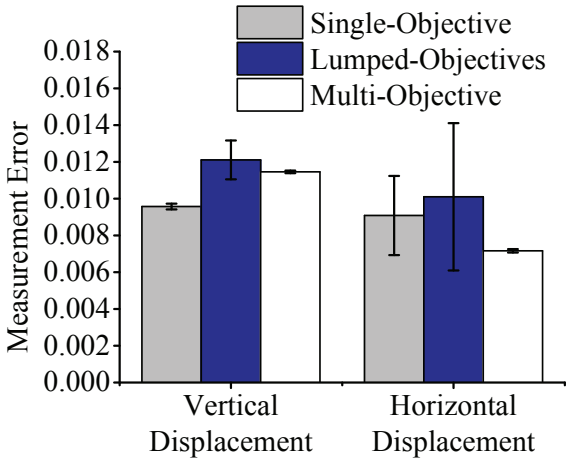

Figure 1.11: Mean and standard deviation (error bars) of the measurement error for each optimization approach after 2000 finite element analyses for Example 2 with a single experimental damage location.

was deemed sufficient for this example to ensure all optimization trials reached convergence (whether to a local or global minimum). Fig. 1.11 shows the mean and standard deviation of the measurement error for the vertical displacement (γ_1) and the horizontal displacement (γ_2) and Fig. 1.12 shows the mean and standard deviation of the damage parameter values produced by the solutions obtained from the five trials of each optimization approach. Similarly to the first example, the Multi-Objective approach showed a superior ability to minimize all measurement errors, and therefore, produced more accurate estimates to the damage parameters than any of the Single- or Lumped-Objective approaches. Moreover, the Single-Objective results when using only the vertical displacement are noticeably more accurate than either the Single-Objective approach with the horizontal displacement or the Lumped-Objective approach. These results again imply that one measurement quantity was more sensitive to the damage parameters than the other, and when combining the two measurement groupings the Lumped-Objective approach is negatively affected by the additional data, whereas the Multi-Objective strategy benefits from all information available.

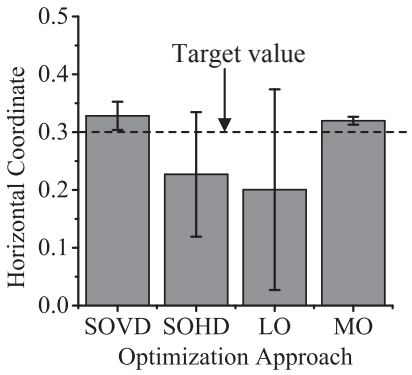

(a) Horizontal Coordinate

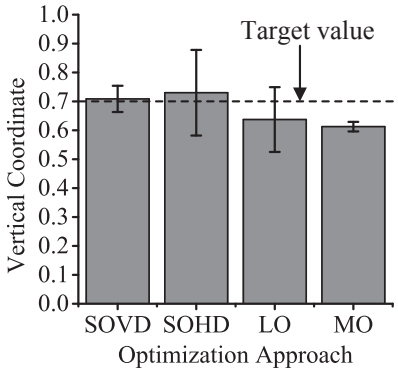

(b) Vertical Coordinate

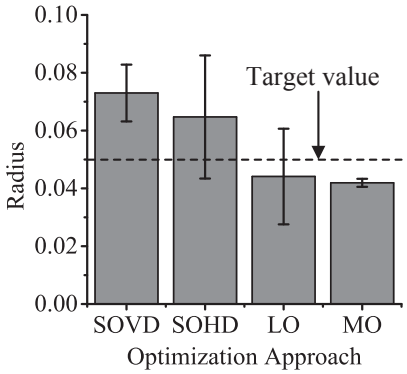

(c) Radius

Figure 1.12: Mean and standard deviation (error bars) of the optimal damage parameter solutions from each optimization approach: Single-Objective (SO) using either vertical displacement (VD) or horizontal displacement (HD), Lumped-Objectives (LO), and Multi-Objective (MO) after 2000 finite element analyses compared to the target (experimental) values for Example 2 with a single experimental damage location.

1.5.2.2 Multiple Damage Locations In contrast to all of the previous examples, the last set of tests was intended to examine the capabilities of the Multi-Objective optimization approach for problems in which the "true" solution does not exist in the optimization search space, leading to a higher propensity for multiple global (or nearly global) minima that have substantially different parameter values. Therefore, for the final set of tests two damage locations were used to generate the simulated experiment, but the inverse characterization problem sought to determine the location and size of only a single damage. Table. 1.3 shows the experimental ("true") values of the damage parameters for the two damage locations, and the same minimum and maximum values for the damage parameters as were used for the previous example and shown in Table. 1.2 were employed for the optimization process to determine the estimated single damage location.

Table 1.3: Target (experimental) values for the unknown damage centroid horizontal and vertical coordinates (c_h and c_v) and radius (c_r) for each damage location for the example plate structure with two damage locations.

Damage Parameter	Target Value 1	Target Value 2
c_h	0.7	0.7
c_v	0.7	0.3
c_r	0.05	0.05

For the measurement data only the horizontal displacements resulting from the applied harmonic excitation were measured at 99 locations that were equally-spaced vertically in 1 cm increments along both the left and right surfaces of the plate. The measurements were divided into two objectives with the displacement measurements from the left surface used to form the first objective (γ_1) and the displacement measurements from the right surface used to form the second objective (γ_2).

For these final tests the focus was on the ability of the stochastic optimization approaches to maintain diversity in their solution populations and ultimately reveal multiple potential solutions when they exist. As such, for simplicity only the Multi-Objective and the Lumped-Objective approaches were applied to the multiple damage location cases to estimate the

location and size of a single unknown damage in the plate, again with five trials for each optimization approach and with a stopping criteria of 2000 total finite element analyses for each trial. Furthermore, to examine the capabilities to maintain solution diversity and reveal multiple possible damage characterization results the analysis of the trial results focused on the solution distribution in the final populations of the optimization cases. In particular, for the Multi-Objective approach the analysis focused on the distribution of characterization solutions on the resulting Pareto fronts, which given the Pareto fraction used of 0.35 produced 14 solution estimates at the completion of optimization. Alternatively, since the Lumped-Objective strategy does not specifically produce a Pareto front, simply the 14 individuals in the final population with the best combined fitness (according to Eqn. (2.7)) were extracted and analyzed at the completion of optimization.

The results of the five optimization trials were consistent, and therefore, a representative example from the five trials of each optimization approach are presented. Fig. 1.13 shows the overall distribution as well as the mean and standard deviation of the measurement error for the left surface horizontal displacement (γ_1) and the right surface horizontal displacement (γ_2) from the 14 optimal solution sets obtained in one trial of the Multi-Objective strategy and one trial of the Lumped-Objective strategy. Overall, the resulting measurement errors were considerably higher for all cases in comparison to the previous examples, particularly the right surface measurements, which is expected since the parameterization of the characterization problem can not capture the "true" solution used to generate the experimental data. However, the distribution of measurement errors in the populations of the two optimization approaches (Multi- and Lumped-Objective) are considerably different from each other. The Lumped-Objective strategy yielded a population with consistently lower total error (left and right surface) than the Multi-Objective approach, although still with error high enough to suggest the characterization problem failed to find an accurate damage representation (as expected). More importantly, the Lumped-Objective results consistently converged to an entire population (considering even the entire final population of 40 and not just the 14 plotted herein) with nearly the same level of error, whereas the Multi-Objective approach had significant diversity in the measurement errors for the solutions in the final Pareto set and in many cases with substantially lower measurement error for the

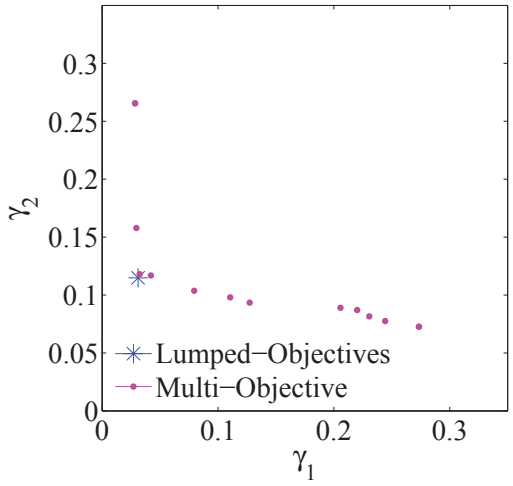

(a)

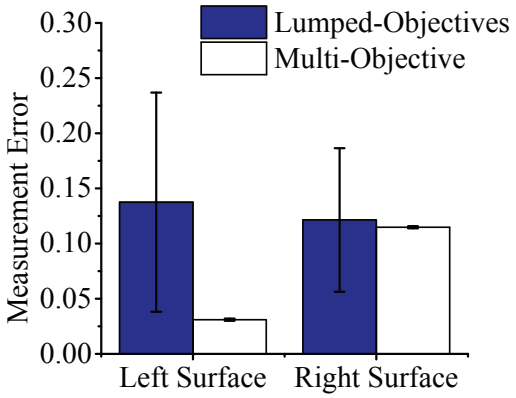

(b)

Figure 1.13: (a) Distribution and (b) mean and standard deviation of the measurement error for the 14 individuals in the Pareto set from a representative trial of the Multi-Objective optimization approach and the 14 individuals with the lowest total measurement error in the final population from a representative trial of the Lumped-Objective optimization approach after 2000 finite element analyses for Example 2 with two experimental damage locations.

right surface measurements. Moreover, as shown in Fig. 2.1 for the corresponding 14 solution estimates for the plate damage in comparison to the "true" (i.e., target) damage, the Lumped-Objective approach converged the entire population to essentially a single solution estimate, providing for minimal insight into the nature of the "true" solution in this failed characterization attempt. By contrast, the Multi-Objective approach produced a diverse set of solution estimates, that for this specific example, happen to cluster near to the two "true" damage locations. As such, there is clearly a benefit to utilizing a Multi-Objective optimization strategy for such a characterization problem to maintain diversity in the solution population. Specifically, the Lumped-Objective results provide minimal insight into potential follow-up strategies to solve the characterization problem more accurately, such as suggesting the "true" number of damage locations or allowing application of coevolutionary strategies to design an improved nondestructive test [35, 34]. Whereas, the results of the Multi-Objective optimization presented could be interpreted to suggest optimization should be repeated with an assumption of two damage locations in the plate and potentially lead to an accurate estimate of the "true" solution. Although, more investigation is required to deduce the ability of a Multi-Objective optimization approach to consistently produce estimates to multiple damage locations under the assumption of only a single damage for the optimization process.

1.6 CONCLUSIONS

A multi-objective optimization-based computational inverse problem solution method for damage characterization in solid continua was presented. In general, the procedure was shown to be a relatively simple change to the standard optimization-based NDE strategies, while providing a substantial improvement in the capabilities to maintain a high level of diversity in the solution population during the search process, and therefore, traverse the optimization search space to minimize the measurement error and produce accurate damage estimates. Within the context of genetic algorithm optimization, the capabilities of a mulit-objective approach were displayed quantitatively in comparison to standard approaches of

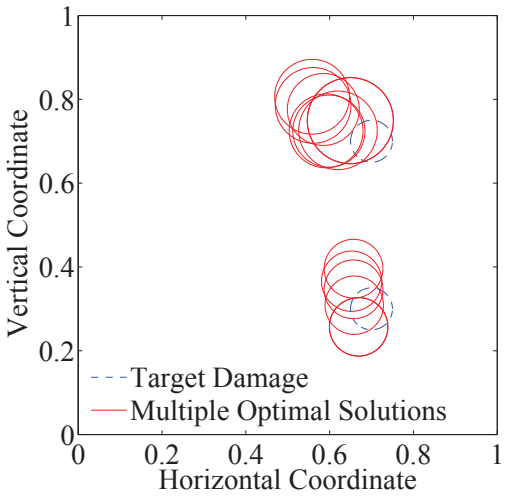

(a)

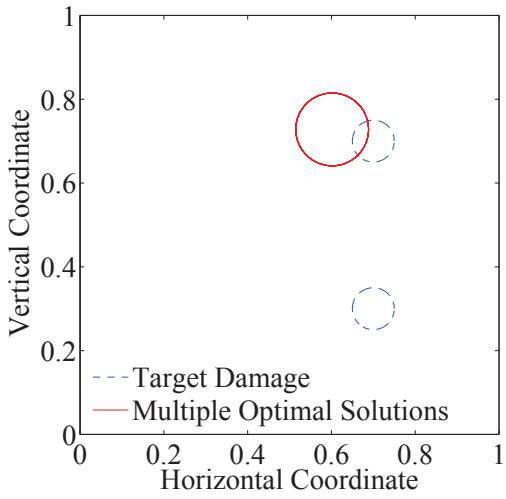

(b)

Figure 1.14: Distribution of the optimal damage solution estimates compared to the "true" (target) damage solution for (a) the 14 individuals in the Pareto set from a representative trial of the Multi-Objective optimization approach and (b) the 14 individuals with the lowest total measurement error in the final population from a representative trial of the Lumped-Objective optimization approach after 2000 finite element analyses for Example 2 with two experimental damage locations.

casting the NDE problem in terms of a single objective through a numerical study of two simulated damage characterization problems based on vibration testing using direct frequency response displacement measurements. Through the example of a steel pipe structure with inner wall erosion damage, the multi-objective approach was shown to improve both efficiency and accuracy of the NDE process, while also having improved tolerance to measurement noise and measurement sparsity in comparison to equivalent single-objective techniques. In addition, an example of identifying holes within a steel plate showed that the multi-objective approach was capable of some degree of generalization to alternate NDE problems. Moreover, the plate example showed that the multi-objective approach can provide a substantial benefit in NDE problems where no accurate solution and/or multiple solutions may exist. By providing diverse solution estimates the multi-objective approach may better indicate the actual solution space when a solution does not exist within the current parameterization or otherwise provide insight into potential changes to the testing or parameterization to produce more accurate and unique solutions to the NDE problem.

2.0 A COMPUTATIONAL NONDESTRUCTIVE EVALUATION ALGORITHM COMBINING SELF-EVOLVING PARAMETERIZATION AND MULTI-OBJECTIVE OPTIMIZATION FOR QUANTITATIVE DAMAGE CHARACTERIZATION

2.1 ABSTRACT

A self-evolving parameterization approach for nondestructive evaluation (NDE) of damage in structural components is presented and numerically evaluated. Focused herein on problems relating to characterizing an unknown quantity of localized changes in properties, the adaptive approach utilizes the substantial solution diversity that is uniquely provided by multi-objective optimization to iteratively build up the parameterization and accurately characterize all localized property changes with the minimum dimensional parameterization. Through simulated test problems based on the characterization of damage within plates, the NDE approach with self-evolving parameterization is shown to provide an accurate and efficient process for the solution of inverse characterization problems.

2.2 INTRODUCTION

Computational inverse mechanics approaches for nondestructive evaluation (NDE) that combine computational mechanics and nonlinear optimization are uniquely well-suited for quantitative inverse characterization for a variety of engineering systems and physical properties, particularly when measurement information is limited [8, 10, 62, 9, 81, 5]. However, these approaches can often become computationally prohibitive, particularly since the computational

expense of the inverse problem solution procedure for many commonly used algorithms (e.g., non-gradient-based optimization approaches [9]) increases significantly with the dimensionality of the parameterization of the unknown variable(s) to be determined (e.g., the number of unknown material parameters). Therefore, it is of paramount importance in many applications to carefully select an efficient parameterization that can represent the nature of the potential inverse problem solutions accurately with a minimal number of parameters.

To maintain reasonable computational efficiency, many applications will attempt to utilize *a priori* knowledge of the potential inverse problem solution space to select a parameterization with relatively few coefficients to be determined. For example, in several applications the spatial distribution of a quantity (e.g., material property) to be determined is known *a priori* to be spatially localized in nature. For such a localized property a parameterization that utilizes basis functions with compact or quasi-compact support in combination with parameters defining the location information for these basis functions (e.g., the center point of the basis function) may lead to being able to use a relatively small number of these basis functions and require substantially fewer parameters to be determined by the inverse routine in comparison to a more generalized dense point-by-point (or element-by-element) parameterization. Examples of such implementations include [1], which used Gaussian radial basis functions to parameterize the distribution of elastic modulus for applications in tissue (particularly tumor) characterization, [71], which assumed that corrosion damage of internal pipe walls could be parameterized as a small number of elliptic regions of material loss, and [68], which used so-called "damage functions" that amounted to using a coarse finite element-type mesh to describe the damage in a reinforced concrete beam in terms of the length-wise distribution of the elastic modulus and thereby restrict the number of search parameters. However, these approaches may also present significant challenges, including a potential that the parameterization will be too restricted, possibly leading to nonexistence issues in that a sufficiently accurate solution will not exist, whereas if a relatively large number of basis functions are utilized then the likelihood of a sufficient solution existing increases, but computational expense and/or nonuniqueness may similarly increase.

To further improve the solvability of inverse characterization problems with known localized spatial distributions, some methods have been developed that utilize multi-stage

inverse solution procedures. These multi-stage procedures typically begin with some form of a localization algorithm to first identify the region of the unknown localized change in properties, and thus reduce the spatial search domain (and computational expense) for the subsequent stages. The work in [54] extended the previously mentioned "damage function" approach applied to beam structures by introducing a multi-stage scheme that first used a coarse mesh parameterization to identify the damage region(s) and then applied a finer mesh parameterization to these regions in subsequent steps to refine the solution approximation. Similarly, several works have developed approaches that use modal analysis to localize regions of property changes and then apply various approaches to efficiently create a more refined/accurate approximation [33, 24, 80, 44]. There have also been similar efforts for characterization problems in solid continua, which can often be even more challenging to parameterize efficiently than those problems using structural simplifications. One approach that has shown significant potential for being applicable to efficiently characterizing spatially localized properties in continua being developed relies primarily on the concept of topological derivatives [20, 25, 7]. For instance, the work in [20] presented an approach that used the topological derivative field to efficiently create an estimate of the geometry of an inclusion (i.e., scatterer) in a transparent homogeneous medium, which could directly provide the inverse solution estimate or potentially be refined further with a subsequent more standard iterative optimization-based inverse characterization approach. However, the topological derivative approach is thus far only directly applicable to cavity or inclusion problems and requires extensive mathematical formulation that is dependent upon the governing physics of the problem. Moreover, while many other of these multi-stage approaches (including those discussed previously) are less complex to implement, they are similarly difficult to generalize, whether to more complicated structures/systems, to alternate physics/testing methods, or to non-binary and/or continuously distributed properties.

With a particular focus on accurate and efficient characterization of an unknown quantity of localized changes in properties in solid continua, the current work presents an algorithm to automatically evolve the parameterization for inverse characterization utilizing a computational inverse mechanics approach with multi-objective optimization. This adaptive approach utilizes the substantial solution diversity that is uniquely provided by multi-objective

optimization in combination with an *ad hoc* clustering algorithm to iteratively expand the parameterization of the inverse problem and accurately characterize all localized property changes computationally efficiently with the minimum dimensional parameterization. In the following section the general framework for nondestructive evaluation utilizing multi-objective optimization is outlined. Then, the self-evolving parameterization algorithm is presented, including a detailed explanation of the *ad hoc* clustering algorithm and decision criteria used to automatically expand the parameterization. Lastly, numerically simulated examples relating to characterization of localized regions of material loss in structures from frequency-response-based testing are presented to examine the capabilities of the NDE algorithm with self-evolving parameterization, which is followed by the concluding remarks.

2.3 NONDESTRUCTIVE EVALUATION UTILIZING MULTI-OBJECTIVE OPTIMIZATION

While an adaptive parameterization strategy could be of use within the context of a variety of inverse problem application areas, the primary focus of the present work is NDE. In particular, the overarching focus herein is on NDE of solid continua given some nondestructively tested response field measurements over some portion of the domain of the structure/solid. Furthermore, this work will utilize the common approach of casting the inverse characterization problem as an optimization problem to determine the unknown parameters of the structure to minimize the difference between the measured response and those predicted by a numerical representation of the structure (e.g., finite element or boundary element analysis) subject to the nondestructive testing conditions, such as

$$\underset{\vec{\alpha}}{\text{Minimize}} \; \|\vec{R}^{sim}(\vec{\alpha}, \vec{x}) - \vec{R}^{exp}(\vec{x})\|_{\Gamma}, \tag{2.1}$$

where $\vec{\alpha}$ is the vector of parameters to be determined to characterize the desired structural properties, $\vec{R}^{sim}$ is the simulated response field to estimate the nondestructive test (NDT) response for a given set of parameters, $\vec{R}^{exp}$ is the experimentally measured response field (i.e., optimization target), and $\|\cdot\|_{\Gamma}$ is some suitable metric norm with respect to the domain,

Γ, of the nondestructive measurements. This type of optimization strategy to approximate the solution of inverse characterization problems provides several benefits, including the capability to address a variety of physical processes/measurements, even simultaneously, and providing quantitative results. However, there are also inherent challenges in addition to the ubiquitous ill-posedness associated with inverse problems, most prevalent being the large computational expense of this optimization approach. In many implementations the computational expense of the numerical approximation of the structural response (i.e., forward problem) is substantial. In addition, many optimization algorithms require a large number of objective functional evaluations to identify a suitable minimum. Therefore, the combination of the forward problem expense and the number of functional evaluations required can lead to this optimization approach to the inverse solution approximation becoming impractical. Thus, considerable effort is often placed on improving this computational expense for this type of optimization strategy for the solution of inverse problems in mechanics [10, 9, 32, 48].

Previous work of the authors [71] showed a simple yet effective approach to utilize multi-objective optimization rather than the standard single objective optimization (as shown in Eqn. (2.3)) to substantially reduce the computational expense and improve the consistency of the solution accuracy for inverse characterization of solid continua. The key to the approach is as simple as dividing up the measurement components or spatial distribution into several separate objective functionals to be minimized simultaneously, but separately, which could be viewed as (e.g., for the case of dividing the spatial distribution of the measurements)

$$\underset{\vec{\alpha}}{\text{Minimize}} \begin{cases} \|\vec{R}^{sim}(\vec{\alpha},\vec{x}) - \vec{R}^{exp}(\vec{x})\|_{\Gamma_1} \\ \|\vec{R}^{sim}(\vec{\alpha},\vec{x}) - \vec{R}^{exp}(\vec{x})\|_{\Gamma_2} \\ \vdots \\ \|\vec{R}^{sim}(\vec{\alpha},\vec{x}) - \vec{R}^{exp}(\vec{x})\|_{\Gamma_n} \end{cases}, \tag{2.2}$$

where Γ_i is the i^{th} subdivision of the domain of the response field measurements obtained from nondestructive testing and n is the total number of subdivisions. Then, any preferred multi-objective optimization algorithm can be employed to determine the Pareto front for (2.2), which can be thought of as the set of all possible solutions to the inverse problem that

have a lower value for at least one of the separate objective functionals in comparison to any other solution estimate seen throughout the optimization process. The previous work of the authors employed a controlled elitist multi-objective genetic algorithm (CEMGA) [16, 17] to determine the Pareto front in the example cases considered therein. When the multi-objective optimization process is complete, a single solution estimate for the inverse problem can be attained through some chosen final decision criteria, such as the minimum sum of all objective functionals, e.g.,

$$\underset{\vec{\alpha}\in\{\vec{\alpha}_i\}_{i=1}^{p}}{\text{Minimize}} \sum_{j=1}^{n} \|\vec{R}^{sim}(\vec{\alpha},\vec{x}) - \vec{R}^{exp}(\vec{x})\|_{\Gamma_j}, \tag{2.3}$$

where $\{\vec{\alpha}_i\}_{i=1}^{p}$ is the set of p potential solutions identified as part of the Pareto front. Note that there are many other "postprocessing" methods available to select the final solution estimate from the Pareto front, with the basic equation above being a potentially suitable heuristic choice in cases where the measurement quantities have similar magnitudes and physical meaning, for example.

The primary feature of the multi-objective optimization that leads to improved inverse solution capabilities is that substantial diversity of the solution estimates is maintained throughout the search process by evolving a set of optima (i.e., the Pareto front) rather than a single optimum throughout an iterative optimization process. By maintaining diversity, the multi-objective optimization process is uniquely able to traverse the large parameter search spaces that are typical of inverse characterization problems efficiently and consistently, avoiding stalling and convergence to local minima. An additional benefit of the diversity in the solution estimates provided by multi-objective optimization, which is particularly relevant to the present work, is the resulting improvement in the ability to reveal the variety of solutions that may exist for ill-posed (particularly non-unique) problems.

As a direct reason for non-uniqueness can be insufficiency of the parameterization of the properties to be determined, the solution diversity provided by multi-objective optimization can thus be assumed to be able to provide insight into the changes to the parameterization necessary to subsequently produce more unique and accurate inverse solutions. As a simple example of this potential from the previous study by the authors, Fig. 2.1 shows the Pareto front solutions from a multi-objective optimization process to estimate the size and location

of circular loss of material within a plate from numerically simulated NDT data (see [71] for all details of this particular example problem).

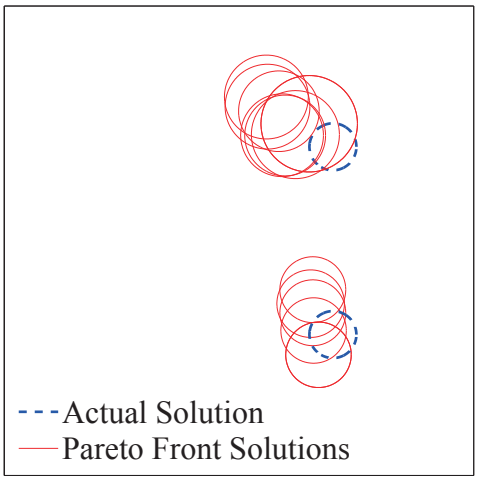

Figure 2.1: Distribution of the Pareto front solution estimates from multi-objective optimization having assumed one region of material loss compared to the two "actual" regions of material loss used to simulate the experimental measurements for a numerically simulated nondestructive evaluation problem of damage characterization in a plate structure.

Of particular importance is that the NDT data was simulated for this example from a computational analysis with two circular voids (i.e., the true/correct solution to the NDE problem should be two circular voids), while the inverse characterization process was performed assuming that there was only one circular void. Naturally, none of the obtained Pareto front solutions that are shown here minimized the total measurement error particularly well, implying that no "true" solution was found. However, the distribution of these "best" possible solutions given the assumption of only one circular void shows distinct clusters surrounding the two actual voids used to simulate the NDE (i.e., the correct solution). In other words, the set of Pareto front solutions obtained for this example problem quite clearly provides intuitive evidence of how the parameterization (i.e., selection of the number of voids to search for) could be improved towards achieving an accurate inverse solution estimate. Extending this concept, the present study focused on the development of a strategy to improve solution capabilities for this and similar classes of inverse characterization prob-

lems utilizing this diversity provided by multi-objective optimization through a self-evolving parameterization approach.

2.4 NONDESTRUCTIVE EVALUATION WITH SELF-EVOLVING PARAMETERIZATION

To provide additional context, the following discussion will provide example scenarios based upon the class of NDE problems relating to characterizing an unknown quantity of localized changes in properties (e.g., damage or defect characterization). However, this approach should be able to be similarly implemented for a variety of inverse characterization problems, particularly those for which some property of the unknown field is known *a priori* to be (semi-) localized in the parameter space. The overall structure of the optimization-type NDE algorithm incorporating an adaptive self-evolving parameterization approach is shown in Fig. 2.2.

The algorithm begins with some minimum parameterization of the inverse characterization problem (i.e., a parameterization of the unknown field of the inverse problem with a minimum number of parameters to be determined subject to constraints of the system and any *a priori* physical information). For a localized damage characterization problem, this could imply first assuming that there is a single localized region of damage. The multi-objective optimization solution approach is then applied to determine the Pareto front of potential solutions to the characterization problem (e.g., the set of potential damage locations and associated breadth and magnitude). Next, the self-evolving parameterization step is employed, including an *ad hoc* hierarchical clustering algorithm to determine whether there are any distinct clusters of Pareto front solutions in the parameter space (e.g., distinct spatial groupings of damage locations, such as the two groupings shown in Fig. 2.1), and if so, then how many clusters exist. Based upon the number of parameter clusters a decision criteria is employed to expand the parameterization (e.g., based on the results shown in Fig. 2.1 assume the parameterization should allow for two damage locations). If no additional clusters are found for a given iteration, then the algorithm is completed and the "best" possible char-

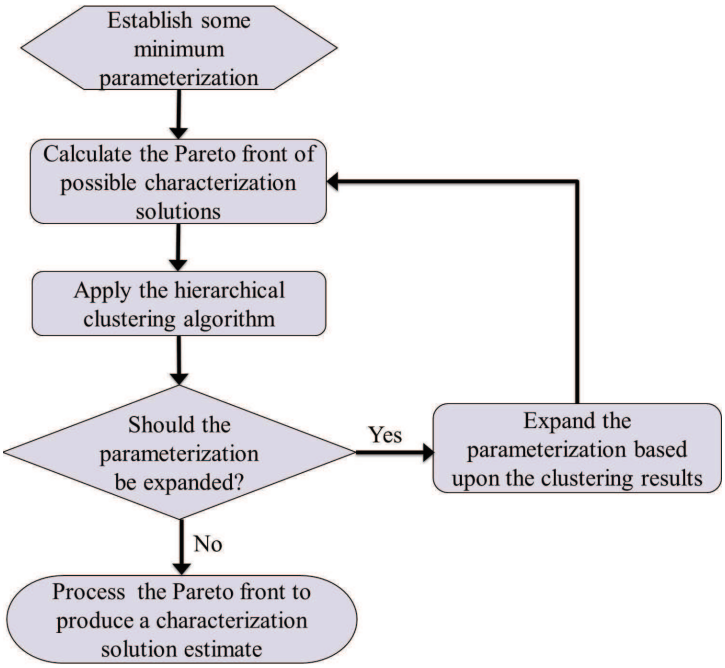

Figure 2.2: Flowchart of the optimization-type NDE algorithm with adaptive self-evolving parameterization.

acterization solution is chosen from the current Pareto front. Otherwise, the multi-objective optimization solution approach is applied again with the updated parameterization and the process is repeated until the parameterization converges or a maximum number of iterations have been performed. The hierarchical clustering algorithm and parameterization expansion decision criteria comprising the self-evolving parameterization component of the algorithm are elaborated upon in the following.

As stated, the core hypothesis of the self-evolving parameterization component of the algorithm developed is that the distribution of solutions in the parameter space produced through multi-objective optimization provides guidance as to whether a specific physical parameter should be expanded. In the localized property characterization context, in which the primary method to expand the parameterization could be to increase the number (n) of basis functions with compact (or semi-compact) support used to define the property distribution along with their associated unknown parameters to be determined by the inversion, the self-evolving parameterization component of the characterization algorithm could be implemented as follows:

Given - The Pareto front of potential solutions to the inverse characterization problem (e.g., spatial coordinates of the centroid for each localized property change and any associated parameters) subject to the current value of n (i.e., the number of compactly or quasi-compactly supported basis functions used to define the localized change).

Step 1 - Identify the n+1 regions of localized property change whose centroids are separated by the largest Euclidean distance from the entire Pareto set of solutions (noting that each solution set could contain multiple localized property changes depending on the value of n), referred to as the $n + 1$ "Parameterization Poles".

Step 2 - Identify and average all regions of localized property changes that overlap with each Parameterization Pole to produce the $n + 1$ "Cluster Means" of the localized property changes.

Step 3 - Do any of the Cluster Means overlap?

Yes $\rightarrow$ STOP (do not update the parameterization further).

No $\rightarrow$ SET $n = n + 1$ and GO TO Step 1.

2.5 EXAMPLES AND DISCUSSION

To examine the capability of the self-evolving parameterization approach utilizing multi-objective optimization for NDE to efficiently and accurately characterize localized property changes in solid continua several simulated examples of damage characterization within structural steel plates (as could potentially be affected by erosion) were considered. More specifically, the example NDE cases sought to characterize the size and location of circular regions of material loss within the steel plates considered. This circular defect assumption was used for simplicity and based on several other related NDE works by a variety of authors that used a similar assumption [43, 20, 36, 7, 21, 40]. The material behavior for all cases was defined as linear elastic with a Young's modulus of 200 GPa, Poisson's ratio of 0.3, and density of 8000 kg/m^3, and all properties were assumed to remain as defined following damage (i.e., the erosion damage being characterized in this simulated problem was assumed to occur without any observable change to the properties of the remaining material in the structure, and therefore only changed the structure's geometry). In all cases the simulated nondestructive tests consisted of applying a harmonic pressure to a portion of the structure at an excitation frequency of 20 Hz, and then measuring the resulting steady-state harmonic displacement amplitudes at several discrete locations along the outer surface of the structure. Vibration testing using direct frequency response measurements was chosen based on its documented ability to provide substantial diagnostic information for a global evaluation of a structure [11, 39, 3]. However, the overall inverse characterization approach and corresponding benefits would be expected to yield similar results for alternate testing approaches.

For both generating the experimental data and simulating the forward problem during the inverse solution process the structures were assumed to behave linearly and be defined by steady-state dynamic plane stress solid mechanics, and all analyses were performed using the finite element method. Standard linear plane stress continuum elements were employed, and the mesh sizes were ensured to be sufficiently small through mesh convergence to provide accurate analysis for all cases considered. In addition, for all analyses the meshed domains remained constant describing the geometry of a healthy structure (i.e., structure without

damage), and the damage was modeled as total material loss within the specified regions by reducing both the Young's modulus and density to negligibly small values at all integration points within the specified damage regions. This modeling procedure for the inverse simulations allowed the numerical analyses to be efficiently parameterized for the optimization process. To add realism and to alleviate the inverse crime inherent in simulated experiments Gaussian white noise was added to the simulated experimental measurements as

$$U^{expn} = U^{exp}\left(1 + kv\right), \tag{2.4}$$

where U^{expn} and U^{exp} are the experimental displacement measurements with noise and without noise, respectively, k is the noise amplitude multiplier, and v is a normally distributed random variable with unit variance and zero mean. For the majority of cases examined here (only the results discussed in Section 2.5.1.3 used a higher noise level) k was chosen as 0.01 to produce an approximate signal to noise ratio (SNR) of 40 dB, which was deemed to be a sufficiently realistic value, calculated as

$$SNR(dB) = 10log_{10}\left(\frac{1}{k}\right)^2. \tag{2.5}$$

The inverse problems to determine the parameters defining the damage in the example structures were cast in the form of the following multi-objective optimization problem, arbitrarily having selected to divide the displacement measurements into four groupings based on measurement direction and spatial location,

$$\min_{\vec{\alpha}} \begin{cases} \gamma_1(\vec{\alpha}) = \left(\frac{\sum_{j=1}^{n}\left(U_{1j}^{exp} - U_{1j}^{sim}(\vec{\alpha})\right)^2}{\sum_{j=1}^{n}\left(U_{1j}^{exp}\right)^2}\right)^{1/2} \\ \gamma_2(\vec{\alpha}) = \left(\frac{\sum_{j=1}^{m}\left(U_{2j}^{exp} - U_{2j}^{sim}(\vec{\alpha})\right)^2}{\sum_{j=1}^{m}\left(U_{2j}^{exp}\right)^2}\right)^{1/2} \\ \gamma_3(\vec{\alpha}) = \left(\frac{\sum_{j=1}^{k}\left(U_{3j}^{exp} - U_{3j}^{sim}(\vec{\alpha})\right)^2}{\sum_{j=1}^{k}\left(U_{3j}^{exp}\right)^2}\right)^{1/2} \\ \gamma_4(\vec{\alpha}) = \left(\frac{\sum_{j=1}^{l}\left(U_{4j}^{exp} - U_{4j}^{sim}(\vec{\alpha})\right)^2}{\sum_{j=1}^{l}\left(U_{4j}^{exp}\right)^2}\right)^{1/2} \end{cases}, \tag{2.6}$$

where $\vec{\alpha}$ is the vector containing the parameters of the unknown damage to be determined in the inverse problem, U_{1j}^{exp}, U_{2j}^{exp}, U_{3j}^{exp} and U_{4j}^{exp} are the experimentally measured displacement at the j^{th} measurement location in the four groupings, and U_{1j}^{sim}, U_{2j}^{sim}, U_{3j}^{sim} and

U_{4j}^{sim} are the numerically simulated displacement at the j^{th} measurement location in the four groupings. Note that it would certainly be possible to utilize additional or alternate competing objectives than those discussed in the following, such as measurements of different directional components and/or from alternate regions of the domain, and tests (not shown here for brevity) have been completed with such variations with results consistent with those presented herein. Beyond ensuring that the chosen measurement quantities were sensitive to the parameters of the unknown damage to be determined, the selection and division of the measurement data into the multiple objectives in the following case studies was entirely arbitrary. For the inverse solution process the parameters of the unknown damage to be determined were constrained such that all damage estimates were within the domain of the structure and were non-overlapping.

A CEMGA ([16, 17]) was applied to solve the constrained optimization problems in terms of the four objective functions outlined above for all examples considered. An initial population of 80 individuals was utilized for all cases, as well as scattered crossover, adaptive feasible mutation, and tournament selection. In all cases to ensure a fair comparison the stopping criteria for the optimization was set as a maximum number of 40 generations (which is equivalent to setting a maximum number of 3200 finite element analyses). To obtain a single solution estimate from the Pareto front of solutions provided by the CEMGA at completion of the inversion algorithm the Pareto front was postprocessed to select the one solution estimate with the minimum l_2-norm of the four objective functions as

$$\underset{\vec{\alpha}\in P}{min} \left(\gamma_1^2(\vec{\alpha}) + \gamma_2^2(\vec{\alpha}) + \gamma_3^2(\vec{\alpha}) + \gamma_4^2(\vec{\alpha})\right), \tag{2.7}$$

where P represents the set of Pareto front solution estimates obtained by the CEMGA. Note that there have been alternate methods used in related works to select the final inverse solution estimate for such results (e.g., [32]). However, since the measurement groupings used for the examples herein are physically similar quantities to each other, the above choice is somehow intuitively ideal, providing the optimal solution estimate in an average sense. In addition, due to the stochastic nature of the optimization solution strategy, the inverse problem solution procedure was repeated five times for all test cases to ensure that the results presented were consistent, yet results of only one representative trial from each test

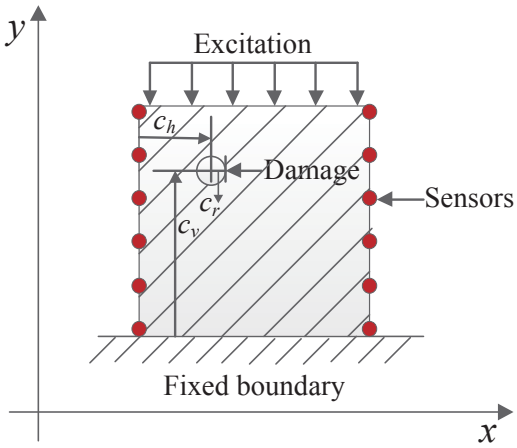

Figure 2.3: Schematic of the damaged square plate structure for Example 1.

case will be presented here for brevity and simplicity since the results were found to be highly consistent.

2.5.1 Example 1: Simulated Square Plate

The first set of example cases considered NDE of a simulated square steel plate to determine the size and location of a varying number of damages throughout the plate. As shown in Fig. 2.3, the plate was taken to be an arbitrarily thin 1 $m \times 1$ m square section with the bottom fixed to a rigid support.

The simulated NDT consisted of applying a 1 kN/m (factoring out the arbitrary thickness) harmonic excitation to the top surface of the plate and measuring the vertical and horizontal displacements at 99 equally-spaced increments along the left and right surfaces, as indicated in Fig. 2.3. The four objective functions for the multi-objective optimization were simply defined by dividing the measurements with respect to the two sides and the two directional components. In the following, three different damage scenarios are considered to explore the self-evolving NDE algorithm, which are primary distinguished by the number of "actual" damage locations to be determined (with the implication that the diffi-

culty of the NDE problem substantially increases with the number of damage locations to be determined).

2.5.1.1 One Damage Region This first case with one damage region was tested to not only examine the effectiveness for the simplest possible scenario, but to also show that the adaptive approach will typically not "over-evolve" the parameterization to overestimate the number of damaged regions provided that the algorithm begins with the minimum parameterization (e.g., parameterization for one damage region). Table 2.1 shows the actual values for the unknown damage parameters (i.e., values used to simulate the experimental measurements) and the minimum and maximum values (i.e., constraints) considered reasonable for each parameter for the inverse solution process.

Table 2.1: Actual (experimental) values for the unknown damage centroid horizontal and vertical coordinates (c_h and c_v) and radius (c_r), and the minimum and maximum values considered for the optimization search process for the example square plate structure with a single damage location.

Damage Parameter	Actual Value	Optimization Minimum	Optimization Maximum
c_h	0.3	0.0	1.0
c_v	0.7	0.0	1.0
c_r	0.05	0.0	0.5

Two versions of the inverse solution process were completed for this example, the first version starting the inverse solution process with the assumption of one damage region (i.e., 3 unknown parameters), and the second starting the inverse solution process with the assumption of two damage regions (i.e., 6 unknown parameters), effectively using twice the minimum parameterization for the problem in the second case. Fig. 2.4 shows representative examples of the Pareto front solution estimates (i.e., the distribution of all damage estimations in the Pareto fronts) from a single iteration of the two versions of the inverse solution process (i.e., without any evolution of the parameterization). In addition, Fig. 2.5 shows

the measurement error for the four objectives (γ_1, γ_2, γ_3, and γ_4) for the "best" individual (based on the criteria in (2.7)) from each of the Pareto fronts shown from the single iteration of the inverse solution process.

Of particular significance is that all damage estimates for the version that started with a single damage parameterization can be seen to be relatively closely clustered around the actual solution to the simulated inverse characterization problem, whereas there are three distinct clusters of damage estimates in the solution set that started with a two damage parameterization. The primary reason for the discrepancy between the results for the two different starting parameterizations is that the optimization process is considerably more challenging for the "over-parameterized" two damage parameterization case leading to the inability to sufficiently minimize the measurement errors and identify an accurate solution (Fig. 2.5), particularly in comparison to the single damage parameterization. Although the two damage parameterization can represent any scenario that the single damage parameterization can, the increase in the number of inaccurate solutions in the search space of the higher-dimensional parameterization substantially hinders the search process, which highlights one of the core motivations of the adaptive algorithm presented to keep the parameterization at a minimum. In addition, these results further display the importance of initializing the parameterization with the minimum physically meaningful number of parameters (e.g., begin the algorithm with a parameterization for a single damage region) in the context of the adaptive algorithm, as the results shown in Fig. 2.4 would actually lead to the parameterization being expanded further in the subsequent iteration to a three damage parameterization and likely lead to the solution diverging, while the single damage parameterization converged after a single iteration and the "best" solution estimate from this one iteration matched the actual solution nearly exactly (as shown in Fig. 2.6).

Simply put, there is no method to differentiate an insufficient error minimization caused by under-parameterization versus over-parameterization, since the relatively high measurement error for the two damage case could be caused by insufficient optimization iterations or insufficient parameterization, and therefore it is critically important to build up the solution approximation from the minimum possible parameterization.

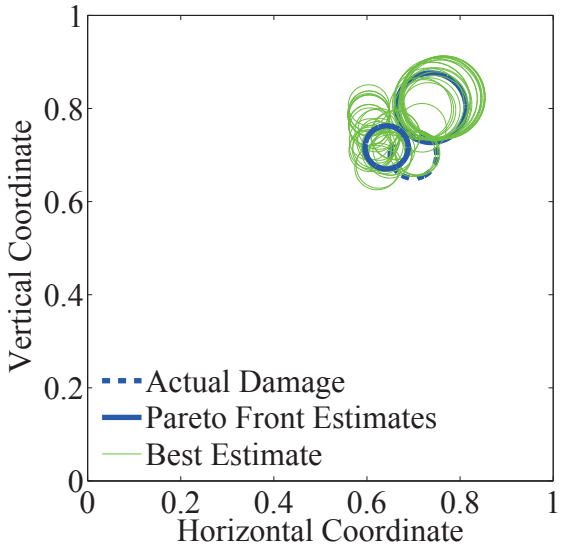

(a)

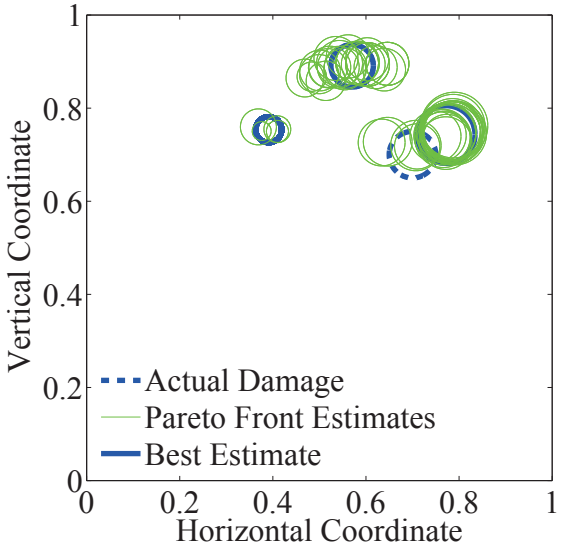

(b)

Figure 2.4: Representative results of the Pareto front damage region solution estimates obtained from multi-objective optimization (a) with the assumption of one damage region and (b) with the assumption of two damage regions, along with the "best" individual from each Pareto front, and compared to the actual (experimental) single damage region for the simulated example square plate structure.

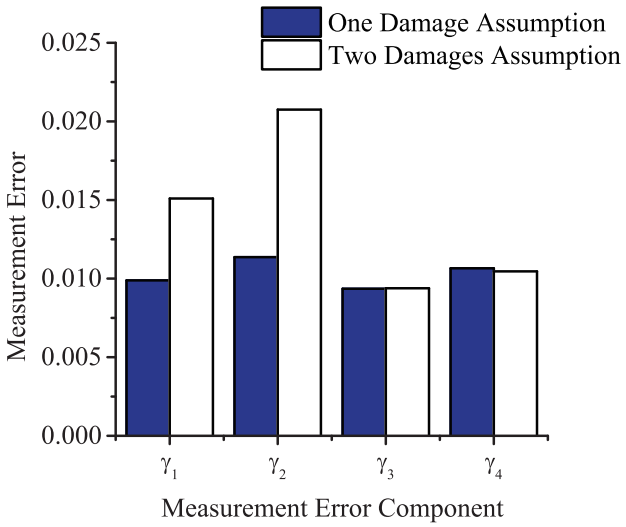

Figure 2.5: Measurement error for the four objectives for the "best" individual in the Pareto front damage region solution estimates obtained from multi-objective optimization with the assumption of one damage region (One Damage Assumption) and with the assumption of two damage regions (Two Damages Assumption) for the representative results for the simulated example square plate structure with a single damage region.

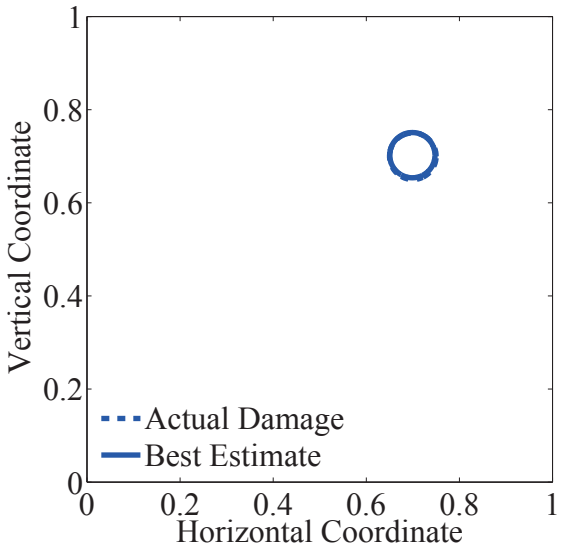

Figure 2.6: Final ("best") solution estimate obtained from multi-objective optimization with the assumption of one damage region compared to the actual (experimental) single damage region for the simulated example square plate structure.

2.5.1.2 Two and Three Damage Regions Two additional cases were considered for the simulated square plate example to further test the capabilities of the NDE algorithm with self-evolving parameterization, a case with two actual damage regions in the simulated experiment and a case with three actual damage regions in the simulated experiment. Tables 2.2 and 2.3 show the actual values for the unknown damage parameters (i.e., the parameter values used to simulate the experimental measurements) for the two damage and three damage cases, respectively, noting that the minimum and maximum values (i.e., constraints) for each individual parameter were identical to those used previously for the one damage case (as shown in Table 2.1).

Fig. 2.7 shows a representative example from the five trials of the inverse solution process of the Pareto front solution estimates and Fig. 2.8 shows the corresponding measurement error for the four objectives for the "best" individual from each of the Pareto fronts at each solution iteration (as the parameterization evolved), and Fig. 2.9 shows the final solution estimate from the converged algorithm for the example with two actual damage regions.

Table 2.2: Actual (experimental) values for the unknown damage centroid horizontal and vertical coordinates (c_h and c_v) and radius (c_r) for each damage region for the example square plate structure with two damage locations.

Damage Parameter	Region 1	Region 2
c_h	0.5	0.8
c_v	0.5	0.8
c_r	0.05	0.025

Table 2.3: Actual (experimental) values for the unknown damage centroid horizontal and vertical coordinates (c_h and c_v) and radius (c_r) for each damage region for the example square plate structure with three damage locations.

Damage Parameter	Region 1	Region 2	Region 3
c_h	0.2	0.8	0.8
c_v	0.5	0.8	0.2
c_r	0.075	0.075	0.05

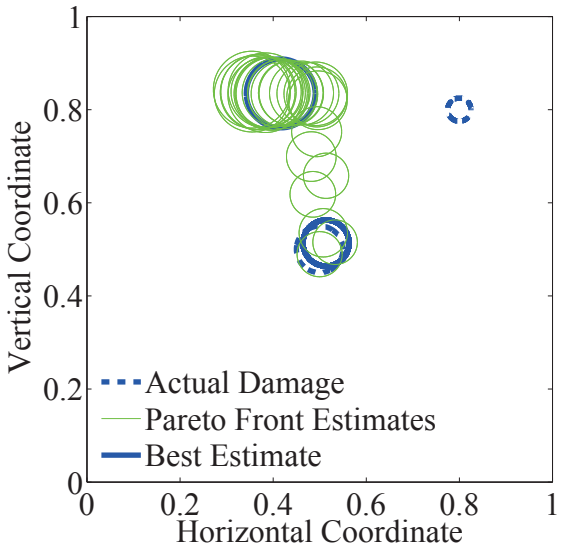

(a)

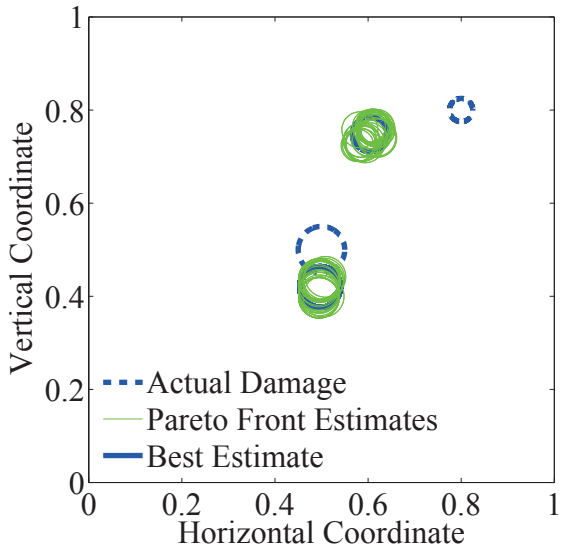

(b)

Figure 2.7: Representative results of the Pareto front damage region solution estimates obtained from the NDE algorithm with self-evolving parameterization after (a) the first iteration with a single damage region parameterization and (b) the second iteration for which the parameterization had been automatically updated to two damage regions, along with the best individual from each Pareto front, and compared to the actual (experimental) two damage regions for the simulated example square plate structure.

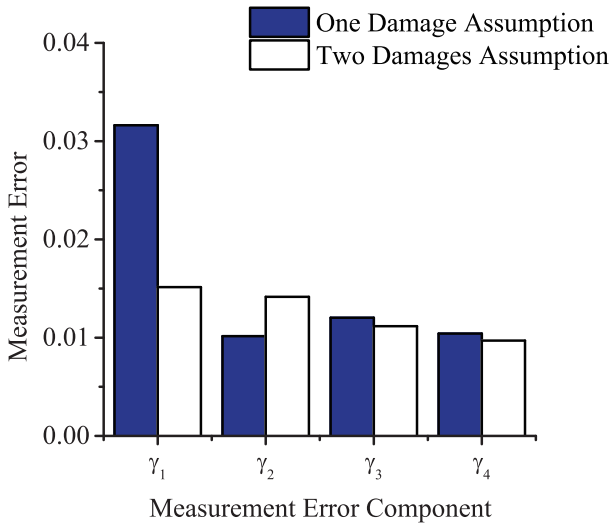

Figure 2.8: Measurement error for the four objectives for the (best) individual in the Pareto front damage region solution estimates obtained from the NDE algorithm with self-evolving parameterization after the first iteration with a single damage region parameterization (One Damage Assumption) and the second iteration for which the parameterization had been automatically updated to two damage regions (Two Damages Assumption) for the representative results for the simulated example square plate structure with two damage regions.

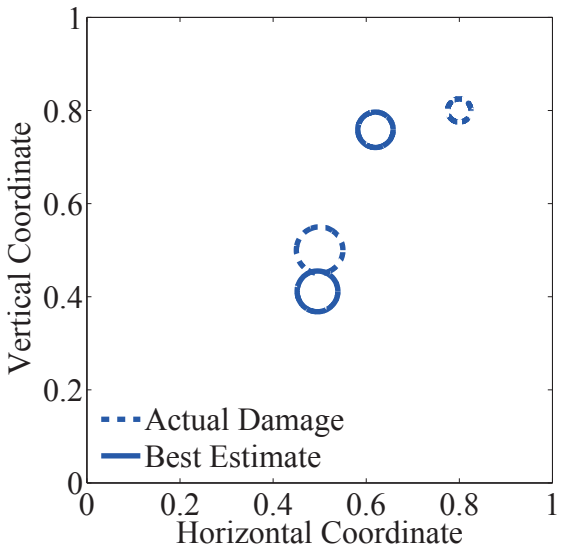

Figure 2.9: Final (best) solution estimate obtained from the NDE algorithm with self-evolving parameterization compared to the actual (experimental) two damage regions for the simulated example square plate structure.

In addition, Fig. 2.10 shows a representative example of the Pareto front solution estimates and Fig. 2.11 shows the corresponding measurement error for the four objectives for the "best" individual from each of the Pareto fronts at each solution iteration, and Fig. 2.12 shows the final solution estimate from the converged algorithm for the example with three actual damage regions.

Both of the trials shown converged after only two iterations, with the measurement error being substantially reduced after each iteration and the clustering results of the first iteration (Figs. 14(a) and 10(a)) leading to an evolution of the parameterization to the correct number of damage regions, even for the three damage case. All trials for the two damage case similarly converged after two iterations, however, a portion of the trials for the three damage case required three iterations to converge. For some trials of the three damage case (not shown for brevity) the first iteration lead to an expansion of the parameterization to two damage regions, the second iteration lead to an expansion of the parameterization to

three damage regions, and finally convergence at three damage regions. The final solution estimates for all trials of both test cases were similarly accurate as the examples shown, with both the sizes and locations of the damage regions being relatively accurate, but noticeably less accurate than the first example with a single actual damage region. This reduction in accuracy is not unexpected, however, with the difficultly of the inverse problems increasing substantially with the increase in the number of damage regions (i.e., increase in problem complexity). Yet, the consistent identification of the exact number of damaged regions with approximate sizes and locations is a significant accomplishment. One final note is that the NDE process is sensitive to the (relative) size of the disturbances to be characterized, and the process is progressively more likely to fail in identifying a damage region for the examples discussed herein as that damage region becomes smaller. However, this sensitivity of the solution capabilities to the magnitude of the change in the property to be determined is a fundamental challenge to any NDT/NDE method, regardless of the solution algorithm employed.

2.5.1.3 Robustness to Measurement Noise To examine the potential affects of additional errors/noise in the measurement data on the NDE algorithm with self-evolving parameterization, two additional higher noise levels of approximately 30 dB (i.e., $k = 0.03$) and 25 dB (i.e., $k = 0.06$) SNR were considered for the example with two actual damage regions in the simulated experiment (using the same damage parameters as were defined for Section 2.5.1.2). Fig. 2.13 and 2.14 show representative examples from the five trials of the inverse solution process of the Pareto front solution estimates corresponding to the measurement data with 30 dB and 25 dB SNR, respectively. In addition, Fig. 2.15 and 2.16 show the corresponding measurement error for the four objectives for the "best" individual from each of the Pareto fronts at each solution iteration (as the parameterization evolved) with the two levels of measurement error. Even with the substantial increase in the level of Gaussian white noise, both cases were able to converge after only two iterations and the measurement errors were able to be minimized to relatively low levels. However, after the first iteration the Pareto front solution distributions were noticeably more diverse (i.e., spread throughout the potential solution space) as the level of noise increased. In addition, the overall accuracy

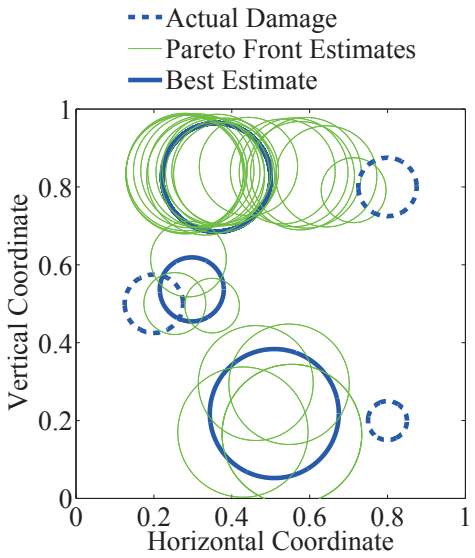

(a)

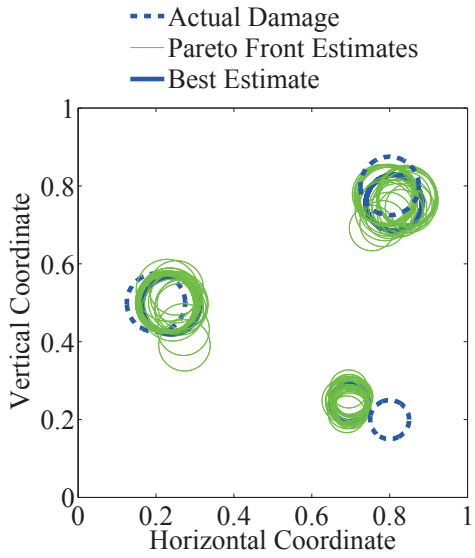

(b)

Figure 2.10: Representative results of the Pareto front damage region solution estimates obtained from the NDE algorithm with self-evolving parameterization after (a) the first iteration with a single damage region parameterization and (b) the second iteration for which the parameterization had been automatically updated to three damage regions, along with the best individual from each Pareto front, and compared to the actual (experimental) three damage regions for the simulated example square plate structure.

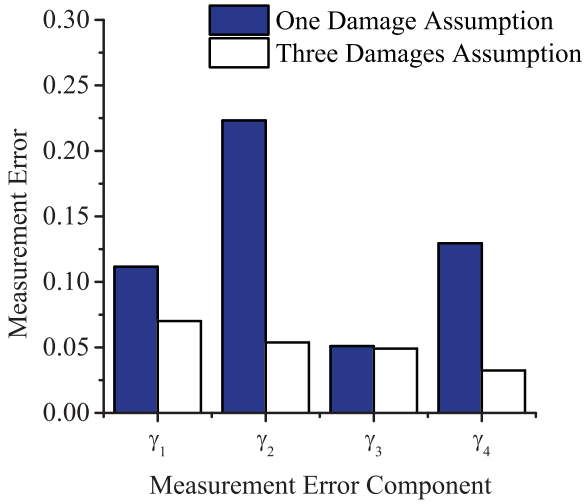

Figure 2.11: Measurement error for the four objectives for the (best) individual in the Pareto front damage region solution estimates obtained from the NDE algorithm with self-evolving parameterization after the first iteration with a single damage region parameterization (One Damage Assumption) and the second iteration for which the parameterization had been automatically updated to three damage regions (Three Damages Assumption) for the representative results for the simulated example square plate structure with three damage regions.

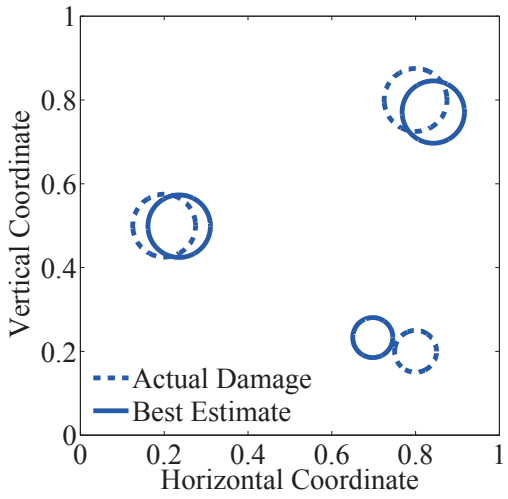

Figure 2.12: Final (best) solution estimate obtained from the NDE algorithm with self-evolving parameterization compared to the actual (experimental) three damage regions for the simulated example square plate structure.

of the solution estimate degraded to some degree with the increase in noise, which is to be expected. Overall, the NDE algorithm with self-evolving parameterization was found to be relatively robust to potential noise in the measurement data.

2.5.2 Example 2: Simulated Trapezoidal Plate

The final set of tests were intended to somewhat examine the generalization of the NDE algorithm with self-evolving parameterization by considering a more irregularly shaped structure. Thus, as shown in Fig. 2.17, an arbitrarily selected trapezoidal steel plate was analyzed to again determine the size and location of a number of damages throughout the plate.

As before, the plate was taken to be arbitrarily thin, the left side fixed to a rigid support, and the simulated NDT consisted of applying a 1 kN/m (factoring out the arbitrary thickness) harmonic excitation to the right (angled) surface of the plate and measuring the vertical and horizontal displacements at 1 cm increments along the top and bottom surfaces, as indicated in Fig. 2.17. The four objective functions for the multi-objective optimization

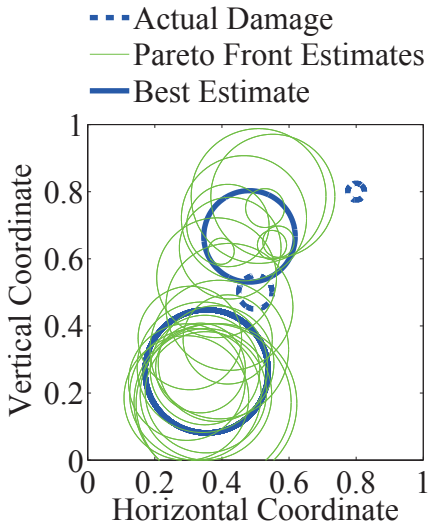

(a)

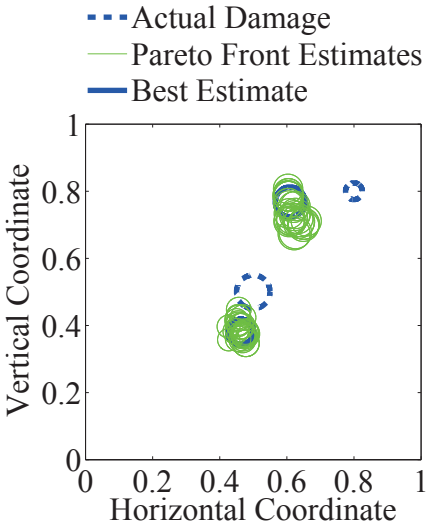

(b)

Figure 2.13: Representative results of the Pareto front damage region solution estimates obtained from the NDE algorithm with self-evolving parameterization after (a) the first iteration with a single damage region parameterization and (b) the second iteration for which the parameterization had been automatically updated to two damage regions, along with the best individual from each Pareto front, and compared to the actual (experimental) two damage regions for the simulated example square plate structure with 30 dB measurement SNR.

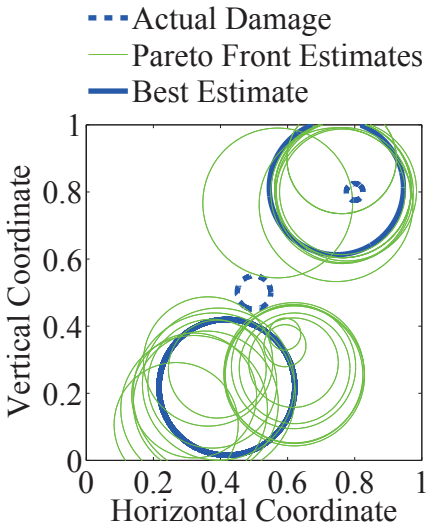

(a)

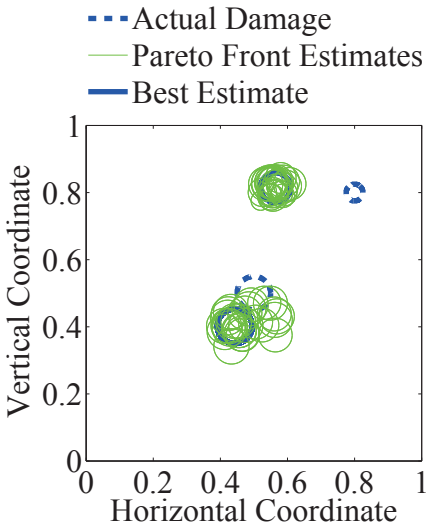

(b)

Figure 2.14: Representative results of the Pareto front damage region solution estimates obtained from the NDE algorithm with self-evolving parameterization after (a) the first iteration with a single damage region parameterization and (b) the second iteration for which the parameterization had been automatically updated to two damage regions, along with the best individual from each Pareto front, and compared to the actual (experimental) two damage regions for the simulated example square plate structure with 25 dB measurement SNR.

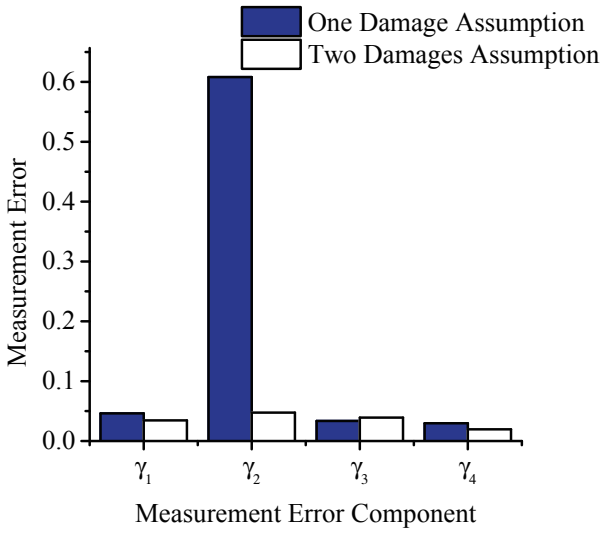

Figure 2.15: Measurement error for the four objectives for the (best) individual in the Pareto front damage region solution estimates obtained from the NDE algorithm with self-evolving parameterization after the first iteration with a single damage region parameterization (One Damage Assumption) and the second iteration for which the parameterization had been automatically updated to two damage regions (Two Damages Assumption) for the representative results for the simulated example square plate structure with two damage regions with 30 dB measurement SNR.

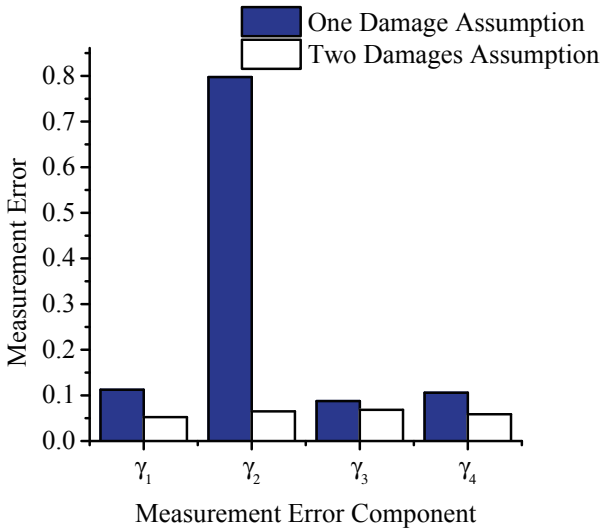

Figure 2.16: Measurement error for the four objectives for the (best) individual in the Pareto front damage region solution estimates obtained from the NDE algorithm with self-evolving parameterization after the first iteration with a single damage region parameterization (One Damage Assumption) and the second iteration for which the parameterization had been automatically updated to two damage regions (Two Damages Assumption) for the representative results for the simulated example square plate structure with two damage regions with 25 dB measurement SNR.

Table 2.4: Actual (experimental) values for the unknown damage centroid horizontal and vertical coordinates (c_h and c_v) and radius (c_r) for each damage region for the example trapezoidal plate structure with three damage locations.

Damage Parameter	Region 1	Region 2	Region 3
c_h	0.3	0.3	0.5
c_v	0.8	0.2	0.5
c_r	0.05	0.05	0.075

were defined by dividing the measurements with respect to the top and bottom and the two directional components.

A single three damage case was analyzed and Table 2.4 shows the actual values for the unknown damage parameters used to simulate the experimental measurements. The constraints for the parameters for the inverse solution process were such that the damage centers were within the plate domain and the damage radii were between 0 m and 0.5 m. Fig. 2.18 shows a representative example from the five trials of the inverse solution process of the Pareto front solution estimates at each iteration of the adaptive algorithm, and Fig. 2.19 shows the final solution estimate from the converged algorithm for the trapezoidal plate example.

Similarly to the previous two and three damage cases for the square plate, the majority of the trials for this case converged after two iterations (as shown), with a minority requiring three iterations, while all trials consistently determined the actual number of three damage regions. In addition, there was again an observable reduction in accuracy in the estimation of the damage locations and sizes for this relatively more challenging example case. Yet, the ability of the adaptive inverse solution process to consistently and efficiently determine the exact number of damage regions and provide relatively accurate estimations of the location and size of these damages based solely on surface measurements is significant.

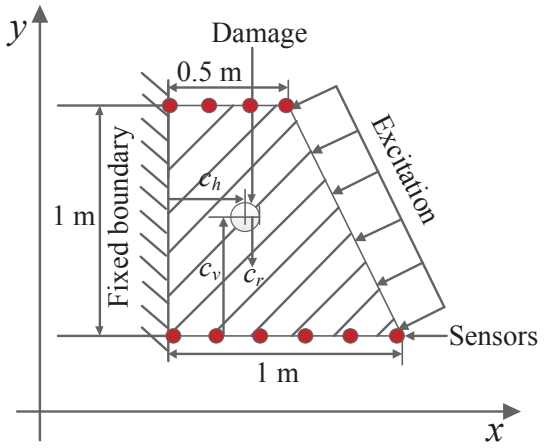

Figure 2.17: Schematic of the damaged trapezoidal plate structure for Example 2.

2.6 CONCLUSIONS

An approach for nondestructive evaluation for material characterization of solid continua incorporating a self-evolving parameterization strategy within a multi-objective optimization framework was presented. In general, the adaptive procedure shown utilizes the substantial solution diversity that is uniquely provided by multi-objective optimization to iteratively adapt the parameterization of the unknown field of the inverse problem to improve both computational efficiency and solution accuracy. More specifically, the presentation was focused on problems relating to characterization of an unknown quantity of localized changes in properties, such as those potentially caused by damage or degradation. In this context and starting from the minimum physically-relevant parameterization (e.g., parameterization of one damage location), the iterative solution process was shown to be capable of utilizing an *ad hoc* hierarchical clustering algorithm applied to the Pareto front results of a multi-objective optimization procedure to sequentially build up the parameterization (e.g., add potential damage regions to the parameterization) to provide an accurate inverse solution approximation with the minimum dimensional parameterization. The capabilities of the adaptive inverse characterization approach were displayed through a a series of tests of two simulated damage characterization problems based on vibration testing using direct

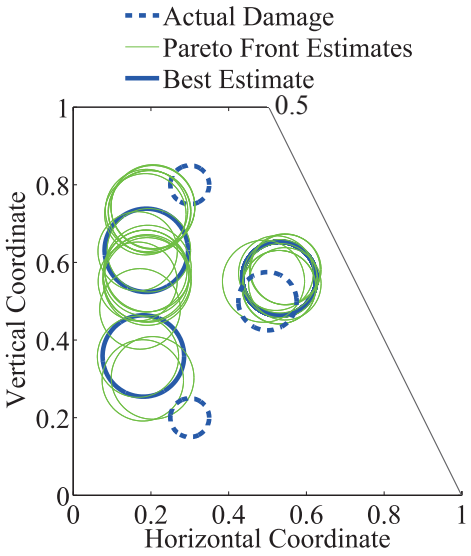

(a)

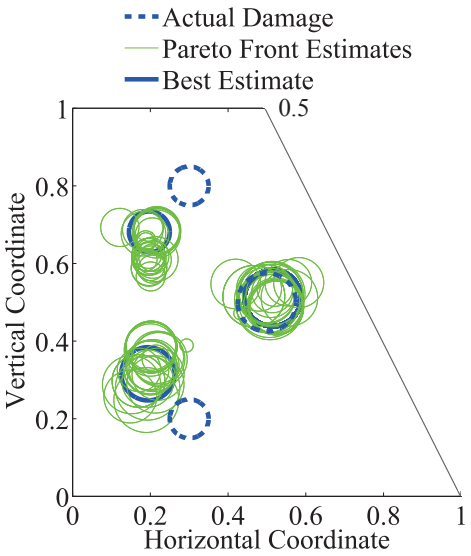

(b)

Figure 2.18: Representative results of the Pareto front damage region solution estimates obtained from the NDE algorithm with self-evolving parameterization after (a) the first iteration with a single damage region parameterization and (b) the second iteration for which the parameterization had been automatically updated to three damage regions, along with the best individual from each Pareto front, and compared to the actual (experimental) three damage regions for the simulated example trapezoidal plate structure.

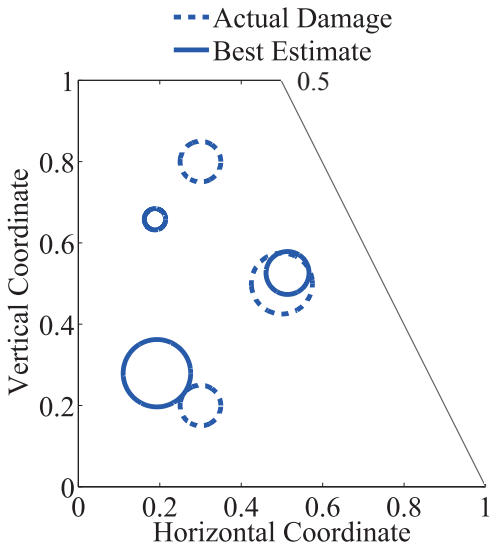

Figure 2.19: Final (best) solution estimate obtained from the NDE algorithm with self-evolving parameterization compared to the actual (experimental) three damage regions for the simulated example trapezoidal plate structure.

frequency response displacement measurements. Through the simulated test problems based on the characterization of material loss within structural steel plates, the adaptive inverse characterization approach was shown in all cases to efficiently determine the exact minimum parameterization necessary to capture the material loss while also providing sufficiently accurate approximations of the size and locations for multiple regions of material loss utilizing only surface response measurements and without any *a priori* knowledge of the number of damage regions.

3.0 A COMPUTATIONALLY EFFICIENT APPROACH FOR INVERSE MATERIAL CHARACTERIZATION COMBINING GAPPY POD WITH DIRECT INVERSION

3.1 ABSTRACT

An approach for computationally efficient inverse material characterization from partial-field response measurements that combines the Gappy proper orthogonal decomposition (POD) machine learning technique with a physics-based direct inversion strategy is presented and evaluated. Gappy POD is used to derive a data reconstruction tool from a set of potential system response fields that are generated from available *a priori* information regarding the potential distribution of the unknown material properties. Then, the Gappy POD technique is applied to reconstruct the full spatial distribution of the system response from whatever portion of the response field has been measured with the chosen system testing method. Lastly, a direct inversion strategy is presented that is derived from the equations governing the system response (i.e., physics of the system), which utilizes the full-field response reconstructed by Gappy POD to produce an estimate of the spatial distribution of the unknown material properties. The direct inversion technique is a particularly computationally efficient inversion technique, requiring a cost equivalent to a single numerical analysis. Therefore, the majority of the computational expense of the presented approach is the one-time potential response generation for the Gappy POD technique, which leads to an approach that is substantially computationally efficient overall. Two numerically simulated examples are shown in which the elastic modulus distribution was characterized based on partial-field displacement response measurements, both static and dynamic. The inversion procedure was shown to have the capability to efficiently provide accurate estimates to material property

distributions from partial-field response measurements. The direct inversion with Gappy POD response estimation was also shown to be substantially tolerant to noise in comparison to the direct inversion given measured full-field response. Lastly, a physical example regarding elastography of an arterial construct from ultrasound imaging response measurements is shown to validate the practical applicability of the direct inversion approach with Gappy POD response reconstruction.

3.2 INTRODUCTION

Inverse problems relating to the characterization of various material properties of a variety of solids/structures and systems are of paramount importance in a wide range of science and engineering fields. For instance, structures, from industrial to biological, could be evaluated to determine their current state of health based upon their material properties, whether mechanical, thermal, or electrical. Corresponding to this substantial interest in material property characterization, a wide variety of inverse problem solution strategies have been developed relating to a variety of applications, such as structural health monitoring and nondestructive evaluation [32, 71] and biomechanical imaging [8, 10, 5, 48, 22], among other applications [63, 26].

Since it is often not possible to find analytical solutions for inverse problems in practice, due to problem ill-posedness and/or complexities in geometry and boundary conditions, among other challenges, computational inverse characterization solution approximation approaches have become common. Overall, computational inverse characterization approaches, which are typically based around some type of computational representation of the mechanics of the system of interest (e.g., finite element analysis), have been shown through several studies [26, 5, 8] to provide generalized frameworks for treating and distinguishing between various contributions to a system response, while providing physically meaningful solutions that can be applied to predict future behaviors. However, there is as wide a variety of computational inverse problem approaches as there are applications, with each having different strengths and weaknesses, and their effectiveness is significantly dependent upon the specifics

of the application of interest. Moreover, the different computational approaches often differ significantly in the tradeoff between computational efficiency and solution accuracy.

One general way that computational inverse problem solution approaches can be divided is into those that use iterative optimization and those that are non-iterative/direct. Typically, the optimization-based approaches attempt to determine the unknown properties that minimize the difference between the measured system response and the response predicted by the computational representation of the mechanics of the system [71, 4, 23]. The optimization approaches can be divided further into those that use gradient-based optimization (e.g., Newton's method, conjugate gradient, etc.) and those that use non-gradient-based optimization (e.g., random search, genetic algorithm, etc.) to minimize the response error. Gradient-based optimization methods typically require substantially less iterations to converge to a solution approximation in comparison to non-gradient-based methods (i.e., are less computationally expensive), but often become trapped in local minima (i.e., an inaccurate solution), while non-gradient-based (since they commonly include some stochastic component) often have closer to global search capabilities. Alternatively, non-iterative methods attempt to somehow directly relate the measured response to the unknown parameters [81, 51]. As such, once set up, non-iterative methods are naturally almost negligible in computing cost in comparison to the optimization-based approaches.

Non-iterative methods include machine learning approaches that use experimentally and/or numerically generated datasets of potential inverse problems solution parameters and the corresponding system responses to train a "surrogate" mapping (e.g., artificial neural network) to approximate the relationship between the system response (as inputs to the mapping) and inverse unknowns (as outputs of the mapping) [77, 38]. Then, provided with a measured system response, the surrogate mapping can estimate inverse solution parameters in fractions of a second. Although relatively simple to implement, these machine learning approaches completely exclude any knowledge of the mechanics of the system beyond what can be naturally discerned from the dataset, and can have significant problems creating the surrogate mapping at all, since the input-output relationship is often not one-to-one, leading to substantial accuracy concerns in many cases. Alternatively, there are several different approaches (referred to as "direct inversion" methods herein) that instead manipulate the

equations governing the mechanics of the system (i.e., the forward boundary value problem) to create a solution process similar to that of solving the forward problem itself (e.g., similar in process to a finite element analysis to predict the deformation response of a solid given geometry, material properties, and boundary conditions). Therefore, the direct inversion methods provide a solution estimate based upon the measured response and the mechanics assumed to govern the response of the system considered at a cost on the order of a single numerical analysis of the forward problem.

Direct inversion approaches have seen considerable application in problems relating to characterization of the distribution of elastic properties from mechanical testing. Furthermore, these approaches include those that solve for the material properties over the entire (or almost the entire) domain at once (i.e., global methods), as well as those that break the domain into subregions and determine the properties for each subdomain in sequence (i.e., local). Global methods typically use some variation of either the finite difference method (FDM) or the finite element method (FEM) to create a system of equations based on the forward boundary value problem to solve the node or element-based elastic modulus distribution everywhere in the domain. FDM approaches for global direct inversion include the seminal work of Raghavan and Yagle [57] for simultaneously characterizing stiffness and hydrostatic pressure distribution of tissue from strain measurements, as well as other subsequent similar approaches for characterization of relative elastic modulus [65] and relative shear modulus [66] distributions. FEM approaches have shown some benefits over FDM approaches for global direct inversion in that they can be cast in a way so as to only require the gradient of displacement (i.e., a single derivative) rather than the divergence of strain (i.e., two derivatives of displacement). In this way, FEM approaches can be more tolerant to noise and other measurement errors than FDM approaches. Examples of FEM approaches for global direct inversion include the work by Zhu et al. [81] for elasticity reconstruction from displacement measurements and the work by Park and Maniatty [51] for shear modulus reconstruction from measured steady-state dynamic displacement fields. The local methods are often similar to the global methods, with several approaches similarly using principles from FDM and FEM (although not all), with the fundamental difference being just how the system is discretized/solved. Oliphant et al.[49, 50] presented a local approach that used

polynomial fit of the measured dynamic displacement field and the strong form of the governing equation of motion to characterize the elasticity distribution in tissues, while Romano et al. [61, 60] used a weak form FEM-type approach for element-by-element characterization of the ratio between both Lamé constants and density from dynamic displacement measurements. One particularly unifying aspect of the direct inversion approaches is that the entire (or nearly entire) spatial distribution (i.e., full-field) of the system response (e.g., displacement) must be measured/available to successfully characterize the unknown properties. Due to this requirement, the use of direct inversion (particularly of mechanical properties) has been mainly limited to biomechanical imaging applications (e.g., characterization of elastic properties of tissues from medical imaging data), where full-field or nearly full-field deformation information is regularly available. An additional common challenge of direct inversion approaches is their noise sensitivity. Most direct inversion approaches are not capable of producing a useable solution estimate with any significant level of measurement noise, which has resulted in several investigations into strategies for signal denoising prior to applying direct inversion [51, 50].

This work presents an approach to utilize measurement data from only a portion of the system domain (i.e., partial-field data) for direct inversion of material properties. In particular, the approach is presented in the context of characterizing the spatial distribution of the elastic modulus of solids (i.e., elastography) provided with displacement response measurements over some portion of the solid domain. The core component of this approach is the use of the Gappy proper orthogonal decomposition (POD) machine learning strategy to build a data reconstruction tool that can predict the full-field response of a system from the available partial-field measurements. This data reconstruction tool is built from a set of potential solution fields that are generated based upon information known *a priori* about the nature of the potential inverse problem solutions (e.g., arbitrarily generated approximate potential elastic modulus distributions). Once the full-field response reconstruction is complete, the full-field response is applied in a finite element-type direct inversion strategy to estimate the unknown material property distribution everywhere in the domain at a computational expense approximately equivalent to a single finite element analysis of the system. In addition, the Gappy POD approach can also act as somewhat of a noise filter

during the reconstruction process, thereby, providing an added benefit of reducing the effects of measurement noise on the subsequent direct inversion solution procedure.

The following section presents the details of the Gappy POD approach to reconstruct full-field data from partial-field measurements. Then, Section 3.4 shows the direct inversion algorithm to calculate the spatial distribution of elastic modulus provided with the full-field displacement response and the boundary conditions corresponding to the test method used to produce the measurements (i.e., the constraints on the solid and the excitation used to generate the displacement measurements). The complete direct inversion with Gappy POD algorithm is summarized in Section 3.5. Section 3.6 presents two simulated case studies relating to characterization of localized elastic modulus distributions in solids to evaluate the capabilities of the inverse characterization procedure, which are followed by an example utilizing (actual) experimentally obtained displacement measurements to evaluate the stiffness distribution of an arterial construct to validate the "real-life" applicability of the approach.

3.3 GAPPY PROPER ORTHOGONAL DECOMPOSITION

Gappy POD is an extension of the traditional POD approach that was first developed and presented by Everson and Sirovich [19] for the purpose of filling in missing information to reconstruct marred photos. Subsequently, Gappy POD has shown substantial capabilities to accurately reconstruct physical processes from partial-field measurement data, especially for fluid flow problems [69, 67, 74, 78, 64], and has even been investigated for use in creating surrogate mappings (as described in Section 3.2) to solve design-type inverse problems [67].

To discuss the Gappy POD process, it is first necessary to outline the standard POD method. Given a set of n fields (referred to as "snapshots"), $\{\vec{u}_k(\vec{x})\}_{k=1}^{n}$, POD can be interpreted as an approach to determine the set of m orthogonal basis functions (i.e., modes), $\left\{\vec{\phi}_i(\vec{x})\right\}_{i=1}^{m}$, that are optimal in some sense for representing each given field and, if the given fields are representative, any similar field as:

$$\vec{u}(\vec{x}) \approx \vec{u}^{*}(\vec{x}) = \sum_{i=1}^{m} a_i \vec{\phi}_i(\vec{x}), \tag{3.1}$$

where $\vec{x}$ is the spatial position vector and a_i is the modal coefficient corresponding to the i^{the} mode ($\vec{\phi}_i(\vec{x})$). More specifically, POD identifies the modes that minimize the average L_2-error between the given snapshots and the best approximation of the snapshots from the modes (i.e., the projection of each snapshot onto the modes) as:

$$\underset{\left\{\vec{\phi}_i(\vec{x})\right\}_{i=1}^{m}}{Minimize} \left\langle \|\vec{u}(\vec{x}) - \vec{u}^*(\vec{x})\|^2_{L_2(\Omega)} \right\rangle, \tag{3.2}$$

where $\langle \vec{u} \rangle = \frac{1}{n}\sum_{k=1}^{n} \vec{u}_k$. Based on this optimization problem and applying the method of snapshots (see [2] for additional details), a maximum of n POD modes can be calculated through the solution of the following eigenvalue problem:

$$\frac{1}{n}\sum_{k=1}^{n} A_{jk}C_k = \lambda C_j, \tag{3.3}$$

where

$$A_{jk} = \int_{\Omega} \vec{u}_j\left(\vec{\xi}\right) \cdot \vec{u}_k\left(\vec{\xi}\right) d\vec{\xi}, \tag{3.4}$$

and then the i^{th} mode is given as:

$$\vec{\phi}_i\left(\vec{x}\right) = \frac{1}{\lambda^{(i)} n}\sum_{k=1}^{n} \vec{u}_k\left(\vec{x}\right) C_k^{(i)}. \tag{3.5}$$

An important point is that only a portion ($m << n$) of the set of modes that can be obtained is typically necessary to be retained for further use, whether it be for data representation for pattern recognition purposes [76], reduced-basis model reduction [2], or otherwise. As the associated eigenvalues from the solution of Eqn. (3.3) relate to the value of each mode for the representation of the given dataset, a common heuristic is to retain the number of modes such that the sum of the associated eigenvalues is some amount greater than 99% of the sum of all n eigenvalues.

The Gappy POD process starts by following the above described standard POD procedure to obtain a set of orthogonal modes from a given set of snapshots. The point in which Gappy POD diverges from standard POD is how those modes are utilized. If the full distribution (specifically, full spatial distribution for the cases herein) of a field is available, the

modal coefficients (a_i) needed to reconstruct that field with the POD modes can be easily obtained by projecting the modes onto the field as:

$$a_i = \int_\Omega \vec{u}\left(\vec{\xi}\right) \cdot \vec{\phi}_i\left(\vec{\xi}\right) d\vec{\xi}. \tag{3.6}$$

However, projection is no longer applicable to determine the values of the modal coefficients to reconstruct the field if the entire spatial distribution is not available. Thus, the objective of Gappy POD is to provide a means to reconstruct the full spatial distribution of a field using the POD modes, but with only a partial spatial distribution of the field given. Defining $\hat{\vec{u}}(\vec{x})$ as the given partial distribution of the field of interest such that $\hat{\vec{u}}(\vec{x})$ is (incorrectly) 0 anywhere data is unavailable, then $\hat{\vec{u}}(\vec{x})$ can be expressed in terms of the corresponding, but unknown, full spatial distribution as:

$$\hat{\vec{u}}(\vec{x}) = \beta(\vec{x}, \vec{u})\, \vec{u}(\vec{x}), \tag{3.7}$$

where $\beta(\vec{x}, \vec{u})$ is a mask function that is defined as 0 where data is unavailable and 1 where data is available. Assuming that the full spatial distribution can be approximated with the POD modes as defined in Eqn. (3.1), an approximation of $\hat{\vec{u}}(\vec{x})$ can be written in terms of the POD modes as:

$$\hat{\vec{u}}^*(\vec{x}) = \beta(\vec{x}, \vec{u}) \sum_{i=1}^{m} a_i \vec{\phi}_i(\vec{x}). \tag{3.8}$$

Then, based upon a least-squares criteria, the optimal set of modal coefficients to reconstruct the full spatial distribution of the field can be defined as that which minimizes an error function of the form:

$$\varepsilon = \int_\Omega \left[\beta(\vec{x}, \vec{u})\, \vec{u}(\vec{x}) - \beta(\vec{x}, \vec{u}) \sum_{i=1}^{m} a_i \vec{\phi}_i(\vec{x})\right]^2 d\vec{x}. \tag{3.9}$$

Lastly, applying the necessary condition for extrema of a function by setting the derivative of the error function with respect to the modal coefficients to zero, the optimal set of modal coefficients, {a}, to reconstruct the full spatial distribution of the field can be determined from the solution of:

$$[M]\{a\} = \{f\}, \tag{3.10}$$

where

$$M_{ij} = \int_{\Omega} \beta\left(\vec{x}, \vec{u}\right) \vec{\phi}_i(\vec{x}) \cdot \vec{\phi}_j(\vec{x}) \; d\vec{x}. \tag{3.11}$$

and

$$f_i = \int_{\Omega} \beta\left(\vec{x}, \vec{u}\right) \vec{u}(\vec{x}) \cdot \vec{\phi}_i(\vec{x}) \; d\vec{x}. \tag{3.12}$$

3.4 DIRECT INVERSION OF ELASTIC MODULUS

As discussed, although potentially applicable to a variety of different physical systems, the application of the present work is characterization of the elastic modulus distribution of a solid from displacement measurements (full-field displacement response once Gappy POD has been utilized). Furthermore, the following formulation is presented with respect to a steady-state dynamic testing procedure (as could be applicable to frequency response function-based evaluation), but could easily be converted to a static problem by simply setting the excitation frequency to zero. To provide a foundation for the formulation, the following presents the standard forward problem (i.e., finite element formulation), as would be used to calculate the steady-state harmonic displacement response of the solid given material properties and boundary conditions (also, note that this forward problem was used to generate the snapshots for the Gappy POD procedure), followed by the numerical direct inversion procedure (i.e. inverse problem) to approximate the elastic modulus distribution.

3.4.1 Forward Problem

Neglecting body forces and damping, assuming displacements and strains are small, and assuming that the system variables vary harmonically in time at angular excitation frequency ω, the steady-state dynamic governing equations describing the forward elasticity problem (i.e., the strong form) can be given as:

$$\nabla \cdot \boldsymbol{\sigma}(\vec{x}, \omega) + \omega^2 \rho(\vec{x}) \vec{u}(\vec{x}, \omega) = \vec{0} \;\; on \; \Omega, \tag{3.13}$$

$$\boldsymbol{\sigma}(\vec{x}, \omega) = \boldsymbol{C}^{IV}(\vec{x}) : \boldsymbol{\varepsilon}(\vec{x}, \omega), \tag{3.14}$$

$$\boldsymbol{\varepsilon}(\vec{x},\omega) = \frac{1}{2}\left(\nabla\vec{u}(\vec{x},\omega) + (\nabla\vec{u}(\vec{x},\omega))^T\right), \tag{3.15}$$

$$\boldsymbol{\sigma}(\vec{x},\omega)\cdot\vec{n}(\vec{x}) = \vec{T}(\vec{x},\omega) \;\; on\ \Gamma_{\vec{T}}, \tag{3.16}$$

and

$$\vec{u}(\vec{x},\omega) = \vec{u}_0(\vec{x},\omega) \;\; on\ \Gamma_{\vec{u}}, \tag{3.17}$$

where $\rho(\vec{x})$ is the mass density, $\boldsymbol{\sigma}(\vec{x},\omega)$ is the Cauchy stress amplitude tensor, $\vec{u}(\vec{x},\omega)$ is the displacement amplitude vector, Ω is the domain of the structure, $\boldsymbol{\varepsilon}(\vec{x},\omega)$ is the small strain amplitude tensor, $\boldsymbol{C}^{IV}(\vec{x})$ is the 4^{th}-order elasticity tensor, $\vec{n}(\vec{x})$ is the unit outward normal vector to the surface of the domain, $\vec{T}(\vec{x},\omega)$ and $\Gamma_{\vec{T}}$ are the applied traction amplitude vector and the portion of the domain surface where this traction is applied, respectively, and $\vec{u}_0(\vec{x},\omega)$ and $\Gamma_{\vec{u}}$ are the applied displacement amplitude vector and the portion of the domain surface where displacement is known, respectively.

Applying standard procedures for the weak form finite element method [59], the weak form of this steady-state dynamic boundary value problem can be written as:

$$\int_\Omega \delta\boldsymbol{\varepsilon}(\vec{x}) : \boldsymbol{\sigma}(\vec{x},\omega)\ d\vec{x} - \int_\Omega \rho(\vec{x})\omega^2\delta\vec{u}(\vec{x})\cdot\vec{u}(\vec{x},\omega)\ d\vec{x} = \int_{\Gamma_{\vec{T}}} \delta\vec{u}(\vec{x})\cdot\vec{T}(\vec{x},\omega)\ d\vec{x}, \tag{3.18}$$

where $\delta\vec{u}(\vec{x})$ is the virtual displacement vector field (i.e., weight function or test function) and $\delta\boldsymbol{\varepsilon}(\vec{x})$ is the associated virtual strain tensor. Further applying the standard finite element procedure and converting to Voigt notation, the domain can be discretized into a collection of elements, and the displacement and virtual displacement fields and their corresponding strain vectors can be approximated as:

$$\vec{u}(\vec{x},\omega) \approx [N_{\vec{u}}(\vec{x})]\{\vec{u}^e(\omega)\}, \tag{3.19}$$

$$\delta\vec{u}(\vec{x}) \approx [N_{\vec{u}}(\vec{x})]\{\delta\vec{u}^e\}, \tag{3.20}$$

$$\{\varepsilon(\vec{x},\omega)\} \approx [B_{\vec{u}}(\vec{x})]\{\vec{u}^e(\omega)\}, \tag{3.21}$$

and

$$\{\delta\varepsilon(\vec{x})\} \approx [B_{\vec{u}}(\vec{x})]\{\delta\vec{u}^e\}, \tag{3.22}$$

where $[N_{\vec{u}}(\vec{x})]$ is the standard matrix of shape functions for displacement interpolation and $[B_{\vec{u}}(\vec{x})]$ is the matrix of shape function spatial derivatives for strain interpolation. Substituting these field approximations into Eqn. (3.18), eliminating the arbitrary virtual response field vector, and assembling individual element contributions, the final finite element equations are depicted as:

$$[K]\{u\} - [M]\{u\} = \{P\}, \tag{3.23}$$

where

$$[K] = \sum_{element} \int_{\Omega^e} [B_{\vec{u}}(\vec{x})]^T [D][B_{\vec{u}}(\vec{x})]\ d\vec{x}, \tag{3.24}$$

$$[M] = \sum_{element} \int_{\Omega^e} \rho(\vec{x})\omega^2 [N_{\vec{u}}(\vec{x})]^T [N_{\vec{u}}(\vec{x})]\ d\vec{x}, \tag{3.25}$$

$$\{P\} = \sum_{element} \int_{\Gamma^e_{\vec{T}}} [N_{\vec{u}}(\vec{x})]^T \vec{T}(\vec{x},\omega)\ d\vec{x}, \tag{3.26}$$

and $[D]$ is elasticity matrix, such that:

$$\{\sigma(\vec{x},\omega)\} = [D]\{\varepsilon(\vec{x},\omega)\} \tag{3.27}$$

The summation over elements refers to the assembly process.

3.4.2 Inverse Problem

With the objective of the inverse problem being characterization of the elastic modulus distribution provided with the entire displacement field everywhere in the domain, the first step in the inverse solution formulation is to separate the elastic modulus ($E(\vec{x})$) from the elasticity matrix as:

$$[D] = [D_I]E(\vec{x}), \tag{3.28}$$

where D_I is now only a function of Poisson's ratio (ν). Applying the same general weak form procedure as was done previously for displacement, but now for the elastic modulus,

the inverse problem weak form for the steady-state dynamic boundary value problem can be written as:

$$\int_{\Omega} \nabla \delta \vec{E}(\vec{x}) : \boldsymbol{\sigma}_I(\vec{x},\omega) E(\vec{x}) \; d\vec{x} = \int_{\Omega} \rho(\vec{x}) \omega^2 \delta \vec{E}(\vec{x}) \cdot \vec{u}(\vec{x},\omega) \; d\vec{x} + \int_{\Gamma_{\vec{T}}} \delta \vec{E}(\vec{x}) \cdot \vec{T}(\vec{x},\omega) \; d\vec{x}, \tag{3.29}$$

where

$$\{\sigma_I(\vec{x},\omega)\} = [D_I]\{\varepsilon(\vec{x},\omega)\}, \tag{3.30}$$

and $\delta\vec{E}$ is the virtual elastic modulus vector (matching the dimension of the displacement field, and therefore, the number of equilibrium equations, even though the modulus itself is a scalar). Now discretizing the domain into finite elements to represent the elastic modulus and again using Voigt notation where applicable, the elastic modulus and virtual elastic modulus vector and their corresponding gradients can be approximated as:

$$E(\vec{x}) \approx [N_E(\vec{x})]\{E^e\}, \tag{3.31}$$

$$\delta\vec{E}(\vec{x}) \approx [N_{\delta\vec{E}}(\vec{x})]\{\delta\vec{E}^e\}, \tag{3.32}$$

$$\{\nabla E(\vec{x})\} \approx [B_E(\vec{x})]\{E^e\}, \tag{3.33}$$

and

$$\{\nabla \delta\vec{E}(\vec{x})\} \approx [B_{\delta\vec{E}}(\vec{x})]\{\delta\vec{E}^e\}, \tag{3.34}$$

where $[N_E(\vec{x})]$ is now the matrix of shape functions for elastic modulus interpolation, $[N_{\delta\vec{E}}(\vec{x})]$ is the expanded version (to match the dimensions of the displacement) of the matrix of shape functions for elastic modulus interpolation, and $[B_E(\vec{x})]$ and $[B_{\delta\vec{E}}(\vec{x})]$ are the respective matrices of these shape function spatial derivatives. Substituting these field approximations as well as the previously-defined discretization of the given displacement field into Eqn. (3.29), eliminating the arbitrary virtual elastic modulus field vector, and assembling individual element contributions, the final finite element equations for the direct inversion elastography problem are depicted as:

$$[K_I]\{E\} = \{P_I\} + [M_I]\{u\}, \tag{3.35}$$

where

$$[K_I] = \sum_{element} \int_{\Omega^e} [B_{\delta\vec{E}}(\vec{x})]^T [D_I][B_{\vec{u}}(\vec{x})]\{\vec{u}^e\}[N_E(\vec{x})]\ d\vec{x}, \tag{3.36}$$

$$[M_I] = \sum_{element} \int_{\Omega^e} \rho(\vec{x})\omega^2 [N_{\delta\vec{E}}(\vec{x})]^T [N_{\vec{u}}(\vec{x})]\ d\vec{x}, \tag{3.37}$$

and

$$\{P_I\} = \sum_{element} \int_{\Gamma^e_{\vec{T}}} [N_{\delta\vec{E}}(\vec{x})]^T \vec{T}(\vec{x},\omega)\ d\vec{x}. \tag{3.38}$$

Since $[K_I]$ is typically non-square and Eqn. (3.35) is typically an overdetermined system ($[K_I]$ has dimensions $3N \times N$, where N is the number of nodes in the mesh if the same mesh is used for both fields), the elastic modulus cannot be estimated by simply inverting $[K_I]$. Thus, as is common, a least-squares approach was used here to solve Eqn. (3.35) for $\{E\}$. As such, the nodal values of elastic modulus can be determined as:

$$\{E\} = \left([K_I]^T[K_I]\right)^{-1} [K_I]^T \left(\{P_I\} + [M_I]\{u\}\right). \tag{3.39}$$

One final important point is that it is necessary to invalidate the equations corresponding to the essential boundary conditions (i.e., known displacement values) prior to the solution of Eqn. (3.39). Eliminating these equations is a common approach that is necessary to obtain a well-behaved solution to the direct inversion problem. Thus, prior to solving Eqn. (3.39) the rows in Eqn. (3.35) corresponding to nodes where essential boundary conditions are present are set to zero, such that:

$$[K_I][i,:] = 0, \quad \text{if} \quad \vec{x}_i \in \Gamma_{\vec{u}}, \tag{3.40}$$

$$[M_I]\{u\}[i] = 0, \quad \text{if} \quad \vec{x}_i \in \Gamma_{\vec{u}}, \tag{3.41}$$

and

$$\{P_I\}[i] = 0, \quad \text{if} \quad \vec{x}_i \in \Gamma_{\vec{u}}. \tag{3.42}$$

3.5 ALGORITHM FOR DIRECT INVERSION FROM PARTIAL-FIELD MEASUREMENTS WITH GAPPY POD

The overall algorithm for direct inversion of a material property distribution from partial-field response measurements with Gappy POD can be summarized as follows:

Given: The geometry of the structure of interest, the boundary conditions and partial-field response measurements from a nondestructive testing procedure, and any available material properties.

Find: The unknown material property distribution.

Step 1: Generate (e.g., randomly or through some other sampling procedure) a set of potential distributions for the unknown material property, using any information available *a priori* relating to the likely nature of the unknown distribution, and use a forward analysis procedure (e.g., Section 3.4.1) to produce the corresponding full-field structural responses for each property distribution from the nondestructive testing conditions.

Step 2: Calculate the POD modes from the set of full-field structural responses (Eqn. (3.5)), and select the modes (based on a user-defined criteria, such as the eigenvalue energy) to be retained for Gappy POD field reconstruction.

Step 3: Reconstruct the full-field structural response from the given partial-field measurements with Gappy POD (Eqs. (3.10) and (3.1)).

Step 4: Calculate an estimate to the unknown material property distribution using the direct inversion procedure (e.g., Section 3.4.2) with the reconstructed full-field structural response and nondestructive test boundary conditions.

An additional note is that the vast majority of the computational expense resides in Steps 1 and 2 (i.e., generating the POD modes),which is only necessary to be completed one time for a given problem (e.g., geometry, boundary conditions, parameterization, etc.). Then, the remaining Steps 3 and 4 can be repeated as many times as is desired based on these POD modes. Therefore, the same structure at different times in the structure's life or different, but similar structures could be evaluated to characterize their material property

distributions without having to create new snapshots (i.e., without having to evaluate the forward boundary value problem again), and therefore, with minimal computational expense.

3.6 EXAMPLES AND DISCUSSION

Three examples were considered and evaluated to examine the potential benefits and capabilities of using the direct inversion approach with Gappy POD to characterize the elastic modulus distribution in solids from partial-field measurements. In all three cases, the partial-field measurements were assumed to be obtained from some type of nondestructive testing in the linear range of the solid behavior. First, two numerical examples were considered in which the "experiment" was simulated through finite element analysis, as described in Section 3.4.1, then a physical (i.e., "real life") example was considered relating to elastography of an arterial construct [18].

For all three examples, the finite element method was used to generate the snapshots for the POD process. In addition, the criteria used to determine the number of modes (m) out of the total number available (n) to use for data reconstruction with Gappy POD was to select the mode with the highest associated eigenvalue (λ in Eqn. 3.3) as well as the minimum number of the remaining modes, such that:

$$\frac{\sum_{j=2}^{m} \lambda^{(j)}}{\sum_{i=2}^{n} \lambda^{(i)}} \times 100\% > 99.9\% \tag{3.43}$$

This criteria was determined to be sufficient to ensure that enough modes were retained from POD for Gappy POD to produce accurate reconstructions, while excluding the modes associated with low eigenvalues that can often cause the matrix $[M]$ in Eqn. 3.10 to be ill-conditioned.

3.6.1 Numerically Simulated Examples

The two numerically simulated experiments were based upon characterization of elastic modulus distributions with circular inclusions (hard or soft), as shown schematically in Fig. 3.1.

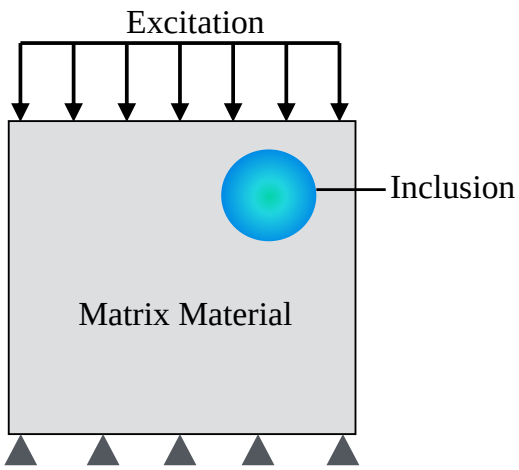

Figure 3.1: Schematic for the numerically simulated examples representing characterization of an elastic modulus distribution with an inclusion.

The circular inclusion assumption was used for simplicity, but more importantly, it is based on several other related characterization works for a variety of applications [20, 26, 37]. In addition, both examples used the plane stress assumption to reduce the computational expense. A Gaussian radial basis function (RBF) representation was chosen to define the localized elastic modulus variations, which was based upon several other similar works [14, 1, 13]. The RBF representation of elastic modulus distribution was defined as:

$$E(\vec{x}) = E_0 \left[1 + \sum_{i=1}^{N_I} \alpha_i exp\left(-\frac{(\vec{x} - \vec{c}_i)^2}{r_i^2} \right) \right], \tag{3.44}$$

where E_0 is the elastic modulus of the matrix material, α_i is the relative change in elastic modulus at the i^{th} inclusion center, $\vec{c}_i$, is the location of the i^{th} inclusion center, r_i is the breadth of the i^{th} inclusion, and N_I is the total number of inclusions. In addition, for the inverse characterization process, it was assumed to be known *a priori* that the variation in elastic modulus was similarly localized in nature (of course, with the size, amplitude, and location of this variation to be estimated by characterizing the entire spatial distribution of the elastic modulus with the direct inversion procedure). Therefore, the process to create the POD modes used snapshots generated with this same RBF parameterization of the elastic

modulus distribution. To add realism to the simulated experiments, for all trials Gaussian white noise was also added to the simulated measurements as:

$$u^{expn} = u^{exp}\left(1 + k\upsilon\right), \tag{3.45}$$

where u^{expn} and u^{exp} are the simulated experimental displacement measurements with noise and without noise, respectively, k is the noise amplitude multiplier, and υ is a normally distributed random variable with unit variance and zero mean.

3.6.1.1 Example 1: Simulated Soft Matrix with a Hard Inclusion - Static Test

The first example of a simulated soft matrix with a hard inclusion was intended to relate to potential applications of tissue characterization (e.g., tumor characterization) from (quasi-) static mechanical testing [22, 48]. A tissue block was modeled as a 50 $mm \times 50$ mm square domain with the bottom fixed to a rigid support. The entire material (matrix and inclusion) was assumed to be known to be nearly incompressible, and a Poisson's ratio of 0.49999 was assigned. The simulated static test was implemented by applying a 0.2 N/mm (factoring out the arbitrary thickness) excitation uniformly to the top surface of the tissue block. Then, the static vertical displacement response to the loading was measured at 100 uniformly spaced discrete locations, as shown in Fig. 3.2. 5% Gaussian white noise was added to the measurements for this first example, which was deemed to be reasonable level of noise that could be expected from similar tests (note that this level of noise is commensurate with the highest levels of noise used in prior referenced works on direct inversion strategies with full-field response measurements).

For the process of generating the snapshots for POD, the elastic modulus of the background material (i.e., matrix material) was assumed to be fixed at 15 kPa, which was based on normal glandular breast tissue [81, 51]. Alternatively, the parameters defining the inclusion based on the RBF description were assumed to be variable. The specific parameter values used to create the snapshots were chosen arbitrarily by uniformly sampling the space of the four variable parameters (the two spatial coordinates, amplitude, and breadth). Three values were chosen for each spatial coordinate of the inclusion center and two values were chosen each for the amplitude and breadth of the inclusion, and one last scenario with no

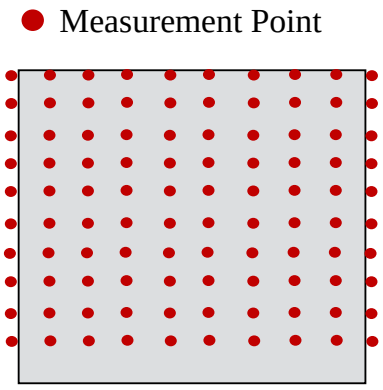

Figure 3.2: Schematic of the vertical displacement sensor locations (red dots) for Example 1: Simulated Soft Matrix with a Hard Inclusion.

inclusion (i.e., homogeneous matrix material) was added, for a total of 37 parameter combinations used to create snapshots. Fig. 3.3 shows the nine location combinations of the inclusion center used to generate the snapshots. The values of the other two parameters used to create the parameter combinations were chosen based on an expectation of what the lower and upper-end would be for the application, using 1 and 3 for the amplitude parameter α (i.e., modulus at inclusion center of 30 kPa and 60 kPa) and 5 mm and 15 mm for the breadth parameter r. To be clear, note that each of elastic modulus distribution realizations used to create a snapshot contained only one inclusion (other than the homogeneous case, which contained none). 15 out of the 37 total available POD modes were necessary to satisfy the criteria defined in Eqn. 3.43 and were retained for the Gappy POD reconstruction process.

A 50×50 mesh of quadratic triangular elements was determined to be sufficient for accurately analyzing the tissue deformation (i.e., solving the forward problem) for all possible material property distributions. For simplicity, this same mesh was used to discretize the elastic modulus distribution for the direct inversion procedure. However, to reduce the dimensionality slightly the elastic modulus was described with linear triangular elements rather than quadratic.

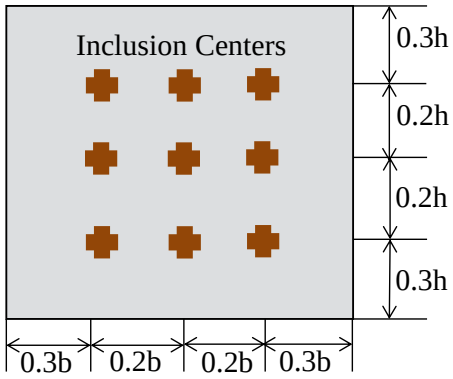

Figure 3.3: Schematic of the nine inclusion centers used separately to generate the snapshots for POD for the numerically simulated examples.

Results:

As an example of the appearance of the POD modes, Fig. 3.4 shows the distributions of the components of the first two POD modes (i.e., the modes corresponding to the two highest eigenvalues from the POD procedure). More importantly, Fig. 3.5 shows a representative example trial of a simulated displacement response field from a randomly generated parameter set and including the 5% Gaussian white noise in comparison to the displacement response field reconstructed from the 100 response measurements of that response field with the Gappy POD procedure. In general, the Gappy POD reconstruction of the displacement response from partial-field measurements was found to be accurate, producing response distributions that were nearly identical to the full simulated responses, with errors consistent with the example shown, which had relative L_2 and L_∞ errors in the displacement reconstruction of 7.4% and 18.5%, respectively.

Fig. 3.6 shows a representative example of an elastic modulus distribution used to generate simulated experimental measurements (i.e., target modulus distribution) and the corresponding elastic modulus distribution estimated by the direct inversion procedure with Gappy POD displacement reconstruction. There was a noticeable amount of error in the modulus reconstruction, and the relative L_2 and L_∞ errors in the modulus estimation compared to the target distribution were 21% and 43%, respectively. However, the localization of

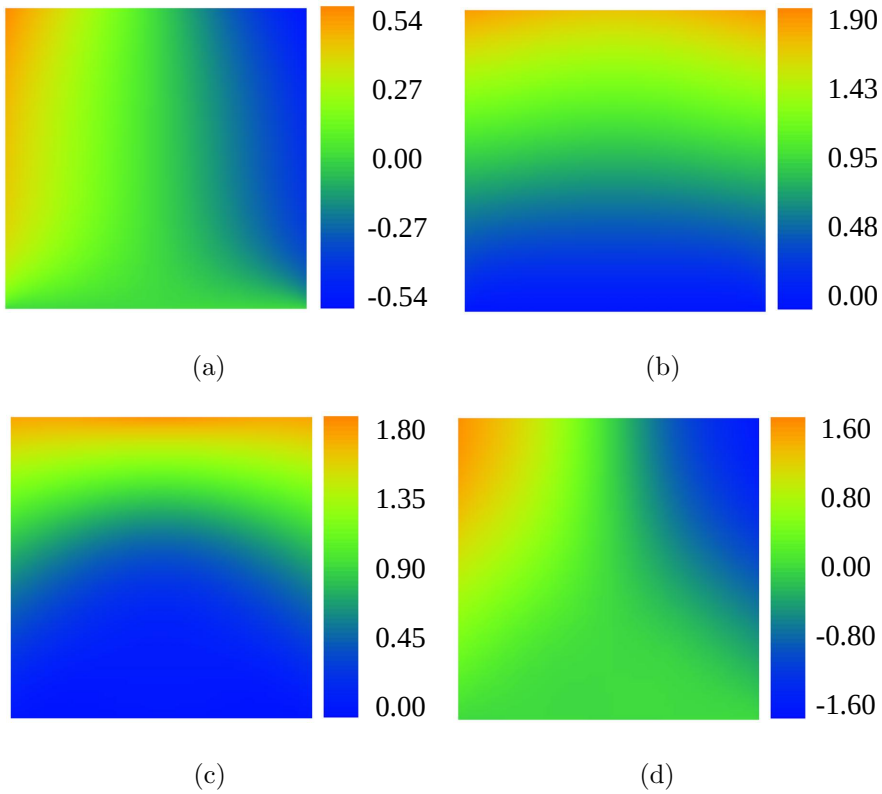

Figure 3.4: (a) Horizontal and (b) vertical components of the first (i.e., highest eigenvalue) mode and (c) horizontal and (d) vertical components of the second mode for Example 1: Simulated Soft Matrix with a Hard Inclusion.

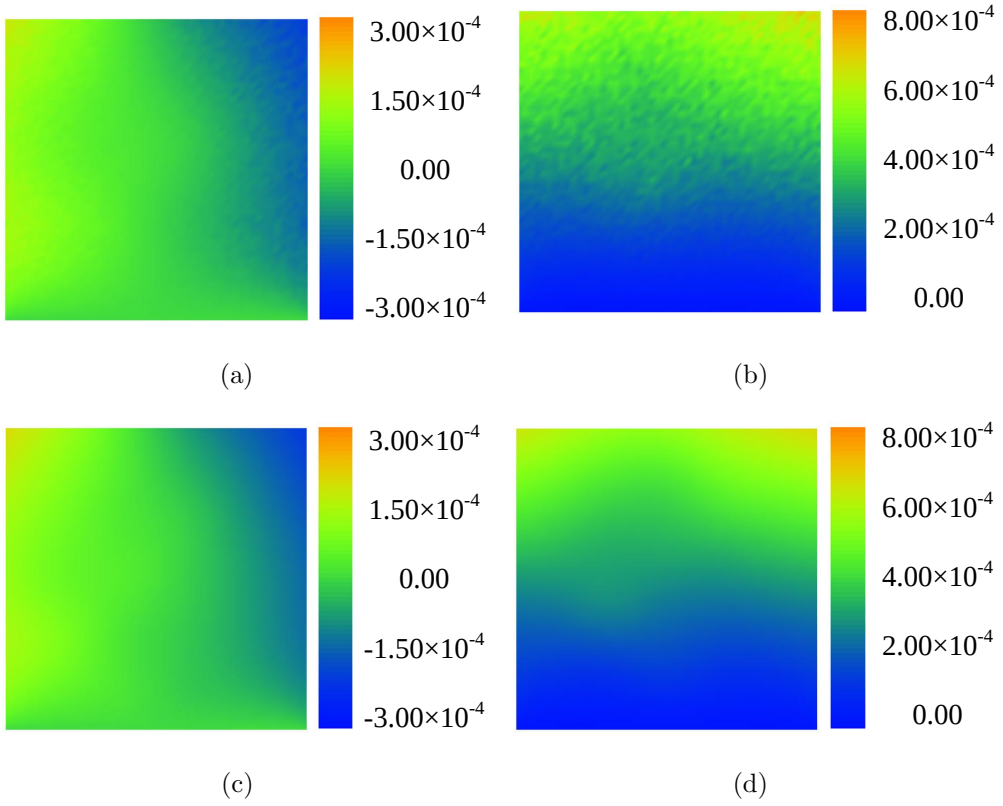

Figure 3.5: Representative example of the (a) horizontal and (b) vertical components of a simulated experimental displacement field with 5% Gaussian white noise and the (c) horizontal and (d) vertical components of the corresponding reconstructed displacement field from Gappy POD with only the discrete measurement data (color contours in units of m) for Example 1: Simulated Soft Matrix with a Hard Inclusion.

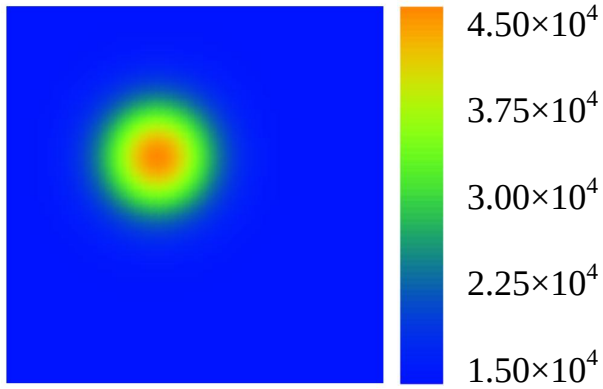

(a)

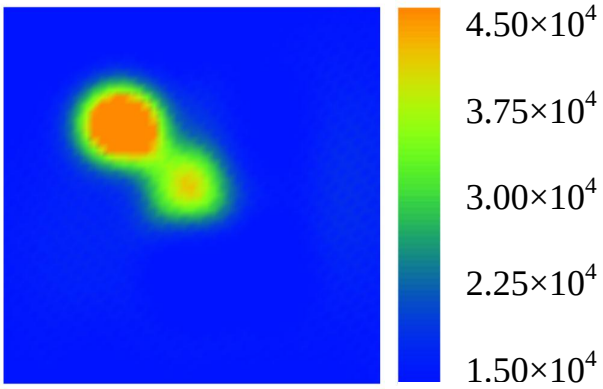

(b)

Figure 3.6: Representative example of (a) the elastic modulus distribution used to simulate experimental measurements (i.e., the target modulus distribution) and (b) the corresponding elastic modulus distribution estimated with the direct inversion approach with Gappy POD full-field displacement reconstruction from the partial-field measurements (color contours in units of Pa) for Example 1: Simulated Soft Matrix with a Hard Inclusion.

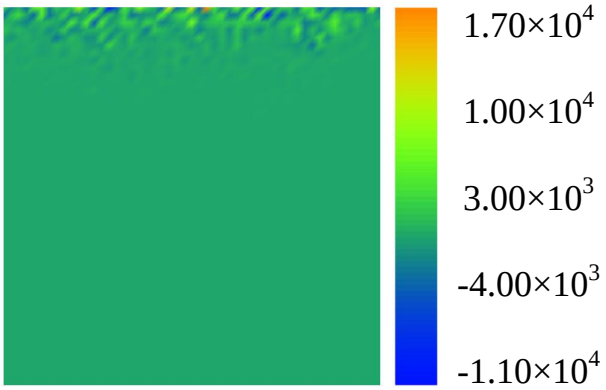

Figure 3.7: Example of an elastic modulus distribution estimated with the direct inversion approach applied directly to the full-field simulated experimental data with noise (i.e., without using Gappy POD) (color contours in units of Pa) for Example 1: Simulated Soft Matrix with a Hard Inclusion.

the modulus distribution was accurate, indicating a single harder region within the solid, and the matrix modulus value and the maximum inclusion modulus value were nearly identical to the target distribution. Again, it should be noted that the direct inversion process does not restrict the distribution of the modulus to be localized, which emphasizes the significance of having recovered the correct localization with the inversion procedure. Moreover, the accuracy of the modulus reconstruction was commensurate, if not qualitatively better, than in the alternate previously referenced works in the literature on direct inversion techniques [81, 51], with those approaches using full-field response measurements, rather than the partial-field measurements used here. To further expand on the benefits of the direct inversion with Gappy POD, Fig. 3.7 shows the elastic modulus distribution estimated by the direct inversion procedure with the original simulated full-field displacement with the added 5% Gaussian white noise. Clearly, the direct inversion procedure applied to the noisy data was unable to remotely come close to estimating the target elastic modulus distribution, indicating the significance of the noise filtering capability of the Gappy POD field reconstruction prior to direct inversion. Lastly, to show the generalization capabilities and robustness of the direct inversion with Gappy POD procedure, five additional elastic modulus reconstruction trials

Table 3.1: The mean and standard deviation of the relative L_2 and L_∞ errors with respect to the reconstructed displacement and corresponding elastic modulus distribution estimate for the five randomly generated trials of the direct inversion procedure with Gappy POD for Example 1: Simulated Soft Matrix with a Hard Inclusion.

Field	Relative L_2 Error		Relative L_∞ Error	
	Mean	Std. Dev.	Mean	Std. Dev.
Displacement	7.9%	0.3%	23.1%	4.7%
Elastic Modulus	17.3%	3.4%	41.6%	3.8%

were performed with randomly generated target localized elastic modulus distributions (similar to the representative example shown in Fig. 3.6 (a)), and the direct inversion technique was applied with the Gappy POD displacement reconstruction from the simulated measurement data with noise for each trial. Table 3.1 shows the mean and standard deviation over the five trials for the relative L_2 and L_∞ errors in the displacement reconstruction and the elastic modulus estimation comparing the direct inversion with Gappy POD results to the target simulated experimental cases. For all trials the Gappy POD with direct inversion procedure was able to reconstruct the full-field displacement and then estimate the elastic modulus distribution with an accuracy consistent with the representative example shown. In particular, the capability of the Gappy POD with direct inversion procedure to correctly localize and accurately estimate the magnitude of the elastic modulus distribution remained consistent.

3.6.1.2 Example 2: Simulated Hard Matrix with Soft Inclusions - Steady-State Dynamic Test The second example of a simulated hard matrix with soft inclusions was considered to illustrate the potential applications of nondestructive evaluation of civil or aerospace structures (e.g., characterizing damage in structural components as could be represented by a reduction in stiffness) from frequency response-based testing. A metal plate

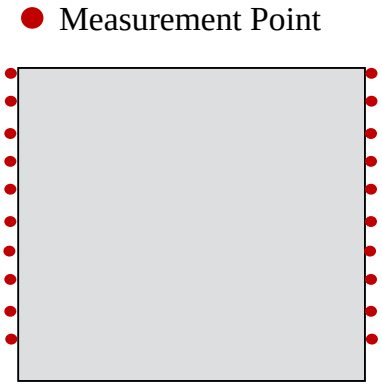

Figure 3.8: Schematic of the horizontal and vertical displacement sensor locations (red dots) for Example 2: Simulated Hard Matrix with Soft Inclusions.

was modeled as a 1 $m \times 1$ m square section with the bottom fixed to a rigid support. The entire material (matrix and inclusions) was again assumed to be known to be linear elastic, with a known Poisson's ratio of 0.3 and a known density of 2700 kg/m^3. The simulated steady-state dynamic test was implemented by applying an excitation with excitation frequency of 20 Hz and amplitude of 1 kN/m (factoring out the arbitrary thickness) uniformly to the top surface of the plate. Then, the steady-state dynamic amplitude of the horizontal and vertical displacement response to the loading was measured at 10 uniformly spaced discrete locations on both the left and right surfaces, as shown in Fig. 3.8. For this second simulated example, 1% Gaussian white noise was added to the measurements. Testing (not shown here for brevity) showed a significant tradeoff between the level of noise and the amount of measurement information in terms of the measurement accuracy. The testing showed that the more measurement information (i.e., the more sensor locations) the more tolerant the inverse solution procedure would be to measurement noise. Therefore, for this second simulated example in which significantly less measurement information was used than the first example, less measurement noise was added to ensure the simulated inverse problems would be sufficiently accurately solvable.

The process of generating the snapshots for POD was almost identical to the first simulated example, with the elastic modulus of background material assumed to be fixed at

69.0 GPa for this case, which was based upon aluminum. Again, 37 parameter combinations were used to create the snapshots. The same nine location combinations of the inclusion center were used as the first example (Fig. 3.3), the two values of the amplitude parameter used were -0.3 and -0.7 (i.e., modulus at the inclusion center of approximately 21 GPa and 48 GPa), and the two values of the breadth parameter used were 0.1 m and 0.3 m. Note that, as before, each snapshot material property distribution other than the homogeneous case contained only one inclusion. 13 out of the 37 total available POD modes were necessary to satisfy the criteria defined in Eqn. 3.43 and were retained for the Gappy POD reconstruction process. The same mesh configurations were used for the forward and inverse problem as were used for the first simulated example, with the displacement mesh having been verified to be sufficiently refined for accurately analyzing the plate deformation for all possible material property distributions.

Single Inclusion Case - Results:

Fig. 3.9 shows a representative example of a target elastic modulus distribution with a single inclusion used to generate simulated experimental measurements and the corresponding elastic modulus distribution estimated by the direct inversion with Gappy POD procedure. The relative L_2 and L_∞ errors in the displacement reconstruction were 1.7% and 4.4%, respectively, while the relative L_2 and L_∞ errors in the modulus estimation compared to the target distribution were 6.2% and 36%, respectively. The overall displacement reconstruction and modulus estimation were somewhat more accurate than the first example, most likely due to the reduction in the added measurement noise. One of the most significant observations is again that the localization of the inclusion and the matrix/inclusion modulus magnitudes were highly accurate, and with using the measurement information from only one fifth of the measurement locations as was used for the first example. To again show the consistency of these characterization results, Table 3.2 shows the mean and standard deviation over five randomly generated trials for the relative L_2 and L_∞ errors in the displacement reconstruction and the elastic modulus estimation comparing the direct inversion with Gappy POD results to the target simulated experimental cases. As previously, the results of the five random trials were consistent with the representative example shown.

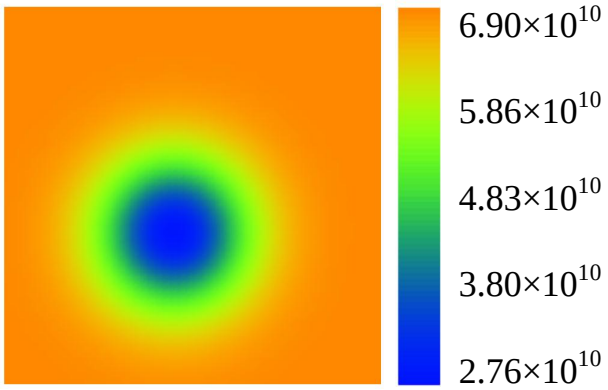

(a)

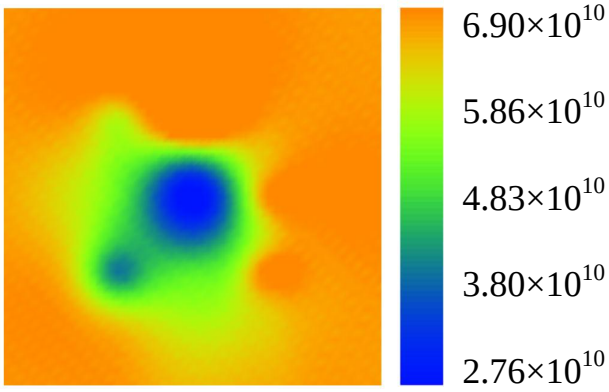

(b)

Figure 3.9: Representative single-inclusion example of (a) the elastic modulus distribution used to simulate experimental measurements (i.e., the target modulus distribution) and (b) the corresponding elastic modulus distribution estimated with the direct inversion approach with Gappy POD full-field displacement reconstruction from the partial-field measurements (color contours in units of Pa) for Example 2: Simulated Hard Matrix with Soft Inclusions.

Table 3.2: The mean and standard deviation of the relative L_2 and L_∞ errors with respect to the reconstructed displacement and corresponding elastic modulus distribution estimate for the five randomly generated trials with a single inclusion of the direct inversion procedure with Gappy POD for Example 2: Simulated Hard Matrix with Soft Inclusions.

Field	Relative L_2 Error		Relative L_∞ Error	
	Mean	Std. Dev.	Mean	Std. Dev.
Displacement	1.6%	0.2%	4.3%	0.8%
Elastic Modulus	5.6%	0.6%	32.2%	6.2%

Two and Three Inclusion Case - Results:

To examine the capability of the inverse procedure to characterize more complicated material property distributions, and particularly, to characterize distributions that are fundamentally different than the material property distributions used to generate the POD snapshots, trials were performed in which the target elastic modulus distribution had multiple soft inclusions (even though all snapshots were generated from material property distributions with at most only one inclusion). This case further addresses the common inverse characterization challenge of having *a priori* knowledge of variations being localized, but not knowing the number of these localized variations (e.g., not knowing the number of tumors or the number of damage locations). Figs. 3.10 and 3.11 show examples of target elastic modulus distributions with two and three inclusions, respectively, used to generate simulated experimental measurements and the corresponding elastic modulus distributions estimated by the direct inversion with Gappy POD procedure. For the two-inclusion case shown, the relative L_2 and L_∞ errors in the displacement reconstruction were 2.88% and 8.52%, respectively, and the relative L_2 and L_∞ errors in the modulus estimation compared to the target distribution were 9.56% and 28.19%, respectively. For the three-inclusion case shown, the relative L_2 and L_∞ errors in the displacement reconstruction were 2.73% and 8.25%, respectively, and the relative L_2 and L_∞ errors in the modulus estimation compared

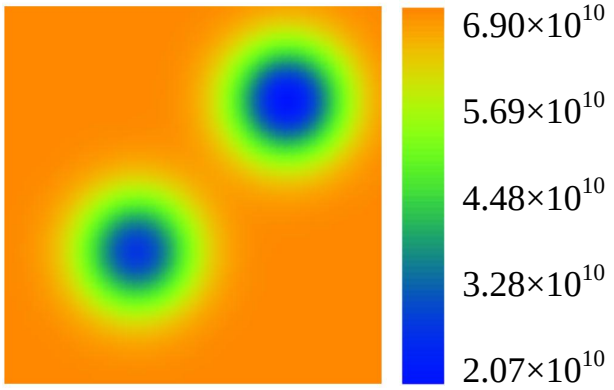

(a)

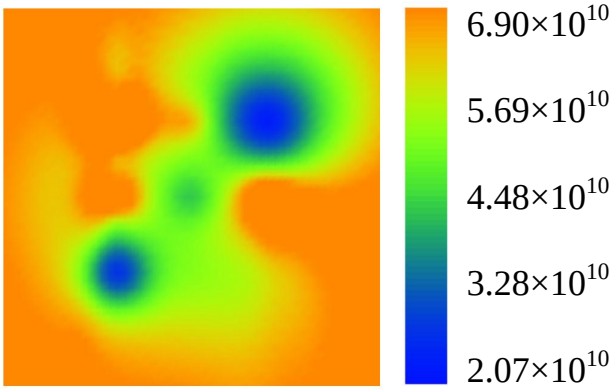

(b)

Figure 3.10: Representative two-inclusion example of (a) the elastic modulus distribution used to simulate experimental measurements (i.e., the target modulus distribution) and (b) the corresponding elastic modulus distribution estimated with the direct inversion approach with Gappy POD full-field displacement reconstruction from the partial-field measurements (color contours in units of Pa) for Example 2: Simulated Hard Matrix with Soft Inclusions.

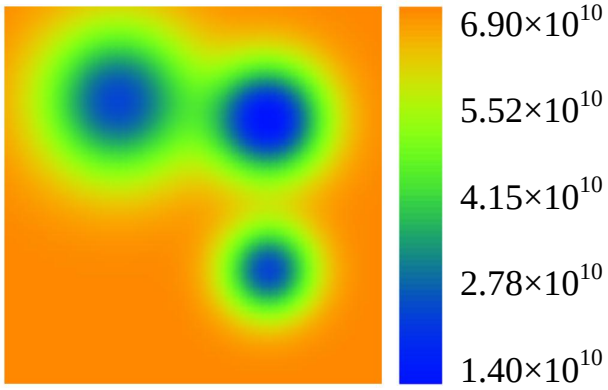

(a)

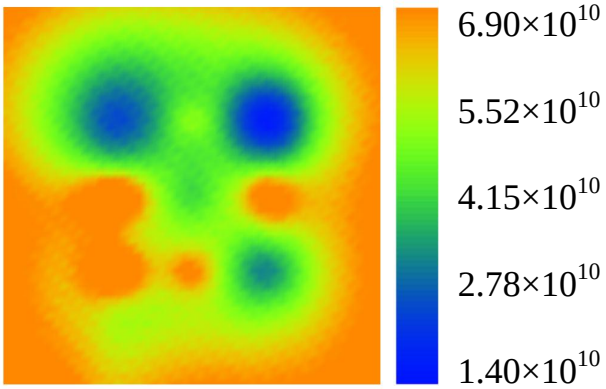

(b)

Figure 3.11: Representative three-inclusion example of (a) the elastic modulus distribution used to simulate experimental measurements (i.e., the target modulus distribution) and (b) the corresponding elastic modulus distribution estimated with the direct inversion approach with Gappy POD full-field displacement reconstruction from the partial-field measurements (color contours in units of Pa) for Example 2: Simulated Hard Matrix with Soft Inclusions.

to the target distribution were 12.98% and 40.71%, respectively. Overall, the direct inversion with Gappy POD continued to produce relatively accurate representations of the modulus distribution, but the accuracy did degrade some amount as the number of inclusions in the target distribution increased (i.e., as the target distribution become increasingly different from the snapshot distributions). What is most impressive is that, although the estimations of the modulus distributions are more dispersed than the target distributions, they were still capable of clearly identifying the number of inclusions and accurately approximate the inclusion and matrix modulus magnitudes for both the two-inclusion and three-inclusion cases. Moreover, it is worth stating again that all of these estimations (Figs. 3.9, 3.10, and 3.11) were performed using the same set of snapshots, and therefore, all three inverse problems were estimated at the combined expense of approximately 40 finite element analyses (i.e., 37 snapshots and 3 direct inversions).

3.6.2 Ultrasound Imaging Experiment: Elastography of an Arterial Construct

The final test case was intended to validate the "real-life" applicability of the approach for direct material property inversion with Gappy POD full-field response reconstruction. This test case considered an elastography problem regarding nondestructive and noninvasive characterization of the elasticity distribution of an engineered arterial construct from ultrasound measurement of the vessel deformation due to the known internal pressure. Such nondestructive capabilities could be beneficial to monitoring the progression of engineered tissues in bioreactor environments, providing accurate information with less variance between samples. Successful translation of such technologies, especially with aids of Gappy POD for realistic computational power, can result in significant savings in time and money for both noninvasive preclinical studies and clinical uses. The example followed a a nearly identical format as the work shown in [18], with the exception of the inverse solution estimation procedure (the prior work used a computationally expensive non-gradient-based optimization procedure). For simplicity, the behavior of the artery for all analyses was assumed to obey the plane strain condition, and the initial cross-sectional geometry of the artery was estimated from ultrasound imaging, as shown in Fig. 3.12. Although clearly not a perfect cylinder, the ap-

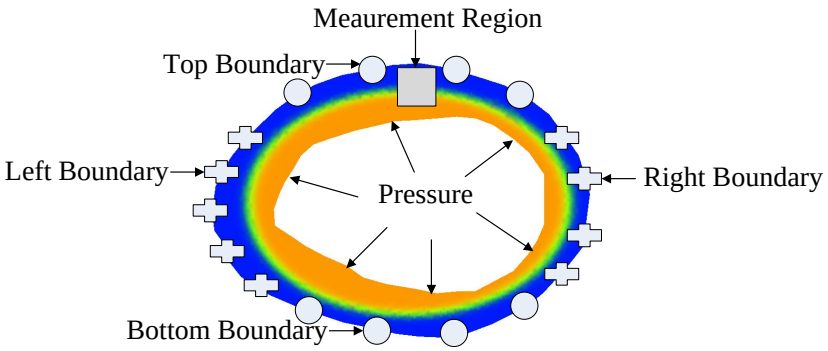

Figure 3.12: Schematic of the testing procedure used to estimate the cross-sectional elastic modulus distribution for the arterial construct from ultrasound imaging.

proximate inner and outer radius of the artery were 2.5 mm and 3.0 mm, respectively. The nondestructive and noninvasive test consisted of measuring the vertical displacement of the artery cross-section due to the known internal pulse pressure of 692 Pa using two-dimensional ultrasound speckle tracking. The behavior of the artery for all analyses was assumed to be quasi-static and linear elastic with respect to this test. In addition, to sufficiently support the artery for the analyses, the vertical displacement of an approximately 2 mm long region vertically centered on both the left and right sides of the outer surface and the horizontal displacement of an approximately 3 mm long region centered horizontally on both the top and bottom of the outer surface were assumed to be fixed. As was similarly used in [18], only 15 discrete vertical displacement measurements in the approximately $0.4\ mm \times 0.6\ mm$ rectangular region shown in Fig. 3.12 were used as the partial-field measurements for the inverse solution estimation process, as those measurements were considered the most reliable with the largest signal-to-noise ratio.

The Poisson's ratio of the entire artificial arterial construct material was assumed to be constant as 0.3 for the analyses. Therefore, the objective of the inverse characterization was again to determine the spatial distribution of the elastic modulus. However, rather than assuming the distribution was localized (as was done with the RBFs in the previous simulated examples), the stiffness of the artery was assumed to have a layered variation,

which is a realistic expectation for this application. As such, to generate the snapshots a two-layer description of the elastic modulus distribution was utilized. The two layers were defined based on a dividing ellipse centered at the centroid of the artery with a vertical radius and horizontal radius of 1.8 mm and 2.6 mm, respectively, and the modulus of the two layers was assumed to be variable between 50 kPa and 450 kPa. In addition, all snapshots were generated with the constraint that the inner layer (with modulus value E_{in}) is stiffer than the outer layer (with modulus value E_{out}) (i.e., $E_{out} < E_{in}$). Again, two layers were chosen with the specified constraint to be consistent with the prior referenced work, which accounted for the nonuniform cell growth in the construct with respect to the distance to the lumen. The specific modulus values used to generate the snapshots were chosen as every combination of the set $[50, 150, 250, 350, 450]$ kPa satisfying the specified stiffness constraint, which produced a total of 10 snapshots. 6 out of the 10 total available POD modes were necessary to satisfy the criteria defined in Eqn. 3.43 and were retained for the Gappy POD reconstruction process. A mesh of approximately 3100 quadratic triangular elements was used to simulate the snapshots for POD, and similarly to the simulated examples, the same mesh, but with linear triangular elements was used for the elastic modulus distribution estimation.

Fig. 3.13 shows the vertical displacement response field reconstructed from the 15 response measurements with the Gappy POD procedure, and more importantly, the elastic modulus distribution estimated by the direct inversion procedure. The estimated two-layer elastic modulus distribution was consistent with the referenced previous study, with the inner modulus of approximately 330 kPa considerably higher than the outer modulus of approximately 110 kPa. Furthermore, as stated in [18], the artery was tested destructively through a tensile testing method following the imaging experiment, and the bulk (i.e., averaged) elastic modulus of the artery was determined to be approximately 184 kPa. Therefore, the approximate average modulus of the distribution estimated herein of 220 kPa was relatively accurate in comparison to the destructive test (noting that the conditions for the two testing procedure were substantially different). Overall, the consistency of the results of this last example with the prior study confirm the "real-life" applicability of the approach for direct material property inversion with Gappy POD full-field response reconstruction.

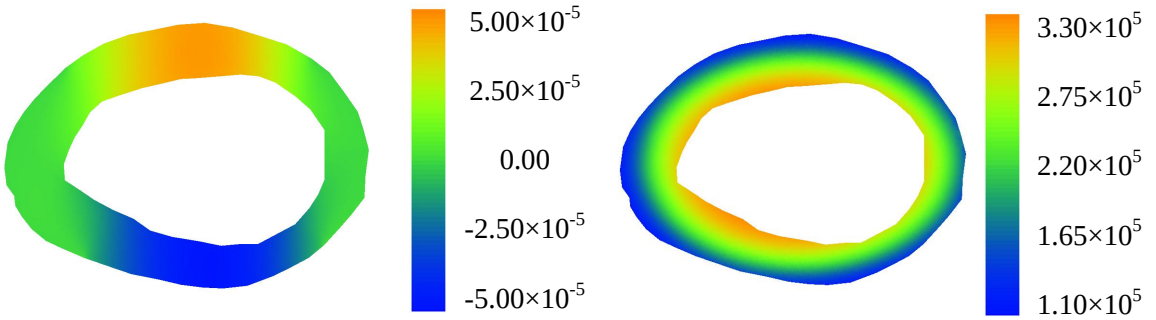

(a) (b)

Figure 3.13: (a) The vertical displacement distribution reconstructed from Gappy POD (color contours in units of m) and (b) the estimated cross-sectional elastic modulus distribution from the direct inversion procedure for the arterial construct tested with ultrasound imaging (color contours in units of Pa).

3.7 CONCLUSIONS

An approach for inverse material characterization that combines Gappy proper orthogonal decomposition with direct inversion for computationally efficient characterization with data measurements from only a portion of the system domain was presented and analyzed. The approach first uses the Gappy POD method to estimate the response field over the entire system domain from the available measurements along with any available *a priori* information regarding the potential solution distribution. Then, the full-field response is utilized within a physics-based direct inversion procedure to estimate the spatial distribution of the desired unknown material property. Through numerically simulated example inverse problems based on characterization of elastic modulus distributions with localized variations (e.g., materials with hard or soft inclusions), the inverse procedure was shown to efficiently provide accurate estimates to elastic modulus distributions from partial-field displacement measurements in both static and dynamic problems. In particular, the expense of the inverse characterization procedure, including the generation of the POD modes, was equivalent to less than

40 standard finite element analyses for the simulated examples, and once the POD modes were obtained (a one-time expense for a given system) the inversion is equivalent to a single standard finite element analysis. In addition, the direct inversion with Gappy POD response reconstruction was found to be substantially tolerant to noise in comparison to the direct inversion given the full-field noisy response (i.e., without applying Gappy POD), and this noise tolerance improved with the increase in the amount of measurement information available. The simulated examples also showed that the inversion procedure could characterize material property distributions that were substantially more complex than the distributions used to create the POD modes for the Gappy POD method (i.e., the inversion procedure had significant extrapolation capabilities). Lastly, through a physical example regarding elastography of an arterial construct from ultrasound imaging response measurements, the direct inversion approach with Gappy POD response reconstruction was validated and the practical applicability was confirmed.

4.0 A GENERALIZED AND COMPUTATIONALLY EFFICIENT INVERSE MATERIAL CHARACTERIZATION APPROACH COMBINING DIRECT INVERSION SOLUTION INITIALIZATION WITH THE ADJOINT METHOD

4.1 ABSTRACT

A computationally efficient gradient-based optimization approach for inverse material characterization from incomplete system response measurements that can utilize a generally applicable parameterization (e.g., finite element-type parameterization) is presented and evaluated. The key to this inverse characterization algorithm is the use of a direct inversion strategy with Gappy proper orthogonal decomposition (POD) response field estimation to initialize the inverse solution estimate prior to gradient-based optimization. Gappy POD is used to estimate the complete (i.e., all components over the entire spatial domain) system response field from incomplete (e.g., partial spatial distribution) measurements obtained from some type of system testing along with some amount of *a priori* information regarding the potential distribution of the unknown material property. The estimated complete system response is used within a physics-based direct inversion procedure with a finite element-type parameterization to estimate the spatial distribution of the desired unknown material property with minimal computational expense. Then, this estimated spatial distribution of the unknown material property is used to initialize a gradient-based optimization approach, which uses the adjoint method for computationally efficient gradient calculations, to produce the final estimate of the material property distribution. The three-step ((1) Gappy POD, (2) direct inversion, and (3) gradient-based optimization) inverse characterization approach is evaluated through simulated test problems based on the characterization of elastic modulus

distributions with localized variations (e.g., inclusions) within simple structures. Overall, this inverse characterization approach is shown to efficiently and consistently provide accurate inverse characterization estimates for material property distributions from incomplete response field measurements. Moreover, the solution procedure is shown to be capable of extrapolating significantly beyond the initial assumptions regarding the potential nature of the unknown material property distribution.

4.2 INTRODUCTION

Computational methods for the solution of inverse problems (e.g., characterization, design, etc.) in mechanics (e.g., relating to solid mechanics, heat transfer, etc.) are becoming ever more popular in a variety of fields in science and engineering. In particular, applications in the characterization of material property distributions span interest areas from civil engineering (e.g., structural damage characterization [72, 80]) to medicine (e.g., tissue characterization for disease diagnosis [8, 46]), where quantitative estimation of a variety of material parameters can provide critical information relating to the state of the system. A common structure of quantitative inverse material characterization approaches is to couple a numerical representation of the system forward problem (e.g., a finite element representation of the system response given the material properties) with some type of optimization to estimate the material properties that lead to a "best match" between the response estimated by the forward numerical representation and the available experimentally measured response. Such computational methods to estimate inverse solutions provide quantitative solutions and are generally applicable regardless of the physics of interest and response measurement type. However, there are several significant challenges depending on the application of interest as well, with a wide range of variations in the inverse solution method specifics. Common differences include variations in the parameterization of the unknown material field, numerical analysis technique, and optimization approach, with each having significant tradeoffs in terms of generalization of the applicability, solution accuracy, and computational efficiency.

One way in which computational inverse solution strategies can be divided is into those that are iterative and those that are non-iterative (i.e., direct). A common direct approach is to relate the measured response to the unknown material property distribution parameters based on the manipulation of the forward boundary value problem and a least-squares criteria, which creates a solution process similar to that of solving the forward problem itself (e.g., similar in process to a finite element analysis to predict the deformation response of a solid given geometry, material properties, and boundary conditions) [51, 81, 50]. Thus, the solution estimate can be obtained at a cost on the order of a single numerical analysis of the forward problem, even with a relatively generalized parameterization of the spatial distribution of the unknown property (e.g., finite element-type parameterization). However, one common challenge of the direct inversion approaches is that the entire (or nearly entire) spatial distribution (i.e., full-field) of the system response (e.g., displacement) must be measured to successfully characterize a distribution of unknown material properties. In addition, direct approaches are often relatively noise sensitive, with solution quality degrading relatively quickly with increasing levels of measurement noise.

Iterative optimization-based approaches are typically better equipped than direct methods to estimate inverse solutions provided with response measurements from only a portion of the system domain (i.e., partial-field measurements) or otherwise incomplete measurement information (e.g., single directional components of displacement). Conceptually these iterative approaches can be further divided into those that use use non-gradient-based optimization (e.g., random search, genetic algorithm, etc.) [9, 73] and those that use gradient-based optimization (e.g., Newton's method, conjugate gradient, etc.) [46, 22]. Non-gradient-based methods often have more significant global search capabilities in comparison to the gradient-based optimization approaches, which can become trapped in local minima (i.e., an inaccurate solution). However, non-gradient-based methods typically require substantially more iterations (i.e., computational time) to converge to a solution approximation than gradient-based approaches, which can be prohibitive for many applications. Moreover, the computational expense of non-gradient-based methods increases substantially with increasing number of unknown parameters (i.e. the curse of dimensionality), leading to the use of simplified (i.e., less generally applicable) parameterizations of the unknown property field.

In contrast, gradient-based methods are not only substantially more computationally efficient overall, but are also not as affected by the curse of dimensionality, particularly if using an adjoint approach or something similar to calculate the gradients [26, 20, 48]. Therefore, gradient-based methods are capable of converging to a solution estimate with relative computational efficiency, even with a generally applicable high-dimensional finite-element type parameterization of the unknown material property field. Unfortunately, as stated, gradient-based methods are local in nature, and unless the initial estimate of the unknown property field provided is relatively accurate, the final solution estimate is likely to be inaccurate. Furthermore, limitations in the amount of measurement data and/or high-dimensional parameterizations of the unknown field often leads to complicated (non-convex) error surfaces for the optimization, and while regularization approaches can somewhat relieve this challenge [47, 46, 63], the importance of the initial estimate accuracy is increased significantly.

The present work investigates an approach to utilize information that is available *a priori* regarding the nature of the unknown property distribution (e.g., that the distribution has localized variations) to initialize a gradient based optimization procedure to achieve a unique level of efficiency and accuracy to estimate generalized (i.e., arbitrarily shaped) distributions of material properties from partial-field measurements without the need for regularization or any kind of direct initial solution estimate. In particular, the approach is presented in the context of characterizing the spatial distribution of the elastic modulus (i.e., elastography) provided with displacement response measurements over some portion of the solid domain. The approach utilizes the Gappy proper orthogonal decomposition (POD) machine learning technique to build a data reconstruction tool based on the available *a priori* solution knowledge that can estimate the full-field response distribution given the available partial-field measurements. The estimated full-field response is then applied within a direct inversion strategy with a general finite element-type parameterization of the unknown field to produce an initial estimate of the spatial distribution of the unknown material property over the entire domain. Lastly, this initial estimate is refined with a gradient-based optimization strategy using the adjoint method for computationally efficient gradient calculations to produce the final estimate of the material property distribution.

The following section presents the details of the inverse material characterization algorithm, including (1) the adjoint formulation for efficient gradient calculation within the gradient-based optimization approach, (2) the direct inversion algorithm to estimate the spatial distribution of elastic modulus provided with a full-field displacement response distribution and the boundary conditions corresponding to the test method used to produce the measurements, and (3) the Gappy POD to reconstruct a full-field response estimate from given partial-field measurements. Then, simulated examples relating to characterization of localized elastic modulus distributions in solids are presented to examine the capabilities of the generalized inverse characterization approach, which is followed by the concluding remarks.

4.3 INVERSE MATERIAL CHARACTERIZATION ALGORITHM

As discussed, although potentially applicable to a variety of different physical systems, material properties, and testing methods, the inverse characterization approach is presented in the specific context of characterization of the elastic modulus spatial distribution of a solid from partial-field displacement measurements. In particular, for the following presentation, it is assumed that some type of steady-state dynamic mechanical testing has been applied, with the solid of interest excited to steady state at one or more excitation frequencies and the resulting steady-state displacement amplitude measured at several locations throughout the solid. Thus, neglecting body forces and damping, assuming displacements and strains are small, and assuming that the system variables vary harmonically in time at angular excitation frequency ω, the steady-state dynamic governing equations describing the associated forward elasticity problem (i.e., the strong form) can be given as:

$$\nabla \cdot \boldsymbol{\sigma}(\vec{x},\omega) + \omega^2 \rho(\vec{x}) \vec{u}(\vec{x},\omega) = \vec{0}, \quad \forall \vec{x} \in \Omega, \tag{4.1}$$

$$\boldsymbol{\sigma}(\vec{x},\omega) = \boldsymbol{C}^{IV}(\vec{x}) : \boldsymbol{\varepsilon}(\vec{x},\omega), \tag{4.2}$$

$$\boldsymbol{\varepsilon}(\vec{x},\omega) = \frac{1}{2}\left(\nabla\vec{u}(\vec{x},\omega) + (\nabla\vec{u}(\vec{x},\omega))^T\right), \tag{4.3}$$

$$\boldsymbol{\sigma}(\vec{x},\omega)\cdot\vec{n}(\vec{x}) = \vec{T}(\vec{x},\omega), \quad \forall\vec{x}\in\Gamma_{\vec{T}}, \tag{4.4}$$

and

$$\vec{u}(\vec{x},\omega) = \vec{u}_0(\vec{x},\omega), \quad \forall\vec{x}\in\Gamma_{\vec{u}}, \tag{4.5}$$

where $\rho(\vec{x})$ is the mass density, $\boldsymbol{\sigma}(\vec{x},\omega)$ is the Cauchy stress amplitude tensor, $\vec{u}(\vec{x},\omega)$ is the displacement amplitude vector, Ω is the domain of the structure, $\boldsymbol{\varepsilon}(\vec{x},\omega)$ is the small strain amplitude tensor, $\boldsymbol{C}^{IV}(\vec{x})$ is the 4^{th}-order elasticity tensor, $\vec{n}(\vec{x})$ is the unit outward normal vector to the surface of the domain, $\vec{T}(\vec{x},\omega)$ and $\Gamma_{\vec{T}}$ are the applied traction amplitude vector and the portion of the domain surface where this traction is applied, respectively, and $\vec{u}_0(\vec{x},\omega)$ and $\Gamma_{\vec{u}}$ are the applied displacement amplitude vector and the portion of the domain surface where displacement is known, respectively. Note that the entire formulation is applicable and easily converted to the static case by simply setting the momentum term to zero.

The first step in setting up the optimization-based computational inverse solution procedure is to construct an appropriate objective functional. This objective functional should somehow quantify the difference between the experimentally measured system response and the corresponding response that is predicted by the numerical representation of the system (i.e., solution to Eqns. (4.1)-(4.5)) given an estimate to the unknown material properties, as (note that dependencies on $\vec{x}$ and ω should be inferred and were left off of the following presentation for brevity):

$$f(\vec{p}) = \left\|\vec{u}\,(\vec{p}) - \vec{u}^M\right\|_{\Omega^M}, \tag{4.6}$$

where, for this example, $\vec{u}^M$ would be the experimentally measured displacement amplitudes, $\vec{u}(\vec{p})$ is the numerical simulated displacement amplitudes for a given estimate to the material parameter vector, $\vec{p}$, and $\|\cdot\|_{\Omega^M}$ is some chosen suitable metric norm that combines the contribution of all measurement locations and excitation frequencies to produce a scalar measurement error. Then, all that is necessary is to apply a suitable optimization algorithm,

to minimize the objective functional, f, with respect to the unknown material parameters, subject to the constraint of the above boundary value problem (BVP) and any physical bounds on the unknown parameters. There are several different gradient-based optimization algorithms that can be (and have been in prior studies [75]) applied to minimize the objective functional with respect to the unknown material parameters, and thereby, estimate the inverse problem solution. For example, the standard interior point method was used for the examples presented herein, which among other algorithmic details that can be found in [70], uses the gradient to approximate the inverse of the Hessian with a BFGS method [75] to update the solution estimate at each iteration. Therefore, much like many other commonly used gradient-based optimization algorithms, the gradient is the main driver of the optimization, and therefore, the most critical calculation within the optimization procedure.

By far the most challenging aspect (at least computationally) of calculating the gradient of the objective functional presented above is the need to calculate the partial derivative of the displacement response with respect to the material parameters ($\vec{p}$), with the relationship between those two quantities being defined by the above BVP. As such, to maintain computational efficiency, the present work used the adjoint method for the gradient calculation [63]. The adjoint method requires only two numerical solutions of BVPs to calculate the necessary gradient, the given BVP and a corresponding adjoint BVP, with both having the same approximate computational expense. Therefore, the adjoint method represents a substantial computational savings in comparison to alternate methods, such as finite difference methods, which require at least $N + 1$ BVP solutions, or direct differentiation of the BVP, which requires N BVP solutions, where N is the number of unknown parameters in the optimization problem [46]. Particularly for generalized (e.g., finite element-type) parameterizations of the unknown property with large numbers of parameters to be determined, the adjoint method, or something similar, is a necessity for practical applicability.

In brief (see the provided references for additional details), the adjoint method for the type of elastography problem considered here begins by constructing a Lagrangian of the form:

$$\mathcal{L}\left(\vec{u}\left(\vec{p}\right), \vec{\gamma}, \vec{p}\right) = f(\vec{p}) + a\left(\vec{u}(\vec{p}), \vec{\gamma}; \vec{p}\right) - \left(\vec{T}, \vec{\gamma}\right), \tag{4.7}$$

such that:

$$\frac{d\mathcal{L}}{d\vec{p}} = \frac{df}{d\vec{p}} = \frac{\partial \mathcal{L}}{\partial \vec{p}} + \frac{\partial \mathcal{L}}{\partial \vec{u}} \frac{\partial \vec{u}}{\partial \vec{p}}, \tag{4.8}$$

where,

$$\begin{aligned} a(\vec{u}(\vec{p}), \vec{\gamma}) = \int_{\Omega} \frac{1}{2} \left(\nabla \vec{\gamma} + (\nabla \vec{\gamma})^T \right) : \boldsymbol{C}^{IV}(\vec{p}) : \frac{1}{2} \left(\nabla \vec{u}(\vec{p}) + (\nabla \vec{u}(\vec{p}))^T \right) d\vec{x} \\ - \int_{\Omega} \rho \omega^2 \vec{\gamma} \cdot \vec{u}(\vec{p}) d\vec{x}, \end{aligned} \tag{4.9}$$

$$\left(\vec{T}, \vec{\gamma} \right) = \int_{\Gamma_{\vec{T}}} \vec{\gamma} \cdot \vec{T} \, d\vec{x}, \tag{4.10}$$

and $\vec{\gamma}$ is a Lagrange multiplier. To avoid the previously mentioned computationally expensive component, without loss of generality, the multiplying term in the Lagrangian gradient expansion can be set to zero to produce the adjoint BVP of the form:

$$\nabla \cdot \left(\boldsymbol{C}^{IV}(\vec{p}) : \frac{1}{2} \left(\nabla \vec{\gamma}(\vec{p}) + (\nabla \vec{\gamma}(\vec{p}))^T \right) \right) + \omega^2 \rho \vec{\gamma}(\vec{p}) = \vec{0}, \quad \forall \vec{x} \in \Omega, \tag{4.11}$$

$$\boldsymbol{C}^{IV}(\vec{p}) : \frac{1}{2} \left(\nabla \vec{\gamma}(\vec{p}) + (\nabla \vec{\gamma}(\vec{p}))^T \right) = \frac{df}{d\vec{u}(\vec{p})}, \quad \forall \vec{x} \in \Gamma_{\vec{T}}, \tag{4.12}$$

and

$$\vec{\gamma}(\vec{p}) = \vec{0}, \quad \forall \vec{x} \in \Gamma_{\vec{u}}. \tag{4.13}$$

Finally, using the solution of the original BVP ($\vec{u}$ from Eqns. (4.1)-(4.5)) and the solution of the adjoint BVP ($\vec{\gamma}$ from Eqns. (4.11)-(4.13)) for a given set of material parameters, the gradient of the objective functional for those material parameters can be calculated as:

$$\frac{d\mathcal{L}}{d\vec{p}} = \frac{\partial \mathcal{L}}{\partial \vec{p}} = \frac{\partial a(\vec{u}, \vec{\gamma}; \vec{p})}{\partial \vec{p}}. \tag{4.14}$$

As discussed in the Introduction, providing a sufficiently accurate initial guess for the unknown material parameters is critical to ensuring an accurate final solution estimate using the computational inverse characterization procedure with gradient-based optimization. The importance of this initial guess is even further heightened when applying a generalized parameterization of the unknown field and when not using any kind of solution regularization (as is the case in the above presentation). To overcome this challenge/limitation, the present work uniquely uses a direct inversion strategy to estimate an initial guess for the unknown material property distribution, which is detailed in the following.

4.3.1 Direct Inversion for Material Property Distribution Estimation

Note that the following direct inversion formulation assumes that a complete displacement response field is available or has been approximated from the response measured with the given testing method. Then, the first step in the inverse solution formulation to estimate the spatial distribution of the elastic modulus of a solid is to separate the elastic modulus ($E(\vec{x})$) from the elasticity matrix $[D]$ (i.e., the Voigt notation version of $\boldsymbol{C}^{IV}$) as:

$$[D] = [D_I]E(\vec{x}), \tag{4.15}$$

where $[D_I]$ is now only a function of Poisson's ratio (ν). Applying the same general Galerkin weak form procedure as is typically done for the forward BVP [59] to approximate displacement, but now to approximate the elastic modulus, the inverse problem weak form for the steady-state dynamic boundary value problem can be written as:

$$\int_{\Omega} \{\nabla \delta\vec{E}(\vec{x})\}^T \{\boldsymbol{\sigma}_I(\vec{x},\omega)\} E(\vec{x})\ d\vec{x} = \int_{\Omega} \rho(\vec{x})\omega^2 \delta\vec{E}(\vec{x}) \cdot \vec{u}(\vec{x},\omega)\ d\vec{x} + \int_{\Gamma_{\vec{T}}} \delta\vec{E}(\vec{x}) \cdot \vec{T}(\vec{x},\omega)\ d\vec{x}, \tag{4.16}$$

where

$$\{\boldsymbol{\sigma}_I(\vec{x},\omega)\} = [D_I]\{\varepsilon(\vec{x},\omega)\}, \tag{4.17}$$

$\{\varepsilon(\vec{x},\omega)\}$ is the Voigt notation version of the small strain amplitude tensor, $\delta\vec{E}(\vec{x})$ is the virtual elastic modulus vector (matching the dimension of the displacement field, and therefore, the number of equilibrium equations, even though the modulus itself is a scalar), and $\{\nabla\delta\vec{E}(\vec{x})\}$ is the corresponding gradient in Voigt notation.

Applying standard procedures of the finite element method to discretize the domain into finite elements to represent the elastic modulus as well as the displacement (assuming that the given full-field displacement response has been discretized as such), and again using Voigt notation where applicable, the elastic modulus, the virtual elastic modulus vector, the displacement vector, and their corresponding gradients can be approximated as:

$$E(\vec{x}) \approx [N_E(\vec{x})]\{E^e\}, \tag{4.18}$$

$$\delta\vec{E}(\vec{x}) \approx [N_{\delta\vec{E}}(\vec{x})]\{\delta\vec{E}^e\}, \tag{4.19}$$

$$\vec{u}(\vec{x},\omega) \approx [N_{\vec{u}}(\vec{x})]\{\vec{u}^e(\omega)\}, \tag{4.20}$$

$$\{\nabla E(\vec{x})\} \approx [B_E(\vec{x})]\{E^e\}, \tag{4.21}$$

$$\{\nabla\delta\vec{E}(\vec{x})\} \approx [B_{\delta\vec{E}}(\vec{x})]\{\delta\vec{E}^e\}, \tag{4.22}$$

and

$$\{\varepsilon(\vec{x},\omega)\} \approx [B_{\vec{u}}(\vec{x})]\{\vec{u}^e(\omega)\}, \tag{4.23}$$

where $[N_E(\vec{x})]$ is the matrix of shape functions for elastic modulus interpolation, $[N_{\delta\vec{E}}(\vec{x})]$ is the expanded version (to match the dimensions of the displacement) of the matrix of shape functions for elastic modulus interpolation, $[N_{\vec{u}}(\vec{x})]$ is the standard matrix of shape functions for displacement interpolation, and $[B_E(\vec{x})]$, $[B_{\delta\vec{E}}(\vec{x})]$, and $[B_{\vec{u}}(\vec{x})]$ are the respective matrices of these shape function spatial derivatives. Substituting the discretization (Eqns. (4.18)-(4.23)) into Eqn. (4.16), eliminating the arbitrary virtual elastic modulus field vector, and assembling individual element contributions, the final finite element equations for the direct inversion elastography problem can be depicted as:

$$[K_I]\{E\} = \{P_I\} + [M_I]\{u\}, \tag{4.24}$$

where

$$[K_I] = \sum_{element} \int_{\Omega^e} [B_{\delta\vec{E}}(\vec{x})]^T [D_I][B_{\vec{u}}(\vec{x})]\{\vec{u}^e\}[N_E(\vec{x})]\ d\vec{x}, \tag{4.25}$$

$$[M_I] = \sum_{element} \int_{\Omega^e} \rho(\vec{x})\omega^2 [N_{\delta\vec{E}}(\vec{x})]^T [N_{\vec{u}}(\vec{x})]\ d\vec{x}, \tag{4.26}$$

and

$$\{P_I\} = \sum_{element} \int_{\Gamma^e_{\vec{T}}} [N_{\delta\vec{E}}(\vec{x})]^T \vec{T}(\vec{x},\omega)\ d\vec{x}. \tag{4.27}$$

Since $[K_I]$ is typically non-square and Eqn. (4.24) is typically an overdetermined system (e.g., $[K_I]$ has dimensions $3N \times N$, where N is the number of nodes in the mesh if the

same mesh is used for both displacement and elastic modulus), the elastic modulus cannot be estimated by simply inverting $[K_I]$. Thus, as is common, a least-squares approach was used here to solve Eqn. (4.24) for $\{E\}$. As such, the nodal values of elastic modulus can be determined as:

$$\{E\} = \left([K_I]^T[K_I]\right)^{-1}[K_I]^T\left(\{P_I\} + [M_I]\{u\}\right). \tag{4.28}$$

One final important point is that it is necessary to invalidate the equations corresponding to the essential boundary conditions in the forward BVP prior to the solution of Eqn. (4.28). Eliminating these equations is a common approach that is necessary to obtain a well-behaved solution to the direct inversion problem. Thus, prior to solving Eqn. (4.28) the rows in Eqn. (4.24) corresponding to nodes where essential boundary conditions are present are set to zero, such that:

$$[K_I][i,:] = 0, \quad \text{if} \quad \vec{x}_i \in \Gamma_{\vec{u}}, \quad \text{for} \quad i = 1, 2, ..., N, \tag{4.29}$$

$$[M_I]\{u\}[i] = 0, \quad \text{if} \quad \vec{x}_i \in \Gamma_{\vec{u}}, \quad \text{for} \quad i = 1, 2, ..., N, \tag{4.30}$$

and

$$\{P_I\}[i] = 0, \quad \text{if} \quad \vec{x}_i \in \Gamma_{\vec{u}}, \quad \text{for} \quad i = 1, 2, ..., N. \tag{4.31}$$

Again note that the above formulation requires the complete displacement response field to be available, yet the intention of the overall inverse characterization procedure presented herein is to be capable of utilizing only partial-field response measurements. As such, it is necessary to have a means to estimate the full-field response from partial-field measurements to use this direct inversion strategy. To address this need the following presents a machine learning approach to create a tool based on information available *a priori* regarding the expected nature of the full-field response distribution that can estimate a full-field response from partial-field measurements.

4.3.2 Gappy Proper Orthogonal Decomposition

Gappy POD is an extension of the traditional POD approach that was first developed and presented by Everson and Sirovich [19] for the purpose of filling in missing information to

reconstruct marred photos. Subsequently, Gappy POD has shown substantial capabilities to accurately reconstruct physical processes from partial-field measurement data, especially for fluid flow problems [69, 67, 74, 78, 64].

The Gappy POD process begins with the standard POD method. Given a set of n fields (referred to as "snapshots"), $\{\vec{u}_k(\vec{x})\}_{k=1}^{n}$, POD can be interpreted as an approach to determine the set of m orthogonal basis functions (i.e., modes), $\left\{\vec{\phi}_i(\vec{x})\right\}_{i=1}^{m}$, that are optimal in the average L_2-error sense for representing each given field and, if the given fields are representative, any similar field as:

$$\vec{u}(\vec{x}) \approx \vec{u}^*(\vec{x}) = \sum_{i=1}^{m} a_i \vec{\phi}_i(\vec{x}), \tag{4.32}$$

where a_i is the modal coefficient corresponding to the i^{the} mode ($\vec{\phi}_i(\vec{x})$). Then, the POD optimization problem to define these modes can be written as:

$$\underset{\left\{\vec{\phi}_i(\vec{x})\right\}_{i=1}^{m}}{Minimize} \left\langle \|\vec{u}(\vec{x}) - \vec{u}^*(\vec{x})\|^2_{L_2(\Omega)} \right\rangle, \tag{4.33}$$

where

$$\langle \vec{u} \rangle = \frac{1}{n} \sum_{k=1}^{n} \vec{u}_k, \tag{4.34}$$

and $\vec{u}^*$ is the best approximation of the snapshots from the modes (i.e., the projection of each snapshot onto the modes). Based on this optimization problem and applying the method of snapshots (see [2] for additional details), a maximum of n POD modes can be calculated through the solution of the following eigenvalue problem:

$$\frac{1}{n} \sum_{k=1}^{n} A_{jk} C_k = \lambda C_j, \tag{4.35}$$

where

$$A_{jk} = \int_{\Omega} \vec{u}_j(\vec{x}) \cdot \vec{u}_k(\vec{x}) \, d\vec{x}, \tag{4.36}$$

and then the i^{th} mode is given as:

$$\vec{\phi}_i(\vec{x}) = \frac{1}{\lambda^{(i)} n} \sum_{k=1}^{n} \vec{u}_k(\vec{x}) \, C_k^{(i)}. \tag{4.37}$$

Gappy POD diverges from standard POD in how the modes are utilized. If the full spatial distribution of a field is available, the modal coefficients (a_i) needed to reconstruct that field with the POD modes can be easily obtained by projecting the modes onto the field as:

$$a_i = \int_\Omega \vec{u}\left(\vec{x}\right) \cdot \vec{\phi}_i\left(\vec{x}\right) d\vec{x}. \tag{4.38}$$

Alternatively, the objective of Gappy POD is to provide a means to reconstruct the full spatial distribution of a field using the POD modes, but with only a partial spatial distribution of the field given. Defining $\hat{\vec{u}}\left(\vec{x}\right)$ as the given partial distribution of the field of interest such that $\hat{\vec{u}}\left(\vec{x}\right)$ is (incorrectly) 0 anywhere data is unavailable, then $\hat{\vec{u}}\left(\vec{x}\right)$ can be expressed in terms of the corresponding, but unknown, full spatial distribution as:

$$\hat{\vec{u}}\left(\vec{x}\right) = \beta\left(\vec{x}, \vec{u}\right) \vec{u}\left(\vec{x}\right), \tag{4.39}$$

where $\beta\left(\vec{x}, \vec{u}\right)$ is a mask function that is defined as 0 where data is unavailable and 1 where data is available. Assuming that the full spatial distribution can be approximated with the POD modes as defined in Eqn. (4.32), an approximation of $\hat{\vec{u}}\left(\vec{x}\right)$ can be written in terms of the POD modes as:

$$\hat{\vec{u}}^*\left(\vec{x}\right) = \beta\left(\vec{x}, \vec{u}\right) \sum_{i=1}^{m} a_i \vec{\phi}_i\left(\vec{x}\right). \tag{4.40}$$

Then, based upon a least-squares criteria, the optimal set of modal coefficients to reconstruct the full spatial distribution of the field can be defined as that which minimizes an error function of the form:

$$\varepsilon = \int_\Omega \left[\beta\left(\vec{x}, \vec{u}\right) \vec{u}\left(\vec{x}\right) - \beta\left(\vec{x}, \vec{u}\right) \sum_{i=1}^{m} a_i \vec{\phi}_i(\vec{x}) \right]^2 d\vec{x}. \tag{4.41}$$

Applying the necessary condition for extrema of a function by setting the derivative of the error function with respect to the modal coefficients to zero, the optimal set of modal coefficients, {a}, to reconstruct the full spatial distribution of the field can be determined from the solution of:

$$[M]\{a\} = \{f\}, \tag{4.42}$$

where

$$M_{ij} = \int_\Omega \beta\left(\vec{x}, \vec{u}\right) \vec{\phi}_i(\vec{x}) \cdot \vec{\phi}_j(\vec{x}) \; d\vec{x}. \tag{4.43}$$

and

$$f_i = \int_\Omega \beta\left(\vec{x}, \vec{u}\right) \vec{u}(\vec{x}) \cdot \vec{\phi}_i(\vec{x}) \; d\vec{x}. \tag{4.44}$$

A last important implementation aspect for this Gappy POD approach is that only a portion ($m << n$) of the set of modes that can be obtained with POD are typically necessary to be retained for further use in the full-field estimation process. As the associated eigenvalues from the solution of Eqn. (3.3) relate to the value of each mode for the representation of the given dataset, typically some heuristic is used based on the relative sum of the associated eigenvalues to determine the modes to retain for further use [67, 74].

One additional note is that the Gappy POD approach can also act as somewhat of a noise filter during the reconstruction process, thereby providing an added benefit of reducing the effects of measurement noise on the subsequent direct inversion solution procedure. However, any reconstructed full-field response is still only an approximation of the true full-field response, with the accuracy of the response estimation and direct inversion solution estimate significantly dependent upon the amount of measurement data (higher accuracy with more data).

4.4 EXAMPLES AND DISCUSSION

Two sets of numerically simulated inverse characterization problems were considered to evaluate the potential benefits and capabilities of the gradient-based optimization approach initialized with direct inversion from Gappy POD response approximation. Both example sets involved characterization of an elastic modulus distribution with localized inclusions (hard or soft) in plate structures from partial-field response measurements. Furthermore, both inverse characterization problems were based upon some type of simulated nondestructive testing (dynamic or static) in the linear range of the solid behavior (such that the governing equations shown in Section 4.3 apply), with an actuation force applied uniformly to the top surface, the bottom surface fixed, and with the horizontal and vertical displacement response to the loading measured at 10 uniformly spaced discrete locations on both

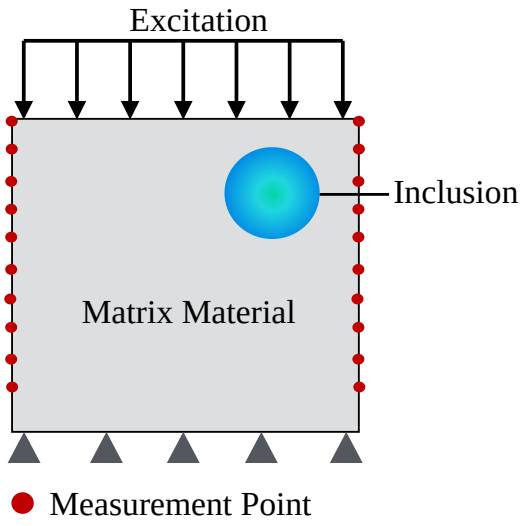

Figure 4.1: Schematic for the numerically simulated examples representing characterization of an elastic modulus distribution with an inclusion based on mechanical testing involving the excitation and measurement points shown.

the left and right surfaces. Fig. 4.1 shows a schematic of the example cases, including the boundary conditions and sensor locations.

The "experimental" nondestructive test measurements were simulated using the standard finite element method. In addition, both examples used the plane stress assumption to reduce the computational expense. To add realism to the simulated experiments, for all trials 1% Gaussian white noise was also added to the simulated measurements as:

$$u^{expn} = u^{exp}\left(1 + 0.01\upsilon\right), \tag{4.45}$$

where u^{expn} and u^{exp} are the simulated experimental displacement measurements with noise and without noise, respectively, and υ is a normally distributed random variable with unit variance and zero mean. Note that testing (not shown here for brevity) showed a significant tradeoff between the level of noise and the amount of measurement information in terms of the final solution accuracy. The testing showed that the more measurement information

(i.e., the more sensor locations) the more tolerant the inverse solution procedure would be to measurement noise.

It was assumed that *a priori* knowledge would be available that the elastic modulus distributions to be characterized in the examples would be localized (e.g., as could be expected in applications of damage characterization of civil structures [45] or tumor characterization of biological structures [48]). As such, the snapshot response fields used for the Gappy POD procedure were generated using a Gaussian radial basis function (RBF) representation of the elastic modulus (see [14, 1, 13] for other similar works utilizing a RBF representation to define localized elastic modulus variations), as:

$$E(\vec{x}) = E_0 \left[1 + \alpha \cdot exp\left(-\frac{(\vec{x} - \vec{c})^2}{r^2} \right) \right], \tag{4.46}$$

where E_0 is the elastic modulus of the matrix material, α is the relative change in elastic modulus at the inclusion center, $\vec{c}$, is the location of the inclusion center, and r is the breadth of the inclusion. Note, as will be shown in the following example cases, although snapshots were generated based upon single circular inclusion cases (defined by Eqn. (4.46)), the approach presented is capable of being applied to substantially more complicated cases (e.g., multiple inclusions and/or irregularly shaped inclusions).

The finite element method was again used to generate all snapshots for the POD process. In addition, the criteria used to determine the number of modes (m) out of the total number available (n) to use for data reconstruction with Gappy POD was to select the mode with the highest associated eigenvalue (λ in Eqn. 4.35) as well as the minimum number of the remaining modes, such that:

$$\frac{\sum_{j=2}^{m} \lambda^{(j)}}{\sum_{i=2}^{n} \lambda^{(i)}} \times 100\% > 99.9\% \tag{4.47}$$

This criteria was determined to be sufficient to ensure that enough modes were retained from POD for Gappy POD to produce accurate reconstructions, while excluding the modes associated with low eigenvalues that can often cause the matrix $[M]$ in Eqn. (4.42) to be ill-conditioned.

The specific objective function used for the gradient-based optimization procedure to estimate the inverse solutions in both examples was the square of the l_2-error as:

$$f(\vec{p}) = \|\vec{u}(\vec{p}) - \vec{u}^{expn}\|_{l_2}^2 , \tag{4.48}$$

In addition, the same finite element-type parameterization of the unknown elastic modulus distribution was utilized for both the direct inversion and subsequent gradient-based optimization processes (note that all meshes, including both the forward and inverse problems, were verified to be sufficiently refined for accurately analyzing all potential system responses and material property distributions). As noted previously, the interior point optimization method [70] was the specific gradient-based optimization algorithm chosen, with the adjoint method utilized to calculate the necessary gradient at each iteration, to minimize the associated objective function and estimate the solution to the example inverse characterization problems. The scientific analysis software MATLAB [**?**] was used to implement the interior point method, largely with default settings, including calculation of the Hessian with a dense quasi-Newton approximation in which both Newton steps and conjugate gradient steps were both allowed at each iteration. For all cases, the stopping criteria was set to 50 iterations, which was sufficient for convergence.

4.4.1 Example 1: Steady-State Dynamic Test of Hard Matrix with Soft Inclusions

The first example consisted of a simulated 1 $m \times 1$ m aluminum plate. The entire material (matrix and inclusions) was assumed to be known to have a Poisson's ratio of 0.3 and a density of 2700 kg/m^3. The simulated steady-state dynamic test was implemented by applying the harmonic excitation at a frequency of 20 Hz and amplitude of 1 kN/m (factoring out the arbitrary thickness) uniformly to the top surface of the plate. This particular scenario could be relevant to applications in nondestructive evaluation of civil or aerospace structures (e.g., characterizing damage in structural components as could be represented by a reduction in stiffness) from frequency response-based testing.

For the process of generating the snapshots for POD, the elastic modulus of the background material (i.e., matrix material) was assumed to be fixed at 69.0 GPa. Alternatively,

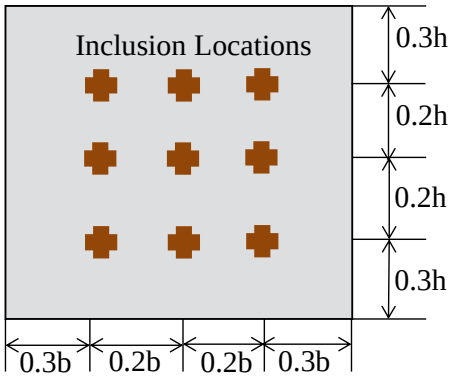

Figure 4.2: Schematic of the nine inclusion centers used separately to generate the snapshots for POD for the numerically simulated examples.

the parameters defining the inclusion based on the RBF description were assumed to be variable. The specific parameter values used to create the snapshots were chosen arbitrarily by uniformly sampling the space of the four variable parameters (the two spatial coordinates, amplitude, and breadth). Three values were chosen for each spatial coordinate of the inclusion center and two values were chosen each for the amplitude and breadth of the inclusion, and one last scenario with no inclusion (i.e., homogeneous matrix material) was added, for a total of 37 parameter combinations used to create snapshots. Fig. 4.2 shows the nine location combinations of the inclusion center used to generate the snapshots. The values of the other two parameters used to create the parameter combinations were chosen based on an expectation of what the lower and upper-end would be for the application, using -0.3 and -0.7 for the amplitude parameter α (i.e., modulus at soft inclusion center of 21 GPa and 48 GPa) and 0.1 m and 0.3 m for the breadth parameter r. To be clear, again note that each of elastic modulus distribution realizations used to create a snapshot contained only one inclusion (other than the homogeneous case, which contained none). 13 out of the 37 total available POD modes were necessary to satisfy the criteria defined in Eqn. 4.47 and were retained for the Gappy POD reconstruction process. Also note that to provide a fair evaluation of the methods presented, none of the modulus distributions considered in the test cases matched the modulus distributions used to generate the snapshots.

4.4.1.1 Case 1 Results: Single Circular Inclusion First, the case of a single circular inclusion within the simulated aluminum plate was examined. A preliminary analysis was done to provide some direct perspective on the capability of the Gappy POD process to estimate the full-field displacement response from the 20 measurement locations provided. Fig. 4.3 shows a representative example of a full-field simulated response including the 1% Gaussian white noise (i.e., the "true response") for a randomly generated single-inclusion elastic modulus distribution in comparison to the full-field displacement estimation from the 20 measurements of this noisy simulated response with the Gappy POD procedure. The relative L_2 and L_∞ errors over the entire domain of this displacement reconstruction in contrast to the true displacement response are 1.8% and 5.0%, respectively. As such, the analysis of the full-field response estimation procedure showed that the Gappy POD approach could reconstruct such a displacement response from partial field measurements with a relatively high level of accuracy.

Next, the complete inverse characterization procedure with Gappy POD response estimation, direct inversion, and gradient-based optimization was examined. Fig. 4.4 shows a representative example of a randomly generated single-inclusion elastic modulus distribution used to simulate experimental measurements (i.e., the "target distribution"), the corresponding elastic modulus distribution estimated by the direct inversion procedure with Gappy POD full-field response estimation (i.e., the initial guess for the gradient based optimization), and the corresponding final elastic modulus distribution estimation from the subsequent gradient-based optimization. In addition, to provide a baseline, Fig. 4.4 also shows results from an attempt to estimate the elastic modulus distribution applying the gradient-based optimization procedure with a homogeneous (i.e., no inclusion) elastic modulus distribution as the initial solution guess (as would be a natural selection without any other information provided), rather than using the results of the direct inversion as the initial guess. It is clear that without the direct inversion-Gappy POD initialization procedure, the gradient-based optimization is entirely ineffectual at providing an accurate estimation of the inverse problem solution, not even qualitatively indicating the presence of an inclusion. Alternatively, the direct inversion with Gappy POD was capable of a significantly more accurate estimation of the elastic modulus distribution, clearly identifying the presence of

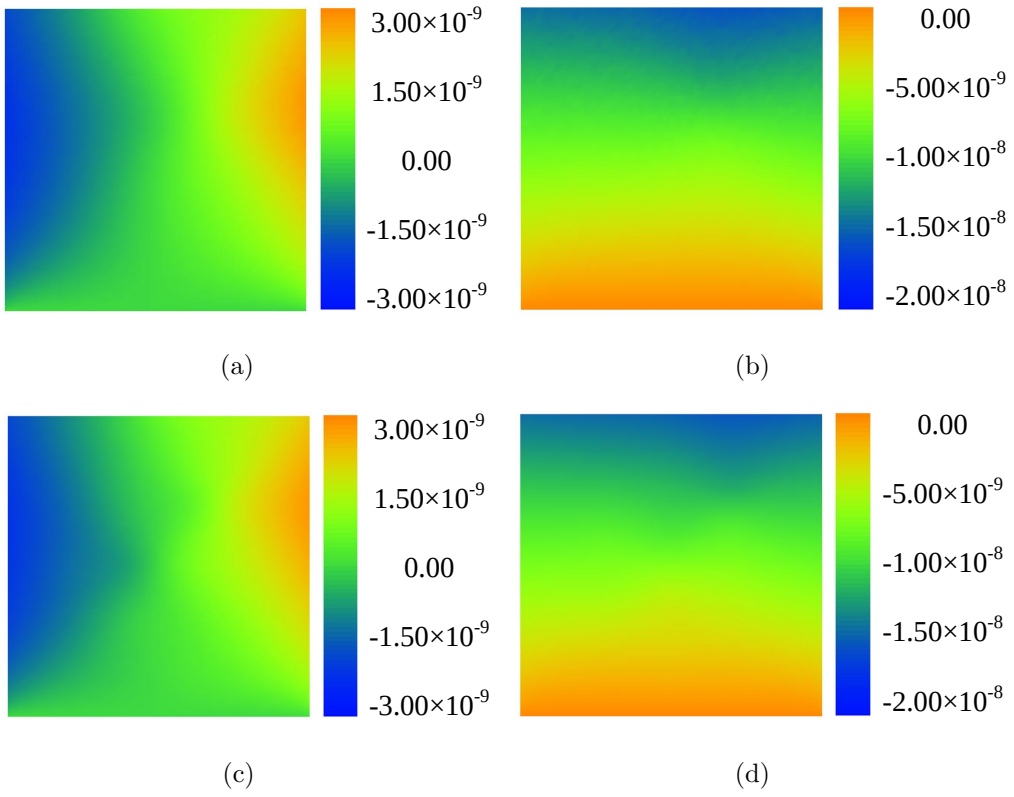

Figure 4.3: Representative single circular inclusion example of the (a) horizontal and (b) vertical components of a simulated experimental displacement field with 1% Gaussian white noise and the (c) horizontal and (d) vertical components of the corresponding reconstructed full-field displacement from Gappy POD with the partial-field measurements for the simulated aluminum plate example (color contours are in units of m).

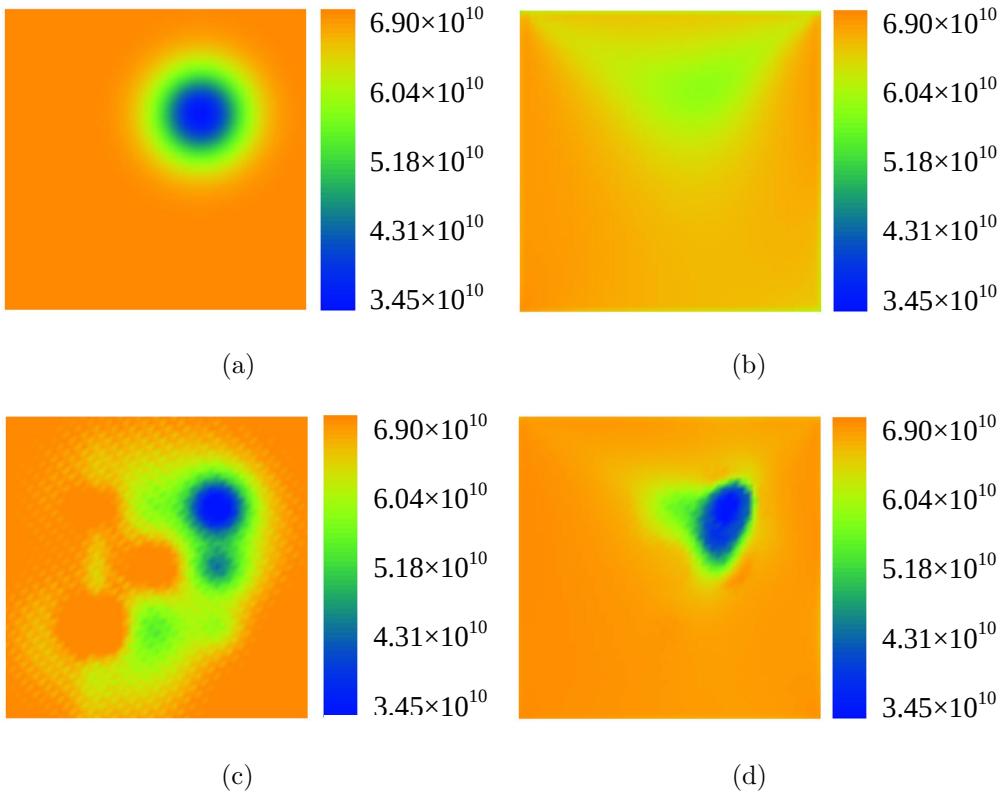

Figure 4.4: Representative single circular inclusion example of (a) the target elastic modulus distribution, (b) the elastic modulus distribution estimated with gradient-based optimization initialized with a homogeneous material distribution, (c) the elastic modulus distribution estimated with the direct inversion approach with Gappy POD full-field displacement reconstruction, and (d) the elastic modulus distribution estimated with gradient-based optimization initialized with the direct inversion solution for the simulated aluminum plate example (color contours in units of Pa).

Table 4.1: The mean and standard deviation of the relative L_2 and L_∞ errors with respect to the elastic modulus distribution estimated with the direct inversion approach and the elastic modulus distribution estimated with the gradient-based optimization approach initialized with the direct inversion result for the five randomly generated trials with a single circular inclusion for the simulated aluminum plate example.

Approach	Relative L_2 Error		Relative L_∞ Error	
	Mean	Std. Dev.	Mean	Std. Dev.
Direct Inversion	5.5%	1.2%	27.0%	7.4%
Gradient Optimization with Direct Inversion	3.7%	1.1%	21.9%	7.2%

an inclusion, but still with an erroneous prediction of dispersed softening throughout the domain. Finally, the application of the gradient-based optimization to the results of the direct inversion was able to significantly "clean up" the approximation, considerably reducing the dispersed softening in the solution estimation. Moreover, for this specific example, the gradient-based optimization was able to improve the relative L_2-error in the elastic modulus estimation by almost a factor of two, from a value of 6.4% after the direct inversion to a final value of 3.6%. The relative L_∞-error was reduced less significantly, going from 23.5% after direct inversion to a final value of 20.9%, but the L_∞-error is a less reliable prediction of the solution quality for localized distributions such as these, since a relatively small shift in the prediction of the inclusion location can result in a disproportionately high L_∞-error.

As a final test for this case, five trials of the inverse characterization procedure, each with a different randomly generated single-inclusion elastic modulus distribution, were performed to examine the consistency of the solution strategy. Table 4.1 shows the mean and standard deviation over the five random trials of the relative L_2 and L_∞ errors corresponding to the elastic modulus distributions estimated with only the direct inversion Gappy POD procedure and with the complete approach including the subsequent gradient-based optimization.

The results from these random trials were highly similar to the results from the representative example shown previously. The inverse procedure was consistently able to accurately predict the elastic modulus distribution over all trials, and the gradient-based step was consistently able to significantly refine the estimation in comparison to the initial guess provided by direct inversion with a relatively small increase in computational expense when using the adjoint method for gradient calculations.

4.4.1.2 Case 2 Results: Two Circular Inclusions The second case considered two circular inclusions within the simulated aluminum plate, and was intended to display the capabilities of the inverse solution procedure for predicting more complicated material property distributions, and particularly distributions that are fundamentally different than those used to simulate the snapshots. Furthermore, this case addresses a common inverse characterization challenge in which the property distribution may be known *priori* to be localized, but the number of localizations (e.g., damage regions) is unknown.

Fig. 4.5 shows a representative example of a randomly generated two-inclusion elastic modulus distribution used to simulate experimental measurements, the corresponding initial elastic modulus distribution estimation from only the direct inversion procedure (with relative L_2 and L_∞ errors of 10.1% and 33.7%), and the corresponding final elastic modulus distribution estimation from the subsequent gradient-based optimization (with relative L_2 and L_∞ errors of 8.8% and 33.6%). Similarly to the previous case, Table 4.2 additionally shows the mean and standard deviation over five randomly generated two-inclusion elastic modulus distribution trials of the relative L_2 and L_∞ errors corresponding to the elastic modulus distributions estimated with only the direct inversion Gappy POD procedure and with the complete approach including the subsequent gradient-based optimization. Although this case represented a considerably more challenging problem than the single-inclusion case, the inverse characterization procedure was still able to accurately estimate the elastic modulus distributions, clearly identifying two inclusion regions in all tests, even though the snapshot set was built only from single-inclusion scenarios. Furthermore, the gradient-based optimization continued to successfully refine the initial approximation provided by direct inversion, substantially reducing the erroneous dispersion seen in the initial estimates of the modulus

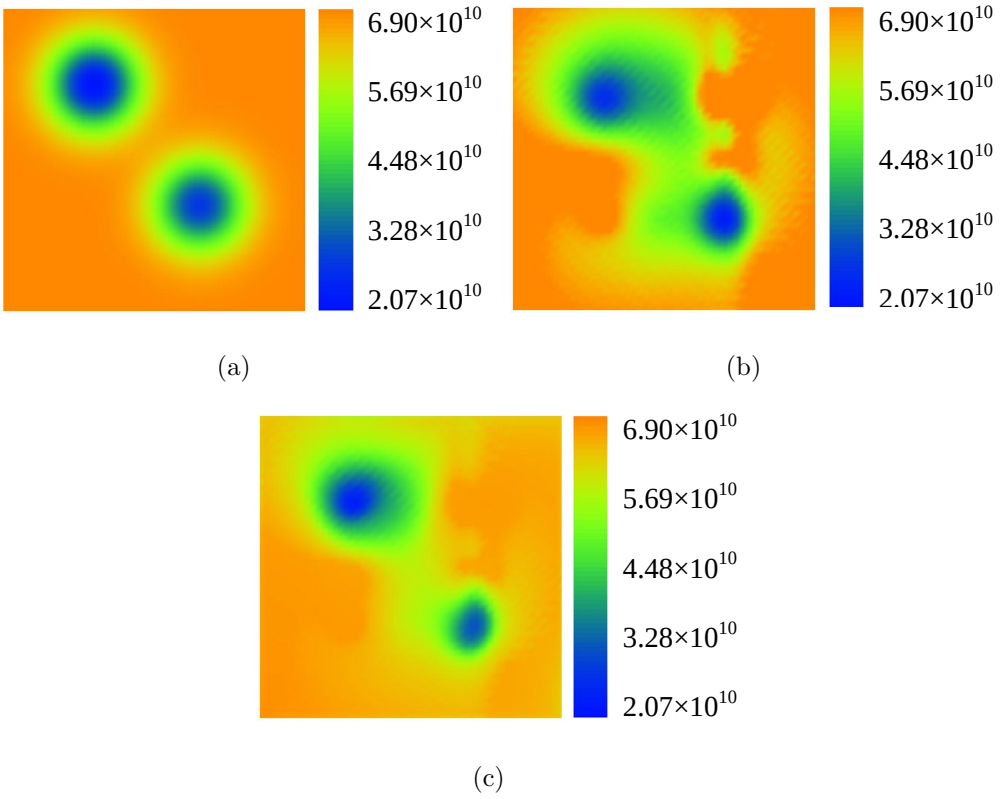

Figure 4.5: Representative two circular inclusion example of (a) the target elastic modulus distribution, (b) the elastic modulus distribution estimated with the direct inversion approach with Gappy POD full-field displacement reconstruction, and (c) the elastic modulus distribution estimated with gradient-based optimization initialized with the direct inversion solution for the simulated aluminum plate example (color contours in units of Pa).

Table 4.2: The mean and standard deviation of the relative L_2 and L_∞ errors with respect to the elastic modulus distribution estimated with the direct inversion approach and the elastic modulus distribution estimated with the gradient-based optimization approach initialized with the direct inversion result for the five randomly generated trials with two circular inclusions for the simulated aluminum plate example.

Approach	Relative L_2 Error		Relative L_∞ Error	
	Mean	Std. Dev.	Mean	Std. Dev.
Direct Inversion	7.6%	1.4%	32.5%	6.7%
Gradient Optimization with Direct Inversion	6.5%	1.4%	28.1%	6.5%

distributions. However, the increase in complexity did lead to a reduction in the level of solution improvement from the gradient-based optimization, which was only able to improve the relative L_2-error of the solution estimation by approximately $10\% - 15\%$ for this case.

4.4.1.3 Case 3 Results: Single Irregular Inclusion The final case for the simulated aluminum plate example explored the potential complexity of the material property distribution further by considering the presence of an irregularly shaped (i.e., non-circular) inclusion within the domain. Again, Fig. 4.6 shows a representative example of an elastic modulus distribution with a randomly selected irregularly shaped inclusion used to simulate experimental measurements, the corresponding initial elastic modulus distribution estimation from only the direct inversion procedure, and the corresponding final elastic modulus distribution estimation from the subsequent gradient-based optimization. Similar to the two inclusion case, the inverse characterization procedure was still able to predict an accurate final estimate to the elastic modulus distribution, even though the full-field response estimation toolset was built only from scenarios with perfectly circular inclusions and the target was irregular. However, in contrast to the two inclusion case, the gradient-based optimization

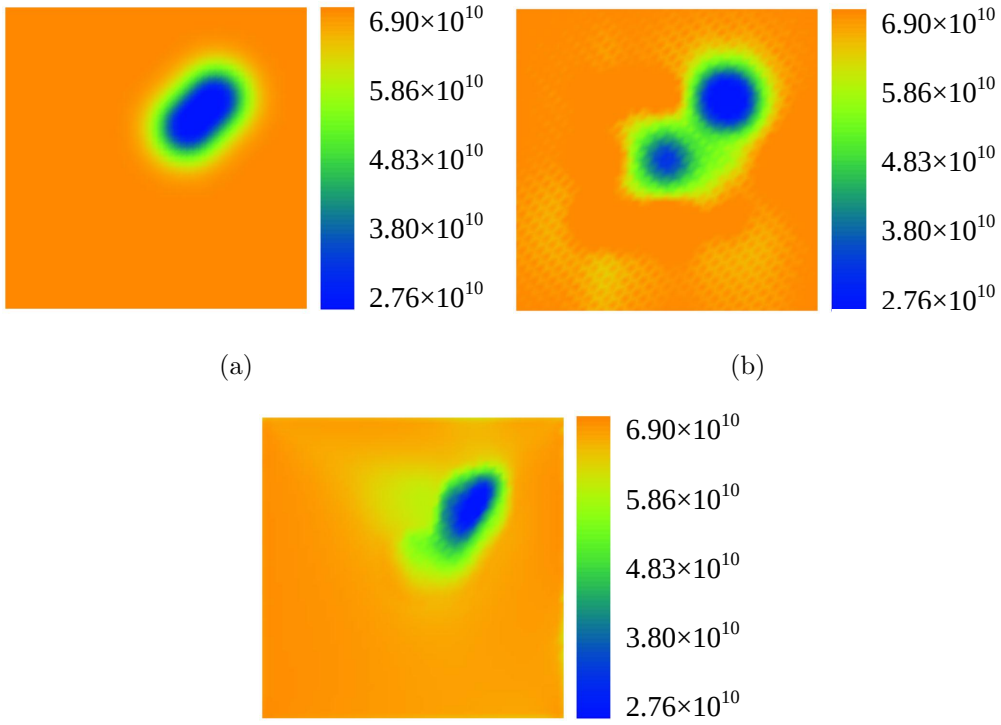

Figure 4.6: Representative irregular inclusion example of (a) the target elastic modulus distribution, (b) the elastic modulus distribution estimated with the direct inversion approach with Gappy POD full-field displacement reconstruction, and (c) the elastic modulus distribution estimated with gradient-based optimization initialized with the direct inversion solution for the simulated aluminum plate example (color contours in units of Pa).

step in the process led to a more substantial improvement in the inverse solution accuracy (closer to that of the single-inclusion case). In qualitative terms, the direct inversion solution appears to indicate the presence of two relatively circular inclusions in the modulus distribution, while the gradient-based refinement correctly resolves only one irregularly shaped inclusion. Moreover, the relative L_2 and L_∞ errors over the domain for the elastic modulus estimation respectively improved from 8.2% and 47.1% for the initial direct inversion estimation to 5.8% and 36.3% following gradient based optimization (i.e., an improvement in the relative L_2-error of approximately 30% and an improvement in the relative L_∞-error of approximately 23%).

4.4.2 Example 2: Static Test of Soft Matrix with a Hard Inclusion

To explore a different physical system and potential application, the final example consisted of a simulated 50 $mm \times 50$ mm tissue block. The entire material (matrix and inclusion) was assumed to be known to be nearly incompressible with a Poisson's ratio of 0.49999. For this example the simulated test was assumed to be static, with a 0.2 N/mm (factoring out the arbitrary thickness) excitation applied uniformly to the top surface of the tissue block. Note that the only difference in the formulation presented herein to convert to static rather than steady-state dynamic is that the momentum terms are set to zero. This second example scenario was intended to relate to potential applications of tissue characterization (e.g., tumor characterization) from (quasi-) static mechanical testing [22, 48].

Overall, the POD snapshot generation process was almost identical to the previous simulated aluminum plate example. Again, 37 parameter combinations were used to create the snapshots, and the same nine location combinations of a single circular RBF inclusion center were used as the first example (Fig. 4.2). Alternatively, the elastic modulus of the matrix (i.e., healthy) material was assumed to be fixed at 15 kPa, which was based on normal glandular breast tissue [81, 51]. The two values of the amplitude parameter used were 1 and 3 (i.e., modulus at the hard inclusion center of approximately 30 kPa and 60 kPa), and the two values of the breadth parameter used were 5 mm and 15 mm. Note that, as before, each snapshot material property distribution other than the homogeneous case contained

only one inclusion. 15 out of the 37 total available POD modes were necessary to satisfy the criteria defined in Eqn. 4.47 and were retained for the Gappy POD reconstruction process.

4.4.2.1 Results: Single Irregular Inclusion One case involving a single irregularly shaped inclusion was considered for the final simulated experiment with the statically tested tissue block. Fig. 4.7 shows a representative example of an elastic modulus distribution with a randomly selected irregularly shaped inclusion used to simulate experimental measurements, the corresponding initial elastic modulus distribution estimation from only the direct inversion procedure (with relative L_2 and L_∞ errors of 21.8% and 53.5%), and the corresponding final elastic modulus distribution estimation from the subsequent gradient-based optimization(with relative L_2 and L_∞ errors of 17.8% and 38.6%). Although a different mechanical testing method was considered and the properties of the system examined were substantially different, the inverse characterization results for this tissue block example were consistent with those shown for the aluminum plate example. The initial direct inversion estimation approximated the location of the inclusion relatively well, but the distribution and magnitude had significant error. Moreover, similarly to the prior test case with an irregular inclusion, although less dramatic, the initial direct inversion results appear to estimate two inclusions. The gradient-based optimization was then able to substantially improve the estimation of the elastic modulus distribution, and indicating a single irregularly shaped inclusion. One possible explanation for the slight increase in the overall solution error for this case compared to the prior test case could be the increase in the range of the elastic modulus magnitude for this tissue example. Yet, the final estimate of the elastic modulus distribution is still clearly a qualitatively accurate estimate of the location, size, and shape of the hard inclusion, which was produced at the relatively small computational cost of no more than approximately 100 finite element analyses (neglecting the one-time cost of creating the POD modes) without the need to provide a specific initial guess for the inverse solution or complicated regularization in the optimization procedure.

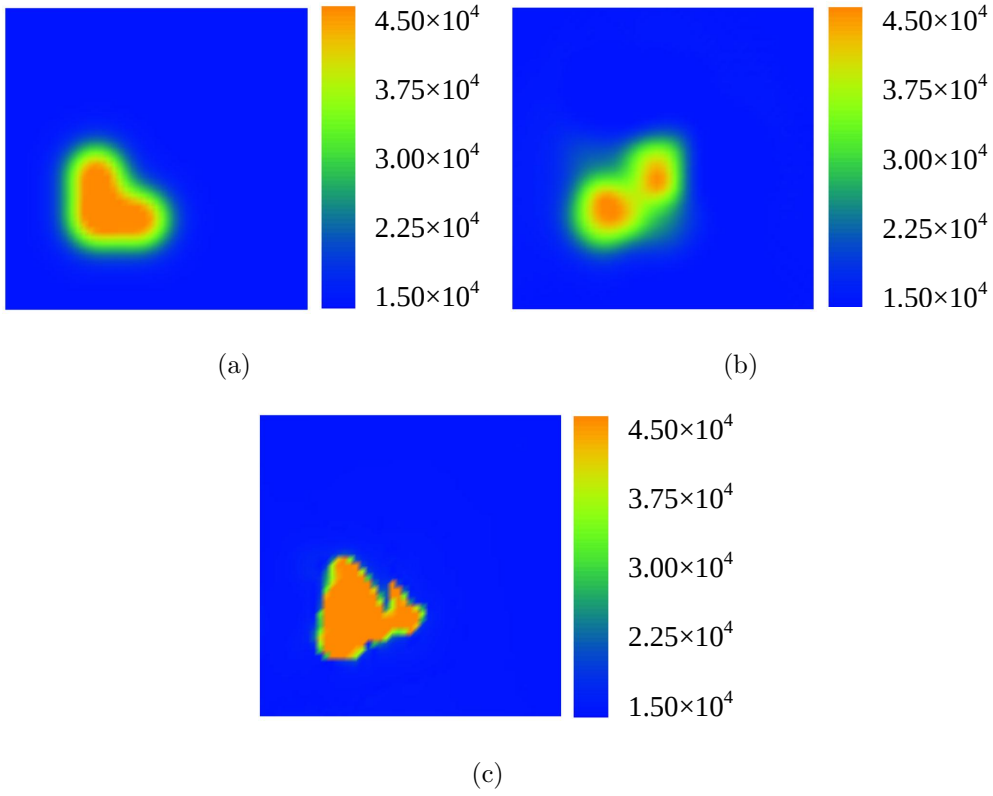

Figure 4.7: Representative irregular inclusion example of (a) the target elastic modulus distribution, (b) the elastic modulus distribution estimated with the direct inversion approach with Gappy POD full-field displacement reconstruction, and (c) the elastic modulus distribution estimated with gradient-based optimization initialized with the direct inversion solution for the simulated tissue block example (color contours in units of Pa).

4.5 CONCLUSIONS

A gradient-based optimization approach for computationally efficient inverse material characterization from partial-field system response measurements capable of using a generally applicable parameterization (e.g., finite element-type parameterization) was presented and analyzed. The approach first builds a Gappy POD machine learning tool for full-field response estimation from the partial-field measurements using available *a priori* information regarding the potential unknown material property distribution. Then, a physics-based direct inversion approach with a finite element-type parameterization uses the Gappy POD estimated full-field response to produce a first estimate of the spatial distribution of the unknown material property. Lastly, the direct inversion results of the material property distribution are further refined with a gradient-based optimization strategy, which uses the adjoint method to calculate the gradients efficiently, to produce the final estimate of the material property distribution. Through numerically simulated example inverse problems based on the characterization of elastic modulus distributions with localized variations in simple structures, the inverse characterization approach was shown to efficiently estimate spatial distributions of the elastic modulus with relatively high solution accuracy from limited partial-field displacement response measurements. Furthermore, the final gradient-based optimization component was shown to be a necessary step in the characterization procedure to provide substantial and physically significant improvement in the inverse solution estimation in comparison to the direct inversion estimate alone. In addition, the complete inverse characterization approach was shown to have the capability to accurately predict material property distributions that are significantly more complicated, and particularly those that are potentially fundamentally different than the assumed material property distributions used to create the Gappy POD component. For instance, the examples presented generated the Gappy POD response estimation tool assuming elastic modulus distributions with a single perfectly circular inclusion. Yet, the inverse characterization approach was then capable of estimating elastic modulus fields with multiple inclusions and inclusions that were irregularly shaped.

5.0 CURRENT CAPABILITIES AND FUTURE DIRECTIONS

Computational inverse solution strategies consisting of compact parameterization approaches and hybrid compact-generalized (i.e., mesh-based) parameterization approaches have been developed and validated for the characterization of localized variations of material properties in solids and structures. The proposed solution strategies are proven to be efficient and accurate to characterize the localized variations of material properties through various numerical and experimental examples according to different applications, such as crack identification and elasticity imaging. For the compact parameterization approaches, a strategy using multi-objective optimization for inverse characterization of material loss (i.e., cracks or erosion) in structural components was presented first. For this first component, the assumption is made that sufficient a *priori* information is available to restrict the parameterization of the unknown field to a known number and shape of material loss regions (i.e., the inverse problem is only required to identify size and location of these regions). Through simulated test problems of damage characterization, the multi-objective optimization approach was shown to provide increased solution estimate diversity during the search process, which results in a substantial improvement in the capabilities to traverse the optimization search space to minimize the measurement error and produce accurate damage size and location estimates in comparison with analogous single objective optimization approaches. An extension of this multi-objective approach was then presented that addresses problems for which the quantity of localized changes in properties is unknown. Thus, a self-evolving parameterization algorithm was presented that utilizes the substantial diversity in the Pareto front of potential solutions provided by the multi-objective optimization approach to build up the parameterization iteratively with an *ad hoc* clustering algorithm, and thereby determine the quantity, size, and location of localized changes in properties with minimal computational

expense. Similarly as before, through simulated test problems based on characterization of damage within plates, the solution strategy with self-evolving parameterization was shown to provide an accurate and efficient process for the solution of inverse characterization of localized property changes.

For hybrid compact-generalized parameterization approaches, the nature (i.e., shape) of the property variation is no longer assumed to be known as precisely a *priori*, while still some amount of the knowledge that the solution is localized in nature is used to balance computational cost induced by the the generalized (mesh-based) parameterization. The initial approach established combines a machine learning data reconstruction strategy known as Gappy proper orthogonal decomposition (POD) with a least-squares direct inversion approach to estimate material stiffness distributions in solids (i.e., to solve elastography problems). The direct inversion approach uses a generalized mesh-based parameterization of the unknown field, but full-field response measurements (i.e., measurements everywhere in the solid) are required, which are not available for most practical inverse characterization problems. Therefore, the gappy POD technique first identifies the pattern of potential response fields of the solid through a collection of a *priori* forward numerical analyses of the solid response with a specified compact parameterization and a corresponding collection of arbitrarily generated parameter sets. Once the pattern is identified, the gappy POD technique is able to use the available partial-field measurement data to estimate the full-field response of the solid to be used by the direct inversion. Through simulated test problems relating to characterization of inclusions in solids, the direct inversion approach with gappy POD was shown to provide highly efficient and relatively accurate inverse characterization results for the prediction of Young's modulus distributions from partial-field measurement data. This direct inversion approach was further validated through an example problem regarding characterization of the layered stiffness properties of an engineered vessel from ultrasound measurements. Lastly, an extension of this hybrid approach was presented that uses the characterization results provided by the previous direct inversion approach as the initial estimate for a gradient-based optimization process to further refine/improve the inverse solution estimate. In addition, the adjoint method is used to calculate the gradient for the optimization process with minimal computational expense to maintain the overall com-

putational efficiency of the inverse solution process. Again, through simulated test problems based on the characterization of localized, but arbitrarily shaped, inclusions within solids, the three-step (gappy POD - direct inversion - gradient-based optimization) inverse characterization approach was shown to efficiently provide accurate and relatively unique inverse characterization estimates for various types of inclusions regardless of inclusion geometry and quantity.

For future directions of inverse characterization of material properties variation, two important issues are necessary to be considered further. First, more accurate numerical modeling should be established considering different physical problems. For instance, the extended finite element method is well suited for modeling crack problems; for tissue characterization, viscoelastic constitutive models should be considered for higher fidelity modeling. In addition, the uncertainty of boundary conditions is usually necessary to be considered, especially for biological tissue modeling *in vivo*. Secondly, inclusions with more complex geometry or distributions should be considered and quantified. Parameterization with the assistance of cubic splines has been shown to be capable of identifying arbitrarily shaped inclusion, although a *priori* information of inclusion quantity is still assumed. Mesh-based parameterization also has shown great potential and capability to characterize any type of material property variation, however the optimization algorithm is a great challenge due to the large dimensionality of parameterization. Thus, it is important to optimize the sensor placement to obtain more sensitive measurement information towards better inverse solutions. Moreover, adaptive parameterization refinement can be used to evolve the accuracy of the inverse solutions for characterization from coarse to fine. In addition, mesh-based parameterization can also be developed as an efficient and useful technique for fast inclusion localization and identification, which has the similar benefit as the topological derivative or source sensitive approaches. After the inclusion is localized, compact paramterization with small dimensionality can be employed to obtain more accurate characterization solutions.

BIBLIOGRAPHY

[1] M.A. Aguilo, W. Aquino, J.C. Brigham, and M. Fatemi. An inverse problem approach for elasticity imaging through vibroacoustics. *Medical Imaging, IEEE Transactions on*, 29(4):1012–1021, 2010.

[2] W Aquino, JC Brigham, CJ Earls, and N Sukumar. Generalized finite element method using proper orthogonal decomposition. *International Journal for Numerical Methods in Engineering*, 79(7):887–906, 2009.

[3] JV Araujo dos Santos, Mota Soares, CA Mota Soares, and NMM Maia. Structural damage identification in laminated structures using frf data. *Composite Structures*, 67(2):239–249, 2005.

[4] Biswanath Banerjee, Timothy F Walsh, Wilkins Aquino, and Marc Bonnet. Large scale parameter estimation problems in frequency-domain elastodynamics using an error in constitutive equation functional. *Computer methods in applied mechanics and engineering*, 253:60–72, 2013.

[5] Paul E Barbone and Jeffrey C Bamber. Quantitative elasticity imaging: what can and cannot be inferred from strain images. *Physics in Medicine and Biology*, 47(12):2147, 2002.

[6] A. Benhamena, L. Aminallah, B. Bachir Bouiadjra, M. Benguediab, A. Amrouche, and N. Benseddiq. J integral solution for semi-elliptical surface crack in high density polyethylene pipe under bending. *Materials and Design*, 32(5):2561 – 2569, 2011.

[7] Marc Bonnet and Bojan B. Guzina. Sounding of finite solid bodies by way of topological derivative. *International Journal for Numerical Methods in Engineering*, 61(13):2344–2373, 2004.

[8] J. C. Brigham, W. Aquino, F. G. Mitri, J. F. Greenleaf, and M. Fatemi. Inverse estimation of viscoelastic material properties for solids immersed in fluids using vibroacoustic techniques. *Journal of Applied Physics*, 101(2):023509 –023509–14, jan 2007.

[9] John C. Brigham and Wilkins Aquino. Surrogate-model accelerated random search algorithm for global optimization with applications to inverse material identification.

Computer Methods in Applied Mechanics and Engineering, 196(45C48):4561 – 4576, 2007.

[10] John C. Brigham and Wilkins Aquino. Inverse viscoelastic material characterization using pod reduced-order modeling in acousticcstructure interaction. *Computer Methods in Applied Mechanics and Engineering*, 198(9C12):893 – 903, 2009.

[11] E. Peter Carden and Paul Fanning. Vibration based condition monitoring: A review. *Structural Health Monitoring*, 3(4):355–377, 2004.

[12] Konstantinos Christodoulou, Evaggelos Ntotsios, Costas Papadimitriou, and Panagiotis Panetsos. Structural model updating and prediction variability using pareto optimal models. *Computer Methods in Applied Mechanics and Engineering*, 198(1):138 – 149, 2008.

[13] C Compas, E Wong, Xiaojie Huang, Smita Sampath, B Lin, X Papademetris, D Dione, A Sinusas, M O'Donnell, and J Duncan. Radial basis functions for combining shape and speckle tracking in 4d echocardiography. 2014.

[14] M Contreras, S Nagarajaiah, and S Narasimhan. Real time detection of stiffness change using a radial basis function augmented observer formulation. *Smart Materials and Structures*, 20(3):035013, 2011.

[15] K. Deb, A. Pratap, S. Agarwal, and T. Meyarivan. A fast and elitist multiobjective genetic algorithm: Nsga-ii. *Evolutionary Computation, IEEE Transactions on*, 6(2):182 –197, apr 2002.

[16] Kalyanmoy Deb. Multi-objective optimization. *Multi-objective optimization using evolutionary algorithms*, pages 13–46, 2001.

[17] Kalyanmoy Deb, Amrit Pratap, Sameer Agarwal, and TAMT Meyarivan. A fast and elitist multiobjective genetic algorithm: Nsga-ii. *Evolutionary Computation, IEEE Transactions on*, 6(2):182–197, 2002.

[18] Debaditya Dutta, Kee-Won Lee, Robert A Allen, Yadong Wang, John C Brigham, and Kang Kim. Non-invasive assessment of elastic modulus of arterial constructs during cell culture using ultrasound elasticity imaging. *Ultrasound in medicine & biology*, 39(11):2103–2115, 2013.

[19] R. Everson and L. Sirovich. Karhuencloeve procedure for gappy data. *J. Opt. Soc. Am. A*, 12(8):1657–1664, Aug 1995.

[20] Gonzalo R Feijoo. A new method in inverse scattering based on the topological derivative. *Inverse Problems*, 20(6), 2004.

[21] Victor Giurgiutiu, Andrei Zagrai, and Jingjing Bao. Damage Identification in Aging Aircraft Structures with Piezoelectric Wafer Active Sensors. *Journal of intelligent Material Systems and Structures*, 15:673–687, 2004.

[22] Sevan Goenezen, Paul Barbone, and Assad A. Oberai. Solution of the nonlinear elasticity imaging inverse problem: The incompressible case. *Computer Methods in Applied Mechanics and Engineering*, 200(13C16):1406 – 1420, 2011.

[23] Nachiket H Gokhale, Paul E Barbone, and Assad A Oberai. Solution of the nonlinear elasticity imaging inverse problem: the compressible case. *Inverse Problems*, 24(4):045010, 2008.

[24] H.Y. Guo and Z.L. Li. A two-stage method to identify structural damage sites and extents by using evidence theory and micro-search genetic algorithm. *Mechanical Systems and Signal Processing*, 23(3):769 – 782, 2009.

[25] B. B. Guzina and M. Bonnet. Topological derivative for the inverse scattering of elastic waves. *The Quarterly Journal of Mechanics and Applied Mathematics*, 57(2):161–179, 2004.

[26] Bojan B Guzina and Marc Bonnet. Topological derivative for the inverse scattering of elastic waves. *The Quarterly Journal of Mechanics and Applied Mathematics*, 57(2):161–179, 2004.

[27] Yiannis Haralampidis, Costas Papadimitriou, and Maria Pavlidou. Multi-objective framework for structural model identification. *Earthquake Engineering and Structural Dynamics*, 34(6):665–685, 2005.

[28] K. C. Hari, M. Nabi, and S. V. Kulkarni. Improved fem model for defect-shape construction from mfl signal by using genetic algorithm. *IET Science, Measurement and Technology*, 1(4):196 – 200, 2007.

[29] Bijaya Jaishi and Wei-Xin Ren. Finite element model updating based on eigenvalue and strain energy residuals using multiobjective optimisation technique. *Mechanical Systems and Signal Processing*, 21(5):2295 – 2317, 2007.

[30] W.Y. Jeong, C.J. Earls, W.D. Philpot, and A.T. Zehnder. Inverse thermographic characterization of optically unresolvable through cracks in thin metal plates. *Mechanical Systems and Signal Processing*, 27(0):634 – 650, 2012.

[31] Tracy S. Gendron John P. Slade. Flow accelerated corrosion and cracking of carbon steel piping in primary water - operating experience at the point lepreau generating station. 2005.

[32] Sungmoon Jung, Seung-Yong Ok, and Junho Song. Robust structural damage identification based on multi-objective optimization. *International Journal for Numerical Methods in Engineering*, 81(6):786–804, 2010.

[33] J.M. Ko, Z.G. Sun, and Y.Q. Ni. Multi-stage identification scheme for detecting damage in cable-stayed kap shui mun bridge. *Engineering Structures*, 24(7):857 – 868, 2002.

[34] B. Kouchmeshky, W. Aquino, and Adam E. Billek. Structural damage identification using co-evolution and frequency response functions. *Structural Control and Health Monitoring*, 15(2):162–182, 2008.

[35] B. Kouchmeshky, W. Aquino, J. C. Bongard, and H. Lipson. Co-evolutionary algorithm for structural damage identification using minimal physical testing. *International Journal for Numerical Methods in Engineering*, 69(5):1085–1107, 2007.

[36] Yue Li, L. Udpa, and S.S. Udpa. Three-dimensional defect reconstruction from eddy-current nde signals using a genetic local search algorithm. *Magnetics, IEEE Transactions on*, 40(2):410 – 417, march 2004.

[37] Yue Li, L. Udpa, and S.S. Udpa. Three-dimensional defect reconstruction from eddy-current nde signals using a genetic local search algorithm. *Magnetics, IEEE Transactions on*, 40(2):410 – 417, march 2004.

[38] Shaw-Wen Liu, Jin H Huang, Jen-Chun Sung, and CC Lee. Detection of cracks using neural networks and computational mechanics. *Computer Methods in Applied Mechanics and Engineering*, 191(25):2831–2845, 2002.

[39] N.M.M. Maia, J.M.M. Silva, E.A.M. Almas, and R.P.C. Sampaio. Damage detection in structures: From mode shape to frequency response function methods. *Mechanical Systems and Signal Processing*, 17(3):489 – 498, 2003.

[40] G. Manson, K. Worden, and D. Allman. Experimental validation of a structural health monitoring methodology: Part iii. damage location on an aircraft wing. *Journal of Sound and Vibration*, 259(2):365 – 385, 2003.

[41] MathWorks. Matlab r2011b documentation. *MATLAB R2011b Documentation*, 2011.

[42] B. Mechab, B. Serier, B. Bachir Bouiadjra, K. Kaddouri, and X. Feaugas. Linear and non-linear analyses for semi-elliptical surface cracks in pipes under bending. *International Journal of Pressure Vessels and Piping*, 88(1):57 – 63, 2011.

[43] Jennifer E Michaels. Detection, localization and characterization of damage in plates with an in situ array of spatially distributed ultrasonic sensors. *Smart Materials and Structures*, 17(3):035035, 2008.

[44] P Moreno-García, JV Araújo dos Santos, and H Lopes. A new technique to optimize the use of mode shape derivatives to localize damage in laminated composite plates. *Composite Structures*, 108:548–554, 2014.

[45] Bahram Notghi and John C Brigham. Optimal nondestructive test design for maximum sensitivity and minimal redundancy for applications in material characterization. *Smart Materials and Structures*, 22(12):125036, 2013.

[46] Assad A Oberai, Nachiket H Gokhale, Marvin M Doyley, and Jeffrey C Bamber. Evaluation of the adjoint equation based algorithm for elasticity imaging. *Physics in Medicine and Biology*, 49(13):2955, 2004.

[47] Assad A Oberai, Nachiket H Gokhale, and Gonzalo R Feijóo. Solution of inverse problems in elasticity imaging using the adjoint method. *Inverse Problems*, 19(2):297, 2003.

[48] Assad A Oberai, Nachiket H Gokhale, Sevan Goenezen, Paul E Barbone, Timothy J Hall, Amy M Sommer, and Jingfeng Jiang. Linear and nonlinear elasticity imaging of soft tissue in vivo: demonstration of feasibility. *Physics in medicine and biology*, 54(5):1191, 2009.

[49] Travis E Oliphant, Jennifer L Mahowald, Richard L Ehman, and James F Greenleaf. Complex-valued quantitative stiffness estimation using dynamic displacement measurements and local inversion of conservation of momentum. In *Ultrasonics Symposium, 1999. Proceedings. 1999 IEEE*, volume 2, pages 1641–1644. IEEE, 1999.

[50] Travis E Oliphant, Armando Manduca, Richard L Ehman, and James F Greenleaf. Complex-valued stiffness reconstruction for magnetic resonance elastography by algebraic inversion of the differential equation. *Magnetic resonance in Medicine*, 45(2):299–310, 2001.

[51] Eunyoung Park and Antoinette M Maniatty. Shear modulus reconstruction in dynamic elastography: time harmonic case. *Physics in medicine and biology*, 51(15):3697, 2006.

[52] Ricardo Perera, Sheng-En Fang, and C. Huerta. Structural crack detection without updated baseline model by single and multiobjective optimization. *Mechanical Systems and Signal Processing*, 23(3):752 – 768, 2009.

[53] Ricardo Perera, Sheng-En Fang, and Antonio Ruiz. Application of particle swarm optimization and genetic algorithms to multiobjective damage identification inverse problems with modelling errors. *Meccanica*, 45:723–734, 2010. 10.1007/s11012-009-9264-5.

[54] Ricardo Perera and Antonio Ruiz. A multistage fe updating procedure for damage identification in large-scale structures based on multiobjective evolutionary optimization. *Mechanical Systems and Signal Processing*, 22(4):970 – 991, 2008.

[55] Ricardo Perera, Antonio Ruiz, and Carlos Manzano. An evolutionary multiobjective framework for structural damage localization and quantification. *Engineering Structures*, 29(10):2540 – 2550, 2007.

[56] Ricardo Perera, Antonio Ruiz, and Carlos Manzano. Performance assessment of multicriteria damage identification genetic algorithms. *Computers and Structures*, 87(1-2):120 – 127, 2009.

[57] KR Raghavan and Andrew E Yagle. Forward and inverse problems in elasticity imaging of soft tissues. *Nuclear Science, IEEE Transactions on*, 41(4):1639–1648, 1994.

[58] Anne M. Raich and Tamas R. Liszkai. Multi-objective optimization of sensor and excitation layouts for frequency response function-based structural damage identification. *Computer-Aided Civil and Infrastructure Engineering*, pages no–no, 2011.

[59] Junuthula Narasimha Reddy. *An introduction to the finite element method*, volume 2. McGraw-Hill New York, 1993.

[60] Anthony J Romano, Joseph A Bucaro, RL Ehnan, and Joseph J Shirron. Evaluation of a material parameter extraction algorithm using mri-based displacement measurements. *Ultrasonics, Ferroelectrics and Frequency Control, IEEE Transactions on*, 47(6):1575–1581, 2000.

[61] Anthony J Romano, Joseph J Shirron, and Joseph A Bucaro. On the noninvasive determination of material parameters from a knowledge of elastic displacements theory and numerical simulation. *Ultrasonics, Ferroelectrics and Frequency Control, IEEE Transactions on*, 45(3):751–759, 1998.

[62] Daniel E. Rosario, John C. Brigham, and Wilkins Aquino. Identification of material properties of orthotropic elastic cylinders immersed in fluid using vibroacoustic techniques. *Ultrasonics*, 48(6C7):547 – 552, 2008. Selected Papers from ICU 2007.

[63] Anthony Sabelli and Wilkins Aquino. A source sensitivity approach for source localization in steady-state linear systems. *Inverse Problems*, 29(9):095005, 2013.

[64] John J Charonko Samuel G Raben and Pavlos P Vlachos. Adaptive gappy proper orthogonal decomposition for particle image velocimetry data reconstruction. *Measurement Science and Technology*, 23(2), 2012.

[65] AR Skovoroda, SY Emelianov, and M O'Donnell. Tissue elasticity reconstruction based on ultrasonic displacement and strain images. *Ultrasonics, Ferroelectrics and Frequency Control, IEEE Transactions on*, 42(4):747–765, 1995.

[66] Chikayoshi Sumi and Kiyoshi Nakayama. A robust numerical solution to reconstruct a globally relative shear modulus distribution from strain measurements. *Medical Imaging, IEEE Transactions on*, 17(3):419–428, 1998.

[67] Murali Damodaran Tan Bui-Thanh and Karen E. Willcox. Aerodynamic Data Reconstruction and Inverse Design Using Proper Orthogonal Decomposition. *AIAA Journal*, 42:1505–1516, 2004.

[68] Anne Teughels, Johan Maeck, and Guido De Roeck. Damage assessment by fe model updating using damage functions. *Computers and Structures*, 80(25):1869 – 1879, 2002.

[69] Daniele Venturi and George Em Karniadakis. Gappy data and reconstruction procedures for flow past a cylinder. *Journal of Fluid Mechanics*, 519:315–336, 2004.

[70] Andreas Wächter and Lorenz T Biegler. On the implementation of an interior-point filter line-search algorithm for large-scale nonlinear programming. *Mathematical programming*, 106(1):25–57, 2006.

[71] Mengyu Wang and John C Brigham. Assessment of multi-objective optimization for nondestructive evaluation of damage in structural components. *Journal of Intelligent Material Systems and Structures*, page 1045389X13494933, 2013.

[72] Mengyu Wang and John C Brigham. A computational nondestructive evaluation algorithm combining self-evolving parameterization and multi-objective optimization for quantitative damage characterization. *Journal of Nondestructive Evaluation*, pages 1–15, 2014.

[73] Shuang Wang and John C Brigham. A computational framework for the optimal design of morphing processes in locally activated smart material structures. *Smart Materials and Structures*, 21(10):105016, 2012.

[74] K. Willcox. Unsteady flow sensing and estimation via the gappy proper orthogonal decomposition. *Computers and Fluids*, 35(2):208 – 226, 2006.

[75] SJ Wright and J Nocedal. *Numerical optimization*, volume 2. Springer New York, 1999.

[76] Jia Wu, Yingqian Wang, Marc A Simon, Michael S Sacks, and John C Brigham. A new computational framework for anatomically consistent 3d statistical shape analysis with clinical imaging applications. *Computer Methods in Biomechanics and Biomedical Engineering: Imaging & Visualization*, 1(1):13–27, 2013.

[77] Hongpo Xu and JagMohan Humar. Damage detection in a girder bridge by artificial neural network technique. *Computer-Aided Civil and Infrastructure Engineering*, 21(6):450–464, 2006.

[78] A. Yakhot, T. Anor, and G.E. Karniadakis. A reconstruction method for gappy and noisy arterial flow data. *Medical Imaging, IEEE Transactions on*, 26(12):1681–1697, 2007.

[79] Kinzo Kishida Yoshiaki Yamauchi, Artur Guzik and Che-Hsien Li. A study of the stability, reliability, and accuracy of neubrescope-based pipe thinning detection system. 2007.

[80] Gun Jin Yun, Kenneth A. Ogorzalek, Shirley J. Dyke, and Wei Song. A two-stage damage detection approach based on subset selection and genetic algorithms. 2009.

[81] Y. Zhu, T.J. Hall, and Jingfeng Jiang. A finite-element approach for young's modulus reconstruction. *Medical Imaging, IEEE Transactions on*, 22(7):890–901, 2003.